Spin Measurements of Accreting Black Holes: A Foundation for X-Ray Continuum Fitting

Spin Measurements of Accreting Black Holes: A Foundation for X-ray Continuum Fitting

A dissertation presented

by

James Francis Steiner

to

The Department of Astronomy

in partial fulfillment of the requirements

for the degree of

Doctor of Philosophy

in the subject of

Astronomy

Harvard University

Cambridge, Massachusetts

March 2012

Thesis Advisor: Doctor Jeffrey E. McClintock James Francis Steiner

Spin Measurements of Accreting Black Holes: A Foundation for X-ray Continuum Fitting

Abstract

Remarkably, an astrophysical black hole has only two attributes: its mass and its spin angular momentum. Spin is often associated with the exotic behavior that black holes manifest such as the production of relativistic and energetic jets. In this thesis, we advance one of the two primary methods of measuring black hole spin, namely, the continuum-fitting method by (1) improving the methodology; (2) testing two foundational assumptions; and (3) measuring the spins of two stellar-mass black holes in X-ray binary systems. *Methodology:* We present an empirical model of Comptonization that self-consistently generates a hard power-law component by upscattering thermal accretion disk photons as they traverse a hot corona. We show that this model enables reliable measurements of spin for far more X-ray spectral data and for more sources than previously thought possible. *Testing the foundations:* First, by an exhaustive study of the X-ray spectra of LMC X–3, we show that the inner radius of its accretion disk is constant over decades and unaffected by source variability. Identifying this fixed inner radius with the radius of the innermost stable circular orbit in general relativity, our findings establish a firm foundation for the measurement of black hole spin. Secondly, we test the customary assumption that the inclination angles of the black-hole's spin axis and the binary's orbital axis are the same; for XTE J1550–564 we show that they are aligned to within 12° by modeling the kinematics of the large-scale jets of this microquasar. *Measuring spins:* We have made the first accurate continuum-fitting spin measurements of the black hole primaries in H1743–322 and XTE J1550–564. For this latter black hole, we have also measured its spin using the other leading method, namely, modeling the broad red wing of the Fe $K\alpha$ line. As we show, these two independent measurements of spin are in agreement.

Contents

Acknowledgments

What a remarkable feeling, to have a completed dissertation behind me (presumably in front of you). While the feeling is so very sweet, it is sad to be at a fork in the road which will lead me away from what has been a wonderful chapter in my life, and away from many friends and colleagues.

Before we go diving into the world of black holes, the fortunate but impossible task of thanking the many people who helped me to obtain this PhD is at hand. There are a great many friends, teachers, and mentors who have been integral in this. While this in no way adequately matches the depth or reach of my thanks, I hope to at least pay tribute to some of the major culprits here.

First and foremost, I must thank my wonderful wife Christina. She is more wonderful than laughter. Christina, I can't imagine any of this without you. Thank you to all of my family. Mom, Dad, Katherine, Adam, Mike, Grandma and Grandpa, Stan, Deb, Vanessa, Elizabeth, and Uncle Jim, I love you all. You inspire the best in me.

The best part of grad school for me has been the wonderful set of friendships I have formed. Jeff, you're a major part of this too, but I'll come back to you later. Thank you Gurtina Besla, Sarah Ballard, Robert Marcus and Robert Harris, Sasha Tchekhovskoy, Dave Musicant, Manasvita Joshi and Karthikeyan Karunanidhi, Kelly and Dustin Sorel, Laura Blecha, Ryan Hickox, Wen-fai Fong, Lauranne Lanz, Sui Ann Mao, Chris Hayward, Sumin Tang, Manuel Torres, Laura Brenneman, Dan Castro, and Diego Munoz. I'm especially grateful to Joey Neilsen, my office-mate, sounding board, and close friend. Aside from this group of Bostonians, I also want to thank Steve and Justin, Swati, Tomomi, Nastaran, Mangala, Joel, Toby, and Renee.

I couldn't have asked for a better crew of friends.

Thanks to my many teachers and mentors throughout the years: Brian McNamara, Valerie Young, Michael Moore, Saw Hla; all of you showed great patience with a noisy undergraduate who had too many ideas and too little knowledge to sort them out. Larry Curtis, you and Maj were such a delight. I learned a tremendous amount from you, and the paper we wrote together (guided very selflessly by you) was a landmark for me. Thank you so much Larry.

The Honors Tutorial College at Ohio University was a fantastic program and gave great preparation for graduate school and offered a wealth of opportunity to pursue research. Ann Fidler, Joe Shields, and Ann Brown were a great part of making such a good program for students in the department. But I want to single out Tom Statler, whose grit and commitment to his students and to scientific ethos is truly impressive. I am lucky to have grown up attending a wonderful public school system. Thank you to the teachers at Maumee City Schools, including Mr. Dreyfus, Mme Greenberg, Mr. Dick, Mr. Tadsen, Mrs. Healey, Mrs. Leach, Mr. Lowry, and especially Dave Jerman, a wonderful teacher and now a close friend.

Since I started working with Jeff, I have been fortunate to collaborate closely with a wonderful group of people. Lijun Gou, Ron Remillard, and Ramesh Narayan have been absolutely crucial to the work presented in this thesis. Lijun's tireless work ethic is impressive, and his always open door and ready ear have made collaborating together a real pleasure. Ron's tremendous ability with data is matched only by Ramesh's boundless knowledge of theory and scientific intuition. Ramesh's weekly group meetings with students and postdocs including Sasha Tchekovskoy, Bob Penna, Yucong Zhu, Jifeng Liu, C-K Chan, Akshay Kulkarni, Allison Farmer, Jon McKinney, Rebecca Shafee, Ryan Hickox, and others has been a highlight of my

time at CfA.

I am very grateful to the Astronomy Department at Harvard for making the CfA a wonderful place for a student to thrive. Thanks to Jean Collins, Donna Adams, Donna Wyatt, Charles Alcock, and Jim Moran for their support from on high. Peg Herlihy has been a godsend, and helped out in every way, especially this last year as Christina and I moved away and managed working remotely. Peg's moral and academic support has gone far above and beyond. My thanks to Irwin Shapiro, Avi Loeb, Doug Finkbeiner, Josh Grindlay, Julia Lee, Dave Charbonneau, Alyssa Goodman, and the faculty and scientists at CfA.

Lastly, I offer these words about my dear friend and advisor Jeff McClintock. Jeff's all around knowledge of X-ray science and every aspect of black hole behavior is truly remarkable. But more powerful still is his ability to inspire in others his enthusiasm and love for research, for black holes, and for science. He has been a bastion of support and wisdom throughout my time at CfA. Jeff and I have spent countless hours enthralled in the wonder of our black holes (and many other hours I treasure just as much exploring the tributaries of the mind). Jeff is unbelievably dedicated to the people and ideas he holds dear. Although he has always been overly busy in our more than five years of working together, Jeff's door has always been open. It wouldn't be right to say Jeff made time for us to meet, since that would convey completely the wrong sense of things. The time spent in our meetings was clearly a joy for Jeff, and that is one small but beautiful and telling aspect of what working with Jeff has been like. I could never have asked for or expected to have a mentor like Jeff. I am unbelievably fortunate. Jeff, I know we will continue to work together closely, and that knowledge eases the sting of how tremendously much I will miss spending my time with you.

Now, as Jeff will appreciate more than anyone, on to the science.

For Jeff

Chapter 1

Introduction

Adapted from J. F. Steiner, J. E. McClintock, R. Narayan, L. Gou *Proceedings of Science, HTRS 2011*, 2011, 019.

Astrophysical black holes are among the most important objects in the world of modern physics. They inhabit the unknown nexus between quantum mechanics and Einstein's relativity. At the same time, a black hole is remarkably simple. The no-hair theorem tells us that a black hole is described by just two numbers: its mass M and spin angular momentum $J \equiv a_* M^2 G/c$, where a_* is the dimensionless spin parameter that is bounded to lie in the range $-1 \leq a_* \leq 1$[1].

To understand the behavior of black holes, and ultimately to test general relativity in the strong field regime, it is essential that we establish reliable methods

[1]In principle, a black hole can have a third parameter, electric charge, but this is unlikely to be important in astronomical settings.

of measuring their spins. The importance of measuring spin is widely recognized. For example, the science cases for two of the three large space missions considered in the US Decadal Survey, namely *LISA* and *IXO*, featured the measurement of black hole spin as a primary science goal. The measurement of spin is likewise a key objective for X-ray missions that are nearing launch, including *Astro-H*, *GEMS*, and *ASTROSAT*.

Moreover, with the advent of Advanced LIGO, knowledge of black hole spin has become critical for calculating the expected gravitational waveforms from merging systems in which one or both objects are spinning black holes; measurements of spin are informing this work (Campanelli et al. 2006). Spin measurements are likewise being applied to problems in fundamental physics, e.g., Arvanitaki et al. (2010). Within astrophysics, spin data have provided the first observational evidence that relativistic jets can be powered directly by the spin energy of black holes (Narayan & McClintock 2012; Blandford & Znajek 1977). With modest improvements to current methodologies, it may soon be possible to test for violations of the no-hair theorem (see e.g., McClintock et al. 2011).

Currently, two means of measuring spin have been developed and applied: the continuum-fitting (CF; Zhang et al. 1997) and Fe $K\alpha$ (Fabian et al. 1989) methods. Each method has been used to estimate the spins of approximately ten stellar-mass black holes; the Fe $K\alpha$ method has additionally yielded the spins of about ten supermassive black holes in active galactic nuclei (AGN).

The foundation of both the CF and Fe $K\alpha$ methods is the existence of an innermost stable circular orbit (ISCO) for particles orbiting a black hole. Outside

the ISCO, the gas slowly spirals inward through a series of nearly circular orbits. Inside the ISCO, there are no stable orbits for the accreting gas, and so it plunges into the black hole on a dynamical timescale ($\lesssim$ 1ms for a stellar-mass black hole). As a result, the accretion disk is truncated at the ISCO. Therefore, by measuring the inner-disk radius, $R_{\rm in}$, we are equivalently determining the size of the ISCO radius, $R_{\rm ISCO}$.

Since the dimensionless ISCO radius $R_{\rm ISCO}/(GM/c^2)$, is a purely monotonic function of black hole spin, knowledge of $R_{\rm ISCO}/M$ equivalently gives the value of a black hole's spin (Figure 1.1). As spin increases from $a_* = 0$ to $a_* = 1$, the dimensionless ISCO radius decreases sharply from 6 to 1 (e.g., Bardeen et al. 1972). This large change in radius over the range of possible spins is what enables us to securely measure spin using estimates of $R_{\rm ISCO}/M$.

In the CF method, which is the focus of this thesis, one uses thermal continuum radiation from the accretion disk to measure $R_{\rm ISCO}/M$. In the principal alternative approach, the Fe $K\alpha$ method, one also measures $R_{\rm ISCO}/M$, but using line emission from the disk instead. The line emission, which is fluoresced over the disk's surface, experiences a strong gravitational redshift at the inner reaches of the disk. As a result, the full breadth of the observed line profile can be used to determine the quantity $R_{\rm ISCO}/M$ and thereby spin.

The remainder of this chapter is organized as follows. In Section 1.1, we discuss the CF method in more detail. In Sections 1.2–1.4 respectively we introduce the three central subjects of this dissertation: a new spectral model that has significantly extended the reach of the CF method; tests of two foundational assumptions of the

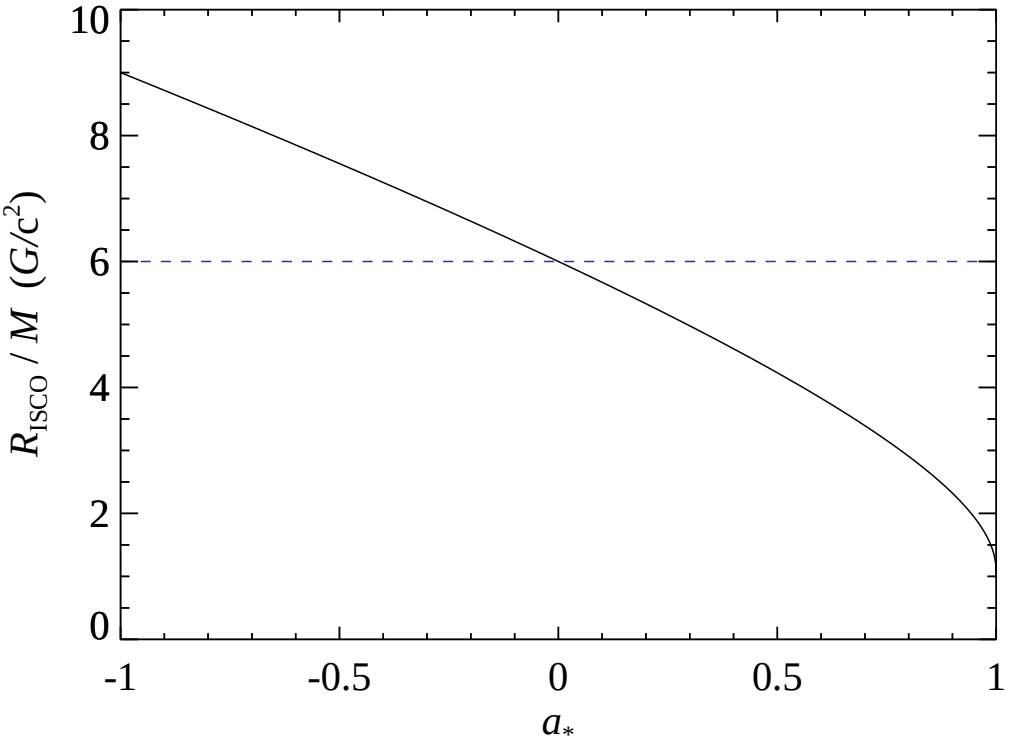

Figure 1.1.— The ISCO radius versus black hole spin. As spin changes from -1 to 0 to 1, the dimensionless ISCO radius $R_{\rm ISCO}/(GM/c^2)$ decreases from 9 to 6 to 1. A horizontal line marks the ISCO radius for $a_* = 0$, $R_{\rm ISCO} = 6GM/c^2$. Notice that the relationship is monotonic and nonlinear and that the scaling of $R_{\rm ISCO}/M$ with spin is steepest at the highest spin values.

method; and new CF measurements of spin for two black holes.

1.1 Continuum-Fitting Measurements of Spin

In the CF method one measures $R_{\rm ISCO}$ and determines spin by modeling the multitemperature thermal emission of the accretion disk. For the method to succeed, it is essential to have (1) a reliable theoretical model of the accretion disk; (2) accurate estimates of black hole mass M, disk inclination i, and source distance D; as well as (3) X-ray spectra that display a strong thermal component of emission. We discuss each of these three elements in turn.

1. The relativistic accretion disk model used is an elaborated and slightly-corrected version of the classic model of Novikov & Thorne (1973), which describes the thermal spectrum produced by a razor-thin accretion disk channeling gas onto a black hole. The model employed, which is referred to as KERRBB2 (Li et al. 2005; Davis & Hubeny 2006; McClintock et al. 2006), includes all relativistic effects and also includes the effects of limb-darkening, self-irradiation of the disk due to light bending, and the effects of spectral hardening.

2. Measuring $R_{\rm ISCO}$ is analogous to measuring the radius of a star (with known distance) from its observed flux and temperature. In this analogy, X-ray flux and temperature determine the solid angle of the disk, from which $R_{\rm ISCO}$ can be simply deduced if one knows D and the disk inclination i, which is usually assumed to be the same as the inclination of the orbital plane. Lastly, it is also

necessary to know M in order to obtain the dimensionless radius $R_{\rm ISCO}/M$, which is equivalent to knowing a_* (see Figure 1.1). The measurements of M, i and D are generally obtained by analyzing ground-based data obtained using optical and infrared instruments (e.g., Orosz et al. 2009).

3. Finally, one requires that the X-ray spectrum contain a strong thermal component. Usually, useful data is obtained in the *thermal-dominant* spectral state (Remillard & McClintock 2006), which is typified by soft disk emission and a relatively weak Compton power law. The only other strong requirement is that the disk must be well approximated by the razor-thin model employed. To achieve this, a luminosity restriction $L < 0.3\ L_{\rm Edd}$ is applied, where $L_{\rm Edd} = 1.26 \times 10^{38}\ (M/{\rm M}_\odot)$ erg s^{-1} is the Eddington limit (McClintock et al. 2006). Above this threshold, the disk scale-height flares beyond the thin disk regime and enters into a domain described by "slim-disk" models (e.g., Sądowski et al. 2011).

The CF method has so far been used to measure the spins of ten stellar-mass black holes. Those results are summarized in Table 1.1. Notably, all the spins are prograde ($a_* > 0$), and their values span the allowed range from 0 to 1.

1.2 Spectral Model

The spectra of accreting stellar-mass black holes reveal a ubiquitous high-energy power-law component of emission (e.g., Remillard & McClintock 2006). This power law is generally attributed to the Compton up-scattering of thermal accretion-disk

Table 1.1. Continuum-Fitting Spin Measurements

Black Hole	a_*	Reference
M33 X–7	0.84 ± 0.05	Liu et al. 2008, 2010
LMC X–3	0.3^a	Davis et al. 2006
LMC X–1	$0.92^{+0.04}_{-0.07}$	Gou et al. 2009
A0620–00	0.12 ± 0.19	Gou et al. 2010
4U 1543–47	0.8^a	Shafee et al. 2006
XTE J1550–564	$0.34^{+0.20\,b}_{-0.28}$	Chapter 7; Steiner et al. 2011
XTE J1655–40	0.7^a	Shafee et al. 2006
H1743–322	0.2 ± 0.3	Chapter 6; Steiner et al. 2012
GRS 1915+105	> 0.98	McClintock et al. 2006
Cyg X–1	> 0.95	Gou et al. 2011

Note. — Errors are 1σ.

[a] Value is provisional.

[b] Using both CF and Fe $K\alpha$ methods, the jointly-measured spin is $a_* = 0.49$.

emission by a hot ($\approx 10^9$ K) and optically thin outer atmosphere termed the "corona."

We adopt an empirical stance and develop a model for the effect of the corona on black hole spectra. Using the observed spectral shape of the component as a template, we assume that Compton-scattering occurs between thermal disk photons and coronal electrons. We assume that the system is generally symmetric with a scattering optical depth which is uniform and independent of the photon energy. In Chapter 2, we present the Comptonization model which results from these simple assumptions and implement a spectral fitting package for general use.

In Chapter 3, we apply the Comptonization routine to thermal accretion disk spectra to achieve a composite model of Comptonized accretion-disk emission and investigate the implications of this unified Comptonized-disk model. We study a range of spectral states to test the scope of our model and to empirically assess its performance. The composite model developed in these chapters will be employed in all later applications of continuum fitting throughout this dissertation, and has been applied to estimate the spins of half of the black holes in Table 1.1.

1.3 Foundations

1.3.1 The ISCO

The single most critical assumption underpinning current measurements of black hole spin is the asserted link between spin and $R_{\rm in}$; namely, the assumption that

the accretion disk terminates at the ISCO. Such a relationship naturally results from geometrically thin hydrodynamic accretion flows (Novikov & Thorne 1973; Shakura & Sunyaev 1973), but can in principle break down when the accretion disk is strongly magnetized or becomes geometrically thick.

The foundational assumption – that the ISCO corresponds to the disk's inner edge, and that $R_{\rm in}$ therefore maps directly to spin – is the basis for both the CF and Fe $K\alpha$ methods of measuring spin. This assumption is supported by recent general relativistic, magnetohydrodynamic simulations (GRMHD; Shafee et al. 2008; Penna et al. 2010; Kulkarni et al. 2011; Noble et al. 2011).

One consequence of the association of black hole spin and the ISCO radius is that in the thin-disk regime we consider, the inner-disk radius should be constant. It should not vary, e.g., with the brightness of the source. In Chapter 4, we explore the constancy of the inner radius empirically for the binary system LMC X–3, a persistent black hole which over the last three decades has been observed more regularly than nearly any other black hole source.

1.3.2 Spin-Orbit Alignment

The second crucial assumption of the CF method is that a black hole's spin angular momentum is aligned with the orbital angular momentum of the binary system. This expectation is grounded in knowledge that accretion torques acting over millions of years can readily cause alignment in stellar-mass black hole binary systems (e.g., Martin et al. 2008). However, while theoretically motivated, this supposed alignment has yet to be rigorously tested.

The black hole binary XTE J1550–564 (hereafter J1550) provides a unique opportunity to make such a test. J1550 is a poster-child microquasar system which underwent a violent outburst in 1998 followed by an atypical re-ignition and subsequent decay. During its outburst, J1550 launched a pair of superluminal jets. These jets were observed several years later in X-rays by Chandra, shocking against the ambient interstellar medium (Corbel et al. 2002), the first discovery of its kind.

By tracking the motion of the nearly pc-scale jets along the plane of the sky, in Chapter 5, we fit for the jet positions and solve for the jet inclination angle, which is presumed to match the angle of the spin-axis of J1550's black hole. Meanwhile, the binary inclination angle of the system has been previously measured by our group using optical and infrared light-curve and radial-velocity data (Orosz et al. 2011). We combine these two measurements and produce the first strong test for alignment along the line-of-sight.

1.4 New Spin Measurements

1.4.1 H1743–322

The microquasar H1743–322 (hereafter H1743), like J1550, also produced large-scale X-ray and radio jets. In Chapter 6, we analyze the motion of these jets on the plane of the sky (just as we did for J1550) and thereby determine the distance to H1743 and the inclination of the black hole's spin axis. Combining these measurements of D and i with our knowledge of the mass distribution for black holes in transient systems, we obtained an estimate of H1743's spin. This is the first time that the CF

method has been used to measure the spin of a black hole despite the absence of any dynamical constraints on the parameters D, i, and M – even the orbital period of H1743 is unknown.

1.4.2 XTE J1550–564: A Joint CF and Fe $K\alpha$ Study

J1550 is significant for having produced the first and most dramatic example of X-ray jets in a black hole microquasar, and for also having produced a resonant 3:2 pair of high-frequency quasi-periodic oscillations (QPOs; Remillard et al. 2002a; Sobczak et al. 2000b). These QPOs are thought to be produced in the innermost regions of the accretion disk and their frequencies are widely believed to depend on only the mass and spin of the black hole (e.g., Remillard & McClintock 2006, and references therein).

Because of the importance of J1550, we performed ground-based optical observations and derived new precise estimates for the binary parameters and distance ($M = 9.1 \pm 0.6$ $M_\odot$, $i = 74.7 \pm 3.8$ degrees, $D = 4.4 \pm 0.5$ kpc; Orosz et al. 2011). Building on these results, in Chapter 7, we determine J1550's spin via the CF method using ~ 50 *RXTE* spectra, and pay strict attention to all known sources of systematic error.

At the same time, in an effort to improve this CF measurement and to check the cross-consistency with the Fe $K\alpha$ method, we worked in collaboration with Fe $K\alpha$ experts to obtain an independent measurement of J1550's spin from the premier models of spectral reflection in black hole binaries. In Chapter 7, both CF and Fe $K\alpha$ results are presented in turn; ultimately, we combine the two measurements to

produce a combined estimate of J1550's spin.

Chapter 2

A Simple Comptonization Model

J. F. Steiner, R. Narayan, J. E. McClintock, & K. Ebisawa *Publications of the Astronomical Society of the Pacific*, Vol. 121, pp. 1279-1290, 2009

Abstract

We present an empirical model of Comptonization for fitting the spectra of X-ray binaries. This model, named SIMPL, has been developed as a package implemented in XSPEC. With only two free parameters, SIMPL is competitive as the simplest model of Compton scattering. Unlike the pervasive standard power-law model, SIMPL incorporates the basic features of Compton scattering of soft photons by energetic coronal electrons. Using a simulated spectrum, we demonstrate that SIMPL closely matches the behavior of physical Comptonization models which consider the effects of optical depth, coronal electron temperature, and geometry. We present fits to *RXTE* spectra of the black-hole transient H1743–322 and a *BeppoSAX* spectrum of

LMC X–3 using both SIMPL and the standard power-law model. A comparison of the results shows that SIMPL gives equally good fits, while eliminating the troublesome divergence of the standard power-law model at low energies. SIMPL is completely flexible and can be used self-consistently with any seed spectrum of photons. We show an example of how SIMPL – unlike the standard power law – teamed up with DISKBB (the standard model of disk accretion) provides a uniform disk normalization that is unaffected by moderate Comptonization.

2.1 Introduction

Spectra of X-ray binaries typically consist of a soft (often blackbody or bremsstrahlung) component and a higher-energy tail component of emission, which we refer to generically as a "power law" throughout this work. The origin of the power-law component in both neutron-star and black-hole systems is widely attributed to Compton up-scattering of soft photons by coronal electrons (White et al. 1995; Remillard & McClintock 2006, hereafter RM06). While this interpretation is not unique, in this work, we adopt the prevailing view that Compton scattering is the mechanism that generates the observed power law. This component is present in the spectra of essentially all X-ray binaries, and it occurs for a wide range of physical conditions.

The tail emission is generally modeled by adding a simple power-law component to the spectrum, e.g., via the model POWERLAW in the widely used fitting package XSPEC (Arnaud 1996). A few of the many applications where power-law models are employed include: modeling the thermal continuum (Narayan et al. 2008) or the

relativistically-broadened Fe K line (Miller et al. 2008b) in order to obtain estimates of black-hole spin; modeling the surrounding environment of compact X-ray sources, such as a tenuous accretion-disk corona (White & Holt 1982) or a substantial corona that scatters photons up to MeV energies (Gierliński et al. 1999); and classifying patterns of distinct X-ray states, e.g., in black-hole binaries (RM06).

Because of the importance of the power-law component, several physical models have been developed to infer the conditions of the hot plasma that causes the Comptonization. Models of this variety that are available in XSPEC are COMPTT (Titarchuk 1994), EQPAIR (Coppi 1999), COMPTB (Farinelli et al. 2008), BMC (Titarchuk et al. 1997), COMPBB (Nishimura et al. 1986), THCOMP (Życki et al. 1999), COMPLS (Lamb & Sanford 1979), and COMPPS (Poutanen & Svensson 1996). It is essential to use such physical models when one is focused on understanding the physical conditions and structure of a scattering corona or other Comptonizing plasma.

Often, however, the physical conditions of the Comptonizing medium are poorly understood or are not of interest, and one is satisfied with an empirical model that seeks to match the data with no pretense that the model can sufficiently discern the underlying physics. The model POWERLAW is one such empirical model which has been extraordinarily widely used in modeling black-hole and neutron-star binaries (see text & references in White et al. 1995; Tanaka & Lewin 1995; Brenneman & Reynolds 2006; RM06) and AGN (e.g., Zdziarski et al. 2002; Brenneman & Reynolds 2006). However, POWERLAW introduces a serious flaw: at low energies it rises without limit. The divergence at low energies, which is not expected for Comptonization, significantly corrupts the parameters returned by the model

component with which it is teamed (e.g., the widely used disk blackbody component DISKBB; Section 2.3).

An excellent alternative to the standard power-law model for describing Compton scattering is given by convolution using a scattering Green's function, formulated decades ago (Shapiro et al. 1976; Rybicki & Lightman 1979; Sunyaev & Titarchuk 1980; Titarchuk 1994). In this approach the power-law is generated self-consistently via Compton up-scattering of a seed photon distribution; consequently, the power-law naturally truncates itself as the seed distribution falls off at low energies.

In this chapter, we present our implementation of a flexible convolution model named SIMPL that can be used with any spectrum of seed photons. For a Planck distribution we show that SIMPL gives identical results to BMC, as expected since the two models are functionally equivalent (Section 2.2.5). Although SIMPL has only two free parameters, the same number as the standard POWERLAW, this empirical model is nevertheless able to very successfully fit data simulated using COMPTT, a prevalent physical model of Comptonization (Section 2.2.4). We analyze data for two black-hole binaries and illustrate the flexibility of SIMPL by convolving SIMPL with DISKBB, the workhorse accretion disk model which has been used for decades (Mitsuda et al. 1984). The principal result is that SIMPL in tandem with DISKBB enables one to obtain values for the disk-normalization parameter for more heavily Comptonized data that are consistent with those found for weakly-Comptonized data (see Section 2.3.2). The standard power law, on the other hand, delivers very inconsistent normalization values. This is shown in greater detail in (Steiner et al. 2009a).

In Section 2.2 we outline the model and in Section 2.3 we present a case study with several examples. We discuss a prospective application of the model in Section 2.4 and conclude with a summary in Section 2.5.

2.2 The Model: SIMPL

The model SIMPL (SIMple Power Law) functions as a convolution that converts a fraction of input seed photons into a power law (see eq. [2.1]). The model is currently available in XSPEC[1]. In addition to SIMPL-2, which is our implementation of the classical model described by Shapiro et al. (1976) and Sunyaev & Titarchuk (1980), which corresponds to both up- and down-scattering of photons, we offer an alternative "bare-bones" implementation in which photons are only up-scattered in energy. The physical motivations behind the two versions of the model are described in Section 2.2.1, and the corresponding scattering kernels — the Green's functions — are given in equation (2.3) and equation (2.4), respectively.

The parameters of SIMPL and the standard POWERLAW model are similar. Their principal parameter, the photon index Γ, is identical. However, in the case of SIMPL, the normalization factor is the scattered fraction $f_{\rm SC}$, rather than the photon flux. The goal of SIMPL is to characterize the effects of Comptonization as simply and generally as possible. In this spirit, all details of the Comptonizing medium, such as its geometry (slab vs. sphere) or physical characteristics (optical depth, temperature, thermal vs. non-thermal electrons), which would require additional

[1]see http://heasarc.nasa.gov/xanadu/xspec/manual/XSmodelSimpl.html

parameters for their description, are omitted.

It is appropriate to employ SIMPL when the physical conditions of the Comptonizing medium are poorly understood or are not of interest. When the details of the Comptonizing medium are known, or are the main object of study, one should obviously use other models (e.g., COMPTT, COMPPS, THCOMP, etc.), which are designed specifically for such work. SIMPL, on the other hand, is meant for those situations in which a Compton power-law component is present in the spectral data and needs to be included in the model but is not the primary focus of interest. SIMPL should thus be viewed as a broad-brush model with the same utility as POWERLAW but designed specifically for situations involving Comptonization.

By virtue of being a convolution model, SIMPL mimics physical reprocessing by tying the power-law component directly to the energy distribution of the input photons. The most important feature of the model is that it produces a power-law tail at energies larger than the characteristic energy of the input photons, and that the power law does not extend to lower energies. This is precisely what one expects any Compton-scattering model to do and is a general feature of all the physical Comptonization models mentioned above. In contrast, the model POWERLAW simply adds to the spectrum a pure power-law component that reaches all the way downward to arbitrarily low energies. The difference between SIMPL and POWERLAW is thus most obvious at soft X-ray bands where SIMPL cuts off in a physically natural way, as appropriate for Comptonization, whereas POWERLAW continues to rise without limit (e.g., see Yao et al. 2005).

Two assumptions underlie SIMPL. The first is that all soft photons have the

same probability of being scattered (e.g., the Comptonizing electrons are distributed spatially uniformly). This is a reasonable assumption when one considers that, even in the best of circumstances, almost nothing is known about the basic geometry of the corona. For example, usually the corona is variously and crudely depicted as a sphere, a slab, or a lamp post. The second assumption is that the scattering itself is energy independent. This is again reasonable given the soft thermal spectra of the seed photons that are observed for black-hole and neutron-star accretion disks, with typical temperatures of ~ 1 keV and a few keV, respectively. For example, in the extreme case of a 180° back-scatter off a stationary electron, a 3 keV seed photon suffers only a 1% loss of energy, and even a 10 keV photon loses only 4% of its initial energy.

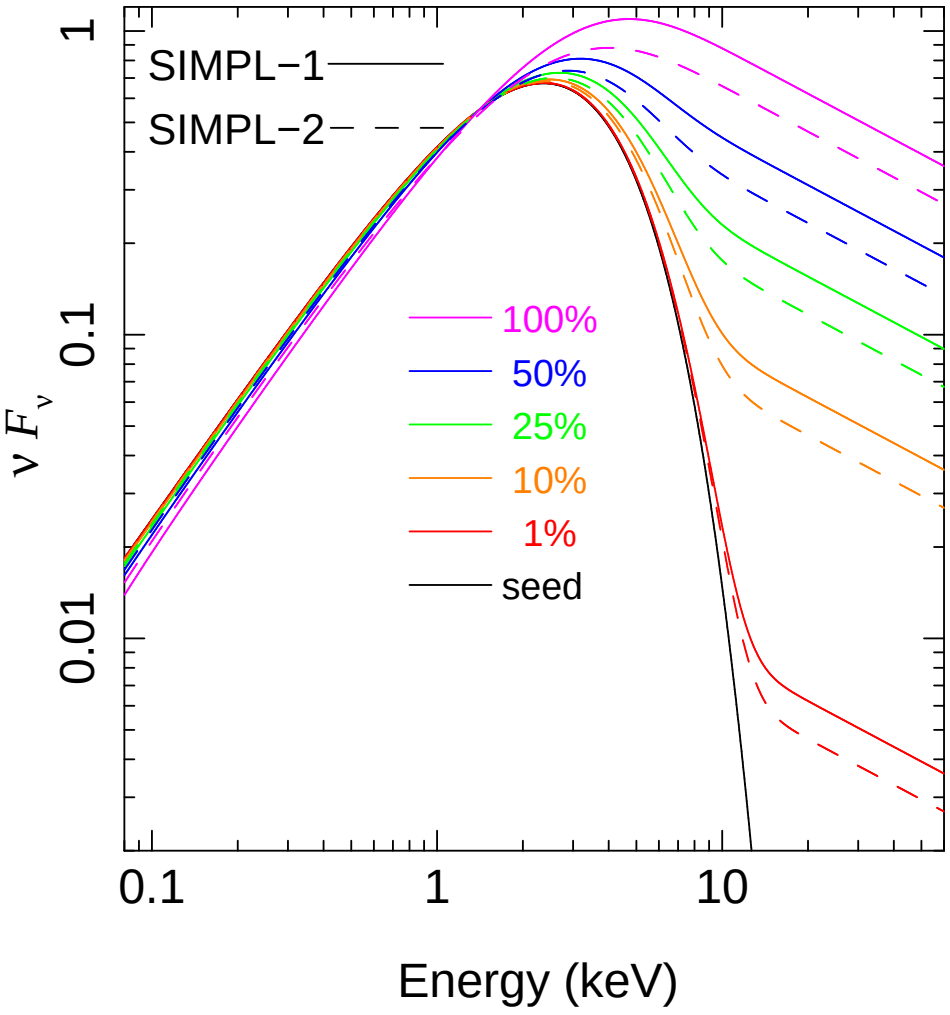

Figure 2.1.— Spectral energy density vs. photon energy for a sample spectrum calculated with SIMPL-1 (solid lines) and SIMPL-2 (dashed lines). The models conserve photons and Comptonize a seed spectrum, which in the case shown is DISKBB with $kT_* = 1$ keV (black line). Ascending colored lines show increasing levels of scattering, from $f_{\rm SC} = 1 - 100\%$.

Table 2.1. Results of Fitting a Simulated COMPTT Spectrum

MODEL	χ^2_ν/ν	$N_{\rm H}$ ($10^{22}{\rm cm}^{-2}$)	Γ	$f_{\rm SC}$	Norm(PL)[a]	kT_0 (keV)	Norm[b]	kT_e (keV)	τ_c
COMPTT[c]	···	0.1	···	···	···	1.	0.001	40.	2.
SIMPL-1 ⊗ BB	1.00/731	0.28 ± 0.01	1.41 ± 0.02	0.84 ± 0.01	···	1.142 ± 0.015	10.9 ± 0.4	···	···
SIMPL-2 ⊗ BB	1.06/731	0.31 ± 0.01	1.37 ± 0.02	0.87 ± 0.01	···	1.292 ± 0.010	7.8 ± 0.3	···	···
COMPBB	1.05/731	0.31 ± 0.01	···	···	···	1.292 ± 0.010	19.7 ± 0.7	43.6 ± 2.2	2.21 ± 0.03
BB+POWERLAW	2.02/731	0.68 ± 0.01	1.00 ± 0.01	···	$(5.0 \pm 0.2) \times 10^{-3}$	1.700 ± 0.008	0.89 ± 0.02	···	···

[a] POWERLAW normalization given at 1 keV in photons $s^{-1}cm^{-2}\,keV^{-1}$.

[b] BB and COMPBB normalization $= \left(\frac{R/{\rm km}}{D/10\ {\rm kpc}}\right)^2$ for a blackbody of radius R at a distance D; COMPTT normalization is undefined.

[c] COMPTT model set to disk geometry (geometry switch = 1).

Figure 2.1 shows sample outputs from SIMPL when the input soft photons are modeled by the multi-temperature disk blackbody model DISKBB (Mitsuda et al. 1984). Results are shown for both SIMPL-2 and SIMPL-1, our alternative version of SIMPL that includes only up-scattering of photons; the spectra are shown for $\Gamma = 2.5$ and a range of values of $f_{\rm SC}$. Note the power-law tails in the model spectra at energies above the peak of the soft thermal input and the absence of an equivalent power-law component at lower energies. This is the primary distinction between SIMPL and POWERLAW. SIMPL-2 and SIMPL-1 give similar spectra, but the spectrum from SIMPL-1 has a somewhat stronger power-law tail for the same value of $f_{\rm SC}$. This is because SIMPL-1 transfers all the scattered photons to the high energy tail, whereas SIMPL-2 has double-sided scattering. Therefore, for the same value of $f_{\rm SC}$, fewer photons are scattered into the high-energy tail with SIMPL-2. Correspondingly, when fitting the same data, SIMPL-2 returns a larger value of $f_{\rm SC}$ compared to SIMPL-1 (for examples, see Section 2.3 and Table 2.2).

2.2.1 Green's Functions

Given an input distribution of photons $n_{\rm in}(E_0)dE_0$ as a function of photon energy E_0, SIMPL computes the output distribution $n_{\rm out}(E)dE$ via the integral transform:

$$n_{\rm out}(E)dE = (1 - f_{\rm SC})n_{\rm in}(E)dE + f_{\rm SC}\left[\int_{E_{\rm min}}^{E_{\rm max}} n_{\rm in}(E_0)G(E;E_0)dE_0\right]dE. \qquad (2.1)$$

A fraction $(1 - f_{\rm SC})$ of the input photons remains unscattered (the first term on the right), and a fraction $f_{\rm SC}$ is scattered (the second term). Here, $E_{\rm min}$ and $E_{\rm max}$ are the minimum and maximum photon energies present in the input distribution, and $G(E;E_0)$ is the energy distribution of scattered photons for a δ-function input at

energy E_0, i.e., $G(E; E_0)$ is the Green's function describing the scattering.

Equation (2.1) assumes that every photon ultimately escapes to infinity, either unscattered (the first term on the right-hand side) or after Compton scattering (the second term). In the context of a disk-corona model we note that as much as half the scattered photons (the exact fraction depends on geometry) are redirected towards the disk. Computing the fate of these photons is the goal of sophisticated reflection models, e.g., REFLIONX (Ross & Fabian 2005) and PEXRAV (Magdziarz & Zdziarski 1995). Equation (2.1) ignores all these details and simply assumes that all the photons that return to the disk are effectively scattered from the surface with no change in energy. In the opposite extreme, we may wish to assume that all the returning photons are fully absorbed and thermalized. In this limit, we would replace equation (2.1) with:

$$n_{\rm out}(E)dE = (1 - f_{\rm SC})n_{\rm in}(E)dE + (f_{\rm SC}/2)\left[\int_{E_{\rm min}}^{E_{\rm max}} n_{\rm in}(E_0)G(E; E_0)dE_0\right]dE. \quad (2.2)$$

Clearly, the real situation is somewhere in between (2.1) and (2.2). The version of SIMPL currently implemented in XSPEC makes use of equation (2.1), though it would be straightforward to change it to equation (2.2).

We now describe the specific prescriptions we use for SIMPL-2 and SIMPL-1. We also discuss the physical motivations behind these prescriptions, drawing heavily on the theory of Comptonization as described by Rybicki & Lightman (1979, hereafter RL79).

2.2.2 SIMPL-2:

In sec. 7.7, RL79 discuss the case of unsaturated repeated scattering by nonrelativistic thermal electrons. Following Shapiro, Lightman, & Eardley (1976), they solve the Kompaneets equation and show that Comptonization produces a power-law distribution of photon energies (eq. 7.76d in RL79). There are two solutions for the photon index Γ:

$$\begin{aligned} \Gamma_1 &= -\frac{1}{2} + \sqrt{\frac{9}{4} + \frac{4}{y}}, \\ \Gamma_2 &= -\frac{1}{2} - \sqrt{\frac{9}{4} + \frac{4}{y}}, \end{aligned}$$

where the Compton y parameter is given by $y = (4kT_e/m_ec^2)\mathrm{Max}(\tau_{\rm es}, \tau_{\rm es}^2)$. Here, kT_e is the electron temperature and $\tau_{\rm es}$ is the optical depth to electron scattering. Up-scattered photons have a power-law energy distribution with photon index Γ_1 and down-scattered photons have a different power-law distribution with photon index Γ_2.

We model this case of nonrelativistic electrons with the following Green's function (Sunyaev & Titarchuk 1980; Titarchuk 1994; Ebisawa 1999), which corresponds to the model SIMPL-2:

$$G(E;E_0)dE = \frac{(\Gamma-1)(\Gamma+2)}{(1+2\Gamma)} \begin{cases} (E/E_0)^{-\Gamma} dE/E_0, & E \geq E_0 \\ (E/E_0)^{\Gamma+1} dE/E_0, & E < E_0. \end{cases} \tag{2.3}$$

The function is continuous at $E = E_0$, is normalized such that it conserves photons, and holds for all $\Gamma > 1$. Substituting (2.3) in (2.1) we see that SIMPL-2 has two parameters: $f_{\rm SC}$ and Γ. Note that although the model makes use of two power laws, their slopes are not independent.

As in the case of the standard power law, SIMPL includes no high energy cutoff. Technically, for any complete model of Comptonization, the up-scattered power-law distribution is cut off for photon energies larger than kT_e. To avoid increasing the complexity of our model, we have ignored this detail; extra parameters could easily be added to account for high energy attenuation if desired. By keeping the model very basic, SIMPL is a direct two-parameter replacement for the standard power law while bridging the divide between the latter model and physical Comptonization models.

2.2.3 SIMPL-1

The Green's function (2.3) is obtained by solving the Kompaneets equation, which assumes that the change in energy of a photon in a single scattering is small. This assumption is not valid when the Comptonizing electrons are relativistic.

In sec. 7.3 of their text, RL79 discuss Compton scattering by relativistic electrons with a power-law distribution of energy: $n_e(E_e)dE_e \propto E_e^{-p}dE_e$. In the limit when the optical depth is low enough that we only need to consider single scattering, they show that the Comptonized spectral energy distribution (SED) is a power law of the form $P(E)dE \propto E^{-(p-1)/2}$. Equivalently, the photon energy distribution takes the form $n(E)dE \propto E^{-\Gamma}$, with a photon index $\Gamma = (p+1)/2$. Hardly any photons are down-scattered in energy.

In sec. 7.5, RL79 show that repeated scatterings produce a power-law SED even when the relativistic electrons have a non-power-law distribution (see also Titarchuk & Lyubarskij 1995). In terms of $\tau_{\rm es}$ and the mean amplification of photon

energy per scattering A, the Comptonized photon energy distribution takes the form $n(E)dE \propto E^{-\Gamma}$ with a photon index $\Gamma = 1 - \ln \tau_{\rm es}/\ln A$. For the specific case of a thermal distribution of electrons with a relativistic temperature $kT_e \gg m_e c^2$, the amplification factor is given by $A = 16(kT_e/m_e c^2)^2$. Once again, hardly any photons are down-scattered.

For both cases discussed above, Comptonization is dominated by up-scattering and produces a nearly one-sided power-law distribution of photon energies. This motivates the following Green's function, valid for $\Gamma > 1$, which we refer to as the model SIMPL-1:

$$G(E;E_0)dE = \begin{cases} (\Gamma-1)(E/E_0)^{-\Gamma}dE/E_0, & E \geq E_0 \\ 0, & E < E_0. \end{cases} \tag{2.4}$$

The normalization factor $(\Gamma - 1)$ ensures that we conserve photons.

Although SIMPL-1 is most relevant for relativistic Comptonization, it can also be used as a stripped-down version of SIMPL-2 for non-relativistic coronae. The reason is that the low-energy power-law $(E/E_0)^{\Gamma+1}$ in equation (2.3) almost never has an important role. There is not much power in this component, and what little contribution it makes is indistinguishable from the input soft spectrum. Therefore, even for the case of nonrelativistic thermal Comptonization, for which the Green's function (2.3) is designed, there would be little difference if one were to use SIMPL-1 instead of SIMPL-2.

2.2.4 Comparison to COMPTT

To illustrate the performance of SIMPL relative to other Comptonization models, we have simulated a 2×10^6-count *BeppoSAX* (Boella et al. 1997) observation using the COMPTT model in XSPEC v12.4.0x.

For our source spectrum, we adopt disk geometry, a Wien distribution of seed photons at $kT_0 = 1$ keV, and a hydrogen column density of $N_{\rm H} = 10^{21}$ cm^{-2}. We set the optical depth and temperature of the Comptonizing medium to $\tau_c = 2$ and $kT_e = 40$ keV. Our simulation uses the LECS, MECS, and PDS detectors on *BeppoSAX*, which span a wide energy range $\sim 0.1 - 200$ keV (for details on the instruments, see Section 2.3). The total number of counts in the simulated spectra ($\sim 2 \times 10^6$) corresponds to a 3 ks observation of a 1 Crab source.

Table 2.2. Spectral Fit Results

					PHABS	SIMPL			DISKBB		POWERLAW	
Source State	Mission Detector	MJD	χ^2_ν/ν	$\frac{L_{\rm disk}}{L_{\rm Edd}}$[a]	$N_{\rm H}$ ($10^{22}{\rm cm}^{-2}$)	Ver.[b]	Γ	$f_{\rm SC}$	kT_* (keV)	Norm[c]	Γ	Norm(PL)[d]
H1743	*RXTE*	52797.6	1.11/44	0.21	1.89 ± 0.11	···	···	···	1.189 ± 0.010	564 ± 19	2.64 ± 0.02	9.77 ± 0.42
SPL	PCA		1.11/44	0.29	1.12 ± 0.10	S1	2.64 ± 0.02	0.169 ± 0.003	1.159 ± 0.008	867 ± 32	···	···
			1.11/44	0.30	1.15 ± 0.11	S2	2.64 ± 0.02	0.222 ± 0.004	1.164 ± 0.008	870 ± 33	···	···
H1743	*RXTE*	52811.5	0.93/44	0.24	1.50 ± 0.10	···	···	···	1.107 ± 0.004	864 ± 23	1.97 ± 0.03	0.51 ± 0.04
TD	PCA		0.93/44	0.25	1.44 ± 0.10	S1	1.98 ± 0.03	0.030 ± 0.001	1.105 ± 0.004	904 ± 24	···	···
			0.93/44	0.25	1.45 ± 0.10	S2	1.98 ± 0.03	0.037 ± 0.001	1.105 ± 0.004	906 ± 25	···	···
LMC X–3	*BeppoSAX*[e]	50415.5	1.05/729	0.58	0.073 ± 0.008	···	···	···	1.279 ± 0.011	24.5 ± 0.8	2.19 ± 0.11	0.055 ± 0.010
TD	LECS,MECS,		1.08/729	0.60	0.044 ± 0.003	S1	2.41 ± 0.45	0.062 ± 0.021	1.238 ± 0.013	30.4 ± 1.2	···	···
	PDS		1.08/729	0.59	0.044 ± 0.003	S2	2.46 ± 0.48	0.085 ± 0.033	1.239 ± 0.012	30.3 ± 1.1	···	···

[a]Bolometric $(0.1 - 20$ keV) luminosity of the disk component in Eddington units. For H1743, we adopt nominal values: $M = 10\ {\rm M}_\odot$, $D = 9.5$ kpc, and $i = 60°$. The fiducial values used for LMC X–3 are $M = 7.5\ {\rm M}_\odot$ and $i = 67°$ (Cowley et al. 1983; Orosz 2003). For fits using SIMPL, this quantity describes the seed spectral luminosity.

[b]Version of SIMPL being used, i.e., S1 for SIMPL-1 and S2 for SIMPL-2.

[c]For an accretion disk inclined by i to the line of sight, with inner radius $R_{\rm in}$ at distance D, Norm $= \left(\frac{R_{\rm in}/{\rm km}}{D/10\ {\rm kpc}}\right)^2 \cos i$.

[d]POWERLAW normalization given at 1 keV in photons ${\rm s}^{-1}{\rm cm}^{-2}\,{\rm keV}^{-1}$.

[e]The cross-normalizations for $C_{\rm LM} \equiv$ LECS/MECS and $C_{\rm PM} \equiv$ PDS/MECS are fitted from $0.7 - 1$ and $0.77 - 0.93$ respectively. $C_{\rm LM} = 0.802 \pm 0.283, 0.814 \pm 0.008, 0.813 \pm 0.008$ for the fits with POWERLAW, SIMPL-1, and SIMPL-2. $C_{\rm PM}$ is pegged at 0.93 for the same fits.

Note. — All errors are presumed Gaussian and quoted at 1σ.

We analyze the simulated data with a model consisting of a blackbody (BB) coupled with SIMPL. We refer to this model as SIMPL⊗BB (the ⊗ is to emphasize that SIMPL represents a convolution). The best fits achieved have reduced chi-squared values of $\chi^2_\nu = 1.00$ (SIMPL-1) and $\chi^2_\nu = 1.06$ (SIMPL-2). The fitted BB temperatures are respectively 1.14 ± 0.02 keV and 1.29 ± 0.01 keV compared to 1 keV in the original COMPTT model. Figure 2.2 shows the fit using SIMPL-1 and Table 2.1 lists the best-fit parameters for both models.

In comparison, COMPBB, an alternative model of Compton scattering that assumes slab geometry, fits our simulated spectrum comparably well as SIMPL, with $\chi^2_\nu = 1.05$ (Table 2.1). COMPBB returns the same temperature as SIMPL-2, $kT_{\rm bb} = 1.29 \pm 0.01$ keV. Compared to the COMPTT progenitor, COMPBB gives similar estimates of the coronal temperature kT_e and optical depth τ_c (Table 2.1). Even though COMPBB is a physically more realistic model of coronal scattering than SIMPL, it does not outperform SIMPL in terms of fitting the COMPTT-generated data. Meanwhile, the model BB+POWERLAW performs quite poorly, yielding $\chi^2_\nu > 2$. Parameters for this fit are given in Table 2.1. Note that the derived $N_{\rm H}$ using POWERLAW is much higher than either the original value or those from fits with SIMPL.

Though SIMPL is a purely empirical model, we see that it can deliver a remarkably successful fit to data simulated using the physical model COMPTT. Even for a very cool corona with electron temperatures as low as $kT_e = 20$ keV, which causes COMPTT to produce noticeable curvature in the high-energy spectrum, we find that SIMPL-2 and SIMPL-1 achieve reasonable fits with $\chi^2_\nu < 1.2$.

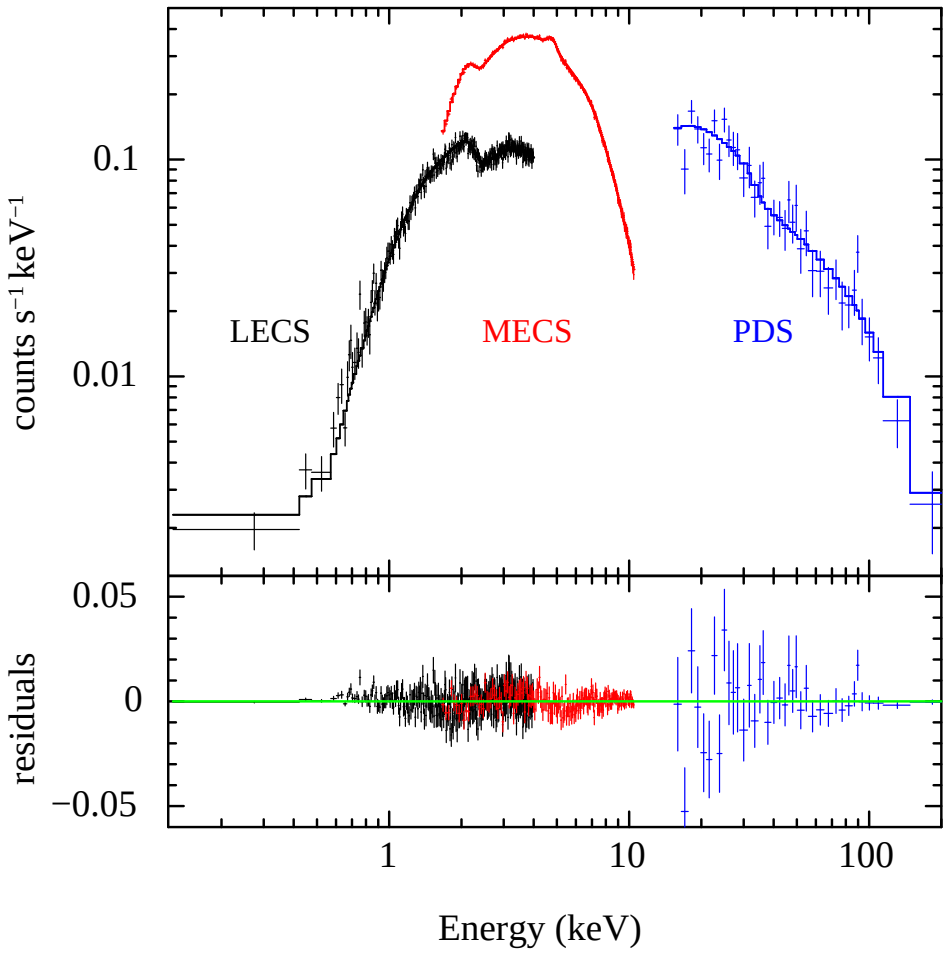

Figure 2.2.— The data correspond to a simulated *BeppoSAX* observation with a total of 2.1×10^6 counts; the spectrum was generated using COMPTT. The histogram shows the fit achieved using SIMPL-1. This fit is performed over the recommended energy ranges of the narrow-field instruments (NFI), as given by the Cookbook for *BeppoSAX* NFI Spectral Analysis, yielding $\chi^2_\nu = 1.00$. For details, see Table 2.1. This example demonstrates the ability of SIMPL to match a representative spectrum generated by a physical model of Comptonization.

A significant virtue of SIMPL relative to the physical Comptonization models in XSPEC is that SIMPL can be employed in conjunction with any source of seed photons. The physical models, on the other hand, are typically restricted to treating only one or two predefined photon distributions. One standard choice of continuum model that is widely used in fitting Comptonized accretion disks is DISKBB+COMPTT. With SIMPL, one would instead employ the model SIMPL⊗DISKBB. The latter not only generates the power law self-consistently via up-scattering of the seed photons, but it also has two fewer control parameters.

2.2.5 Bulk Motion Comptonization

The model BMC describes the Comptonization of blackbody seed photons by a converging flow of isothermal gas that is freely falling toward a compact object, i.e., bulk motion Comptonization (see, e.g., Shrader & Titarchuk 1998; Titarchuk et al. 1997). BMC is an alternative to coronal Comptonization models and is structured *identically* to SIMPL-2⊗BB; both models are specified with just four parameters. As a direct demonstration in XSPEC that SIMPL-2⊗BB and BMC are identical, we analyzed our simulated *BeppoSAX* spectrum described above using both models. We found that the returned values of the column density $N_{\rm H}$, the blackbody temperature kT, and the photon index Γ agreed in each case to four or more significant figures.

BMC has been variously used to support claims that Compton scattering off in-falling gas within several gravitational radii gives rise to the observed high energy power law in several black-hole binaries (e.g., Shrader & Titarchuk 1998, 1999; Borozdin et al. 1999). However, this is only one interpretation of the model;

SIMPL-2⊗BB, and therefore BMC, can equally be used to support a more standard model of coronal scattering (operating with uniform efficiency at all energies, see Section 2.2 and Section 2.2.3). Thus, although BMC is designed specifically to model relativistic accretion inflows, its function is actually quite general.

A virtue of SIMPL is that it fully incorporates the utility of BMC while allowing complete flexibility in the choice of the spectrum of seed photons, e.g., SIMPL⊗DISKBB is more appropriate for modeling Comptonization in accretion disks than BMC, which is hardwired to a Planck function.

The theory of bulk motion Comptonization is developed further and rigorously in Titarchuk et al. (1997). This paper describes a Green's function that is more appropriate than the one used in BMC. A complete version of this Green's function is incorporated into the more sophisticated model COMPTB. However, this model is again limited to treating scattering from a predefined set of (blackbody-like) seed photon distributions and includes additional free parameters. We find that the fitting results obtained using this Green's function are intermediate between those given by SIMPL-1 and SIMPL-2 so long as the temperature of the in-flowing electrons, kT_e, is above the observed energy range.

2.3 Data Analysis

In this section, we apply SIMPL to a sample of observations to illustrate how SIMPL compares with POWERLAW. To this end, we have selected two black-hole binaries, H1743–322 and LMC X–3. H1743–322 (hereafter H1743) is an ideal

black-hole transient for this exercise (see Remillard et al. 2006) since, for much of its 2003 outburst, its spectrum can be satisfactorily modeled with just absorbed ($N_{\rm H} \approx 2.2 \times 10^{22}{\rm cm}^{-2}$) thermal-disk and power-law components (McClintock et al. 2009, hereafter M09). In particular, the 122 days of contiguous spectral data on which we focus do not require any additional components to accommodate the reflection or absorption features that are often present in the spectra of black hole binaries.

The spectra of H1743 were acquired by the *Rossi X-ray Timing Explorer* (*RXTE*) PCU-2 module (Swank 1999), *RXTE*'s best-calibrated PCU detector, and were taken in "standard 2" format. All spectra have been background subtracted and have typical exposure times ~ 3000 s. A systematic error of 0.6% has been added to all energy channels. The resultant pulse-height spectra are analyzed from $2.8 - 25$ keV using XSPEC v12.4.0x (see M09 for further details).

While *RXTE* provides good spectral coverage in hard X-rays ($\gtrsim 10$ keV), which is most important for constraining the power-law component, it is not sensitive at low energies (< 2.5 keV). Therefore, *RXTE* data are generally insensitive to $N_{\rm H}$. To complement the *RXTE* observations presented here, we have selected a *BeppoSAX* observation of LMC X–3, a persistent and predominantly thermal black-hole source with a very low hydrogen column ($N_{\rm H} \approx 4 \times 10^{20}{\rm cm}^{-2}$; Page et al. 2003; Yao et al. 2005). In analyzing these spectra, we have left $N_{\rm H}$ free in order to best illustrate the systematic differences between fits achieved using SIMPL and POWERLAW.

The *BeppoSAX* narrow-field instruments provide sensitive measurements spanning a wide range in energy, from tenths to hundreds of keV. The low-energy

concentrator system (LECS) and the medium-energy concentrator system (MECS) probe soft fluxes, from $\sim 0.1-4$ keV and $\sim 1.5-10$ keV, respectively. The phoswich detector system (PDS) is sensitive to hard X-rays from $\sim 15-200$ keV, and the high-pressure gas scintillation counter (HPGSPC) covers $\sim 4-100$ keV. In this analysis, we consider only the LECS, MECS, and PDS because the statistical quality of the HPGSPC data is relatively poor.

In reducing *BeppoSAX* data, we have followed the protocols given in the Cookbook for *BeppoSAX* NFI Spectral Analysis (Fiore et al. 1999). We use pipeline products and extract spectra from $8'$ apertures centered on LMC X–3 for both the LECS and (combined) MECS detectors. For the PDS, which is a simple collimated phoswich detector, we selected the fixed rise-time spectrum. In our analysis, we have used standard response matrices and included blank-field background spectra with the appropriate scalings. No pile-up correction is necessary.

2.3.1 Steep Power Law State

About a third of the way through its nine-month outburst cycle, H1743 repeatedly displayed spectra in the steep power-law (SPL) state that were devoid of absorption features. A salient feature of the SPL state is the presence of a strong power-law component of emission. (For a review of black-hole spectral states and a precise definition of the SPL state, see Table 2 and text in RM06.)

Twenty-eight such featureless spectra were consecutively observed over a period of about three weeks (spectra Nos. 58–85; M09). We focus here on one representative spectrum, No. 77, whose spectral parameters (Γ, disk temperature

kT_*, and both POWERLAW and DISKBB normalizations) are quite representative of the values observed for the other 27 spectra (see M09). In Figure 2.3 we show our fits and the associated unabsorbed models obtained using DISKBB+POWERLAW and SIMPL⊗DISKBB. Fitted spectral parameters are presented in Table 2.2.

The quality of fit (as measured by χ^2_ν) using either model is comparable. Nevertheless, there are distinct differences between the models. The fits with SIMPL have a $\sim 50\%$ larger disk normalization compared to POWERLAW and a $\sim 40\%$ lower $N_{\rm H}$ (Table 2.2). The fit using POWERLAW diverges at low energies, as revealed by removing photoabsorption from the fitted models (panels on the right in Fig. 2.3). The effect is quite severe and has no obvious physical explanation. In contrast, the fit using SIMPL is well behaved and the unabsorbed model is not divergent.

2.3.2 Thermal Dominant State

The key feature of the thermal dominant (TD) state is the presence of a totally dominant and soft ($kT \sim 1$ keV) blackbody-like component of emission that arises in the innermost region of the accretion disk. The TD state is defined by three criteria, the most relevant of which here is that the fraction of the total 2–20 keV unabsorbed flux in the thermal component is $\geq 75\%$. For the full definition of this state, see Table 2.2 in RM06.

Here we have chosen H1743 spectrum #91 which belongs to a sequence of ∼50 featureless spectra (#86–136; M09) in the TD state. This spectrum has $\Gamma \sim 2$, which is somewhat harder than usual, but is otherwise typical of H1743's TD state. Spectral fit results are shown in Figure 2.4. In addition, in order to further illustrate

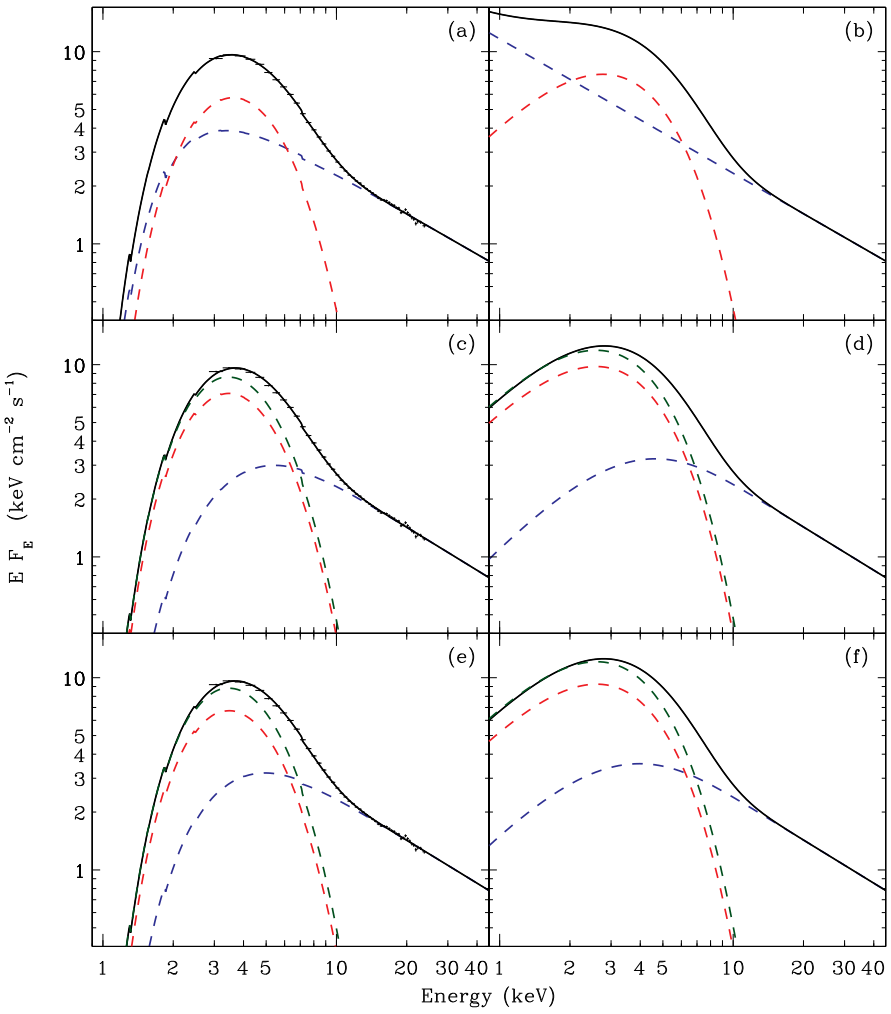

Figure 2.3.— *left:* Unfolded spectral fits to an *RXTE* observation of H1743 in the SPL state and *right:* the corresponding unabsorbed models. Data are fitted using *(a,b):* PHABS×(DISKBB+POWERLAW), *(c,d):* PHABS×(SIMPL-1⊗DISKBB), *(e,f):* PHABS×(SIMPL-2⊗DISKBB). The composite model is represented by a solid black line and the emergent disk and Compton components are shown as red and blue dashed lines respectively. The seed spectrum for SIMPL is shown (dashed) in green. Contrasting behaviors between SIMPL and POWERLAW are most clearly revealed in the unabsorbed models at low energies. Spectral parameters are given in Table 2.2.

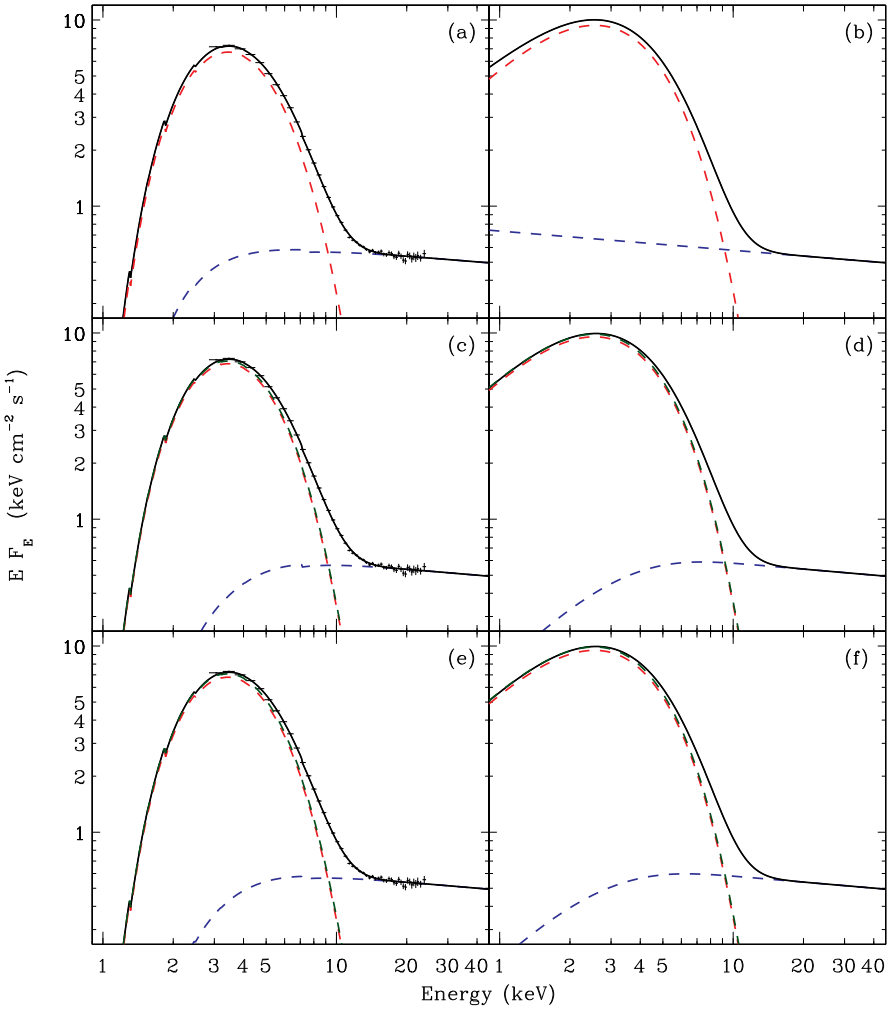

Figure 2.4.— Same as Figure 2.3 except that the results shown here are for an *RXTE* observation of H1743 in the TD state. The systematic differences between the SIMPL and POWERLAW fits are greatly reduced compared to the differences shown for the SPL example in Figure 2.3.

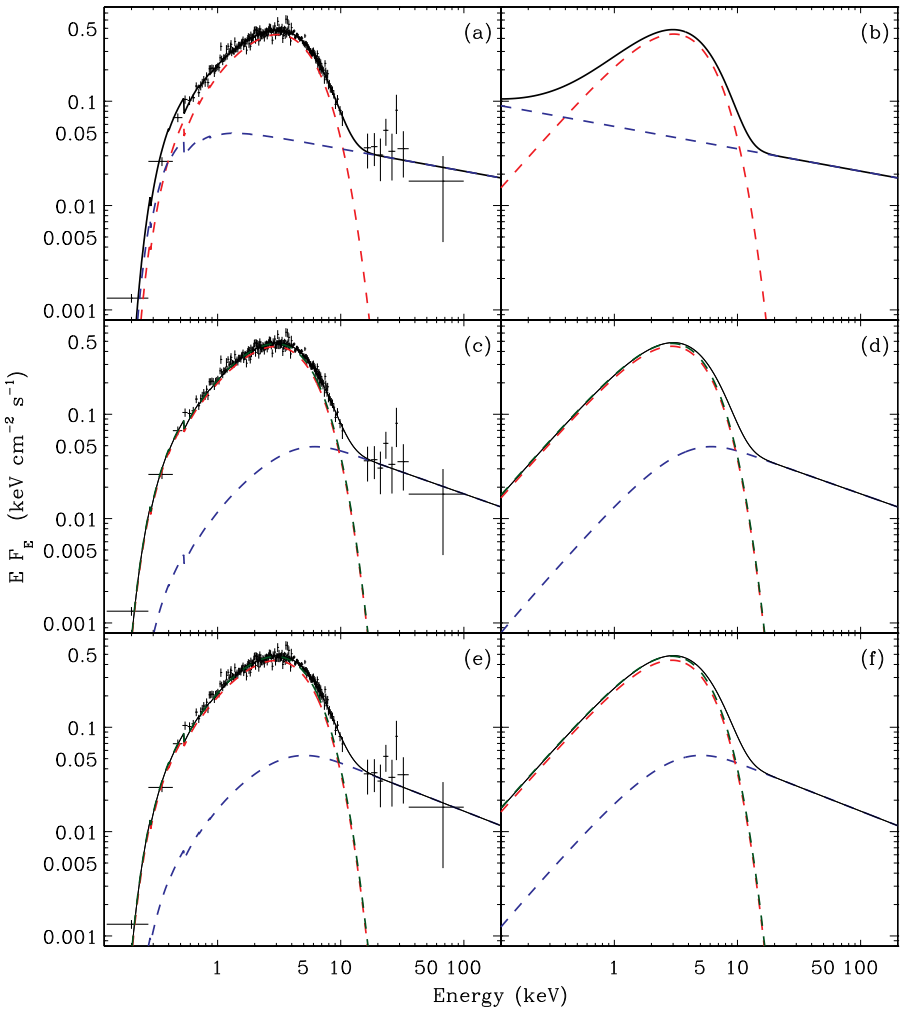

Figure 2.5.— Same as Figures 2.3 and 2.4 for a TD *BeppoSAX* spectrum of LMC X–3. The data have been rebinned for plotting purposes only and both LECS and PDS counts have been rescaled by the fitted normalizations given in Table 2.2. At low energies (below ∼0.5 keV), the unabsorbed model is strongly compromised for fits with POWERLAW

.

for the TD state the differences between SIMPL and POWERLAW at energies below the ≈ 2.5 keV response cutoff of *RXTE*, we use a *BeppoSAX* observation of LMC X–3; our results are illustrated in Figure 2.5. This observation was carried out on 1996 November 28 with exposure times of 1.8, 4.5, and 2 ks respectively for the LECS, MECS and PDS.

As in Section 2.3.1, we fit these data using DISKBB+POWERLAW and SIMPL⊗DISKBB. The best-fit spectral parameters are listed in Table 2.2. Due to a calibration offset between the various *BeppoSAX* instruments, we follow standard procedure and fit for the normalization of the LECS and PDS relative to the MECS, the best-calibrated of the three. We adopt the canonical limits of $0.7 - 1$ for LECS/MECS and $0.77 - 0.93$ for PDS/MECS. These normalizations are included in the tabulated results.

A comparison of the results obtained with POWERLAW and SIMPL confirms the trends highlighted in Section 2.3.1, namely the differences in normalization and $N_{\rm H}$. However, they are more modest here because the Compton component is weaker in the TD state.

2.3.3 Comparison of SIMPL and POWERLAW

An examination of Table 2.2 reveals the following systematic differences in the derived spectral parameters returned when fitting with SIMPL vs. POWERLAW: SIMPL yields (i) a stronger and softer thermal disk component, i.e., a larger normalization and lower kT_*; (ii) a generally steeper power law component (larger Γ); and (iii) a systematically lower $N_{\rm H}$. As we now show, all of these effects can be simply

understood.

Because POWERLAW produces higher fluxes than SIMPL at low energies, it tends to suppress the flux available to the (soft) thermal component, namely DISKBB in the examples given here. This explains why POWERLAW tends to harden the DISKBB component and to steal flux from it (i.e., reduce its normalization constant). Also, at low energies the POWERLAW component predicts high fluxes that, in order to conform to the observed spectrum, depress the value of Γ. These differences between SIMPL and POWERLAW are most pronounced when the power law is relatively steep, i.e., typically when $\Gamma \gtrsim 3$.

Modest and reasonable values of $N_{\rm H}$ are returned in fits using SIMPL, as well as COMPTT and other Comptonization models, because the Compton tail is produced by the up-scattering of seed photons and there is no power-law component at low energies. In contrast, POWERLAW continues to rise at low energies, which forces $N_{\rm H}$ to increase in order to allow the model to fit the observed spectrum. This systematic difference is apparent in our fit results for the H1743 spectra and is especially prominent in the case of the LMC X-3 spectrum for which $N_{\rm H}$ differs by a factor of two. For H1743, the discrepancy in $N_{\rm H}$ is much less for the TD spectrum than for the SPL spectrum because the SPL state has both a steeper and relatively stronger power-law component.

We turn now to consider the DISKBB normalization constant, which is proportional to $R_{\rm in}^2$, the square of the inner disk radius (see footnotes to Table 2.2). For the pair of H1743 spectra, we see that the disk normalization obtained with POWERLAW is $\approx$35% smaller in the SPL state than in the TD state (Table 2.2).

With SIMPL, on the other hand, there is no significant change in the normalization, and hence both the SPL and TD states can be modeled with a disk that has the same radius. Although we present here only one example comparing TD and SPL states, a more detailed analysis may be found in Steiner et al. (2009a). In that work, the full outburst of H1743 is analyzed with a relativistic disk model. Table 2.1 and Figure 2.2 there demonstrate that SIMPL is able to reconcile the derived values of the disk inner radius $R_{\rm in}$ for TD and SPL state spectra, whereas POWERLAW perfoms quite poorly in this regard.

Kubota & Makishima (2004) similarly identified a constant normalization for the black-hole binary XTE J1550–564 between the TD and SPL states in an analysis using the model DISKBB + THCOMP. Because THCOMP is implemented as an additive (i.e., non-convolution) model, Kubota & Makishima had to employ a somewhat ad hoc procedure to obtain their result (see their Appendix). Their work improved upon a similar result obtained for black-hole GRO J1655–40 (Kubota et al. 2001). With SIMPL, the modeling is significantly easier.

2.4 Discussion

A standard method of classifying X-ray states in black-hole binaries involves spectral decomposition into two primary components – a multi-temperature blackbody disk, DISKBB, and a Compton power law, POWERLAW (RM06). This method is compromised by the use of the standard power law when the photon index is large ($\Gamma \gtrsim 3$). In this case, at low energies the flux from the power law can rival or exceed the thermal component. As discussed in Section 2.2, intrusion of the Compton

component at low energies is fundamentally inconsistent with Compton scattering.

This difficulty in classifying states using POWERLAW is remedied by the use of SIMPL because the latter model naturally truncates the power-law component at low energies. It is useful to consider the intrinsic differences between the two models and how they influence the classification of black-hole X-ray states. Using POWERLAW, the thermal disk and tandem Compton emission are modeled independently. On the other hand, under SIMPL all photons originate in the accretion disk. Some of these disk photons scatter into a power law en route from the disk to the observer. As described in Section 2.3.3, fits employing SIMPL imply stronger disk emission and weaker Compton emission than those using POWERLAW. As a result, state selection criteria would need to be modified for classification using SIMPL. This topic is beyond the scope of this work.

2.5 Summary

We present a new prescription for treating Comptonization in X-ray binaries. While no new physics has been introduced by this model, its virtues lie in its simplicity and natural application to a wide range of neutron-star and black-hole X-ray spectra. SIMPL offers a generic and empirical approach to fitting Comptonized spectra using the minimum number of parameters possible (a normalization and a slope), and it is valid for a broad range of geometric configurations (e.g., uniform slab and spherical geometries). The scattering of a seed spectrum occurs via convolution, which self-consistently mimics physical reprocessing of photons from, e.g., an accretion disk. SIMPL has only two parameters, so it is straightforward to use it in place of

POWERLAW whenever one is dealing with Comptonization.

Our model is valid for all $\Gamma > 1$. We have shown that SIMPL is able to provide a good fit to a demanding simulated data set, which was generated with the widely-used Comptonization model COMPTT. Furthermore, we have demonstrated that SIMPL and POWERLAW give very comparable χ^2/ν when fitting spectral data (see Table 2.2). This quality of performance holds true not only for spectra with weak Compton tails (TD state) but also for spectra requiring a large Compton component (SPL state). In the latter case, the model based on SIMPL gives physically more reasonable results for the soft end of the spectrum (e.g., see Section 2.3.3).

Using SIMPL⊗DISKBB it will be important to revisit the classification of black hole states (RM06) for two reasons. First, the selection of TD data will no longer be adversely affected by the presence of a steep power-law component. Secondly, this model will allow some degree of unification of the TD state and SPL state, the latter being a more strongly Comptonized version of the former.

2.6 Appendix: XSPEC Implementation

SIMPL is presently implemented in XSPEC. This version includes three parameters (two that can be fitted), the power-law photon index (Γ), the scattered fraction ($f_{\rm SC}$), and a switch to set up-scattering only (SIMPL-1: switch > 0) and double-sided scattering (SIMPL-2: switch ≤ 0). Since SIMPL redistributes input photons to higher (and lower) energies, for detectors with limited response matrices (at high or low energies), or poor resolution, the sampled energies should be extended or resampled

within XSPEC to adequately cover the relevant range. For example, when treating the *RXTE* data in Section 2.3, which has no response defined below 1.5 keV, the command "energies 0.05 50 1000 log" was used to explicitly extend and compute the model over 1000 logarithmically spaced energy bins from $0.05 - 50$ keV.

Using SIMPL can be problematic when Γ is large, especially if the power-law component is faint or the detector response extends only to ~ 10 keV (e.g., *Chandra*, *XMM* or *ASCA*). When the photon index becomes sufficiently large, a runaway process can occur in which Γ steepens and the scattered fraction becomes abnormally high (typically $\gtrsim 50\%$, inconsistent with a weak power law). This occurs because scattering redirects photons from essentially a δ-function into a new function with characteristic width set by Γ. If Γ reaches large values ($\gtrsim 5$), the scattering kernel will also act like a δ-function, and the convolved spectrum will be nearly identical to the seed spectrum.

In such circumstances, we recommend bracketing Γ. In practice, the power-law spectral indices of black-hole systems are found to lie in the range $1.4 \lesssim \Gamma \lesssim 4$ (Remillard & McClintock 2006). An upper limit of $\Gamma \sim 4 - 4.5$ is typically sufficient to prevent this runaway effect, and this constraint should be applied if it is deemed appropriate for the source in question.

Chapter 3

Measuring Black Hole Spin via the X-ray Continuum Fitting Method: Beyond the Thermal Dominant State

J. F. Steiner, J. E. McClintock, R. A. Remillard, R. Narayan, & L. Gou *The Astrophysical Journal*, Vol. 701, pp. L83-L86, 2009[1]

[1]Reproduced by permission of the AAS.

Abstract

All prior work on measuring the spins of stellar-mass black holes via the X-ray continuum-fitting method has relied on the use of weakly-Comptonized spectra obtained in the thermal dominant state. Using a self-consistent Comptonization model, we show that one can analyze spectra that exhibit strong power-law components and obtain values of the inner disk radius, and hence spin, that are consistent with those obtained in the thermal dominant state. Specifically, we analyze many *RXTE* spectra of two black hole transients, H1743–322 and XTE J1550–564, and we demonstrate that the radius of the inner edge of the accretion disk remains constant to within a few percent as the strength of the Comptonized component increases by an order of magnitude, i.e., as the fraction of the thermal seed photons that are scattered approaches 25%. We conclude that the continuum-fitting method can be applied to a much wider body of data than previously thought possible, and to sources that have never been observed to enter the thermal dominant state (e.g., Cyg X–1).

3.1 Introduction

Black holes (BHs) are completely described by only three quantities: mass, charge, and spin. In astrophysical settings, any net charge will rapidly neutralize, with the result that a stellar-mass BH is specified by just its mass and spin. BH spin is commonly expressed in terms of the dimensionless parameter $a_* \equiv cJ/GM^2$ with $|a_*| \leq 1$, where M and J are respectively the BH mass and angular momentum, and

c and G are the speed of light and Newton's constant. While mass measurements of stellar-mass BHs have been made for decades, the first spin measurements have been achieved only during the past three years (Narayan et al. 2008; McClintock et al. 2006; Liu et al. 2008; Gou et al. 2009; Miller et al. 2009b, and references therein). Meanwhile, the spins of supermassive BHs have also been measured (Brenneman & Reynolds 2006; Miniutti et al. 2007). The only two methods presently available to measure BH spin are via modeling the thermal continuum spectrum of a BH accretion disk, as pioneered by Zhang et al. (1997), or by modeling the profile of a relativistically broadened Fe K fluorescence line, as demonstrated by Tanaka & Lewin (1995).

Spin is measured by estimating the inner radius of the accretion disk $R_{\rm in}$. One identifies $R_{\rm in}$ with the radius of the innermost stable circular orbit $R_{\rm ISCO}$, which is dictated by general relativity. $R_{\rm ISCO}/M$ is a monotonic function of a_*, decreasing from $6G/c^2$ to $1G/c^2$ as spin increases from $a_* = 0$ to $a_* = 1$ (Shapiro & Teukolsky 1983). This relationship between a_* and $R_{\rm ISCO}$ is the foundation of both methods of measuring spin.

In the continuum-fitting (CF) method, one determines $R_{\rm ISCO}$ by modeling the X-ray continuum spectrum, focusing on the thermal accretion-disk component. The observables are flux, temperature, distance D, inclination i, and mass M. To obtain reliable values of spin, it is essential to have accurate estimates for M, i and D, which are typically derived from optical data.

The CF method has been applied only to spectral data obtained in the thermal dominant (TD) state (or very recently to a near-TD intermediate state;

Gou et al. 2009). The TD state is chiefly characterized by the dominance of the soft, thermal disk component of emission. (For a measure of this dominance and a review of BH states, see Remillard & McClintock 2006.) The CF method has never been applied to the more Comptonized steep power law (SPL) state, which is characterized by the coexistence of a strong power-law component with photon index $\Gamma > 2.4$ and a significant thermal component. Most models for the SPL state invoke Compton up-scattering of thermal seed photons by coronal electrons as the mechanism that generates the power law. Herein, we employ a self-consistent Comptonized accretion-disk model that yields values of $R_{\rm in}$ for SPL-state spectra that are consistent with those obtained for TD-state spectra. This result greatly increases the reach of the CF method, allowing one to obtain reliable measurements of spin for a much wider body of data than previously supposed, and for sources that do not enter the TD state (e.g., Cyg X-1). Moreover, the success of this model supports the widely-held assumption that Comptonization is the mechanism which generates the observed high-energy power law component in SPL- and TD-state spectra.

Our full model of a Comptonized accretion disk is a convolution of the relativistic thin accretion-disk model KERRBB2 (Li et al. 2005; McClintock et al. 2006) and SIMPL, an empirical model that convolves a Comptonization Green's function with an arbitrary seed photon spectrum (Steiner et al. 2009b). Both models are implemented in XSPEC (Arnaud 1996). SIMPL, with only two parameters, ensures photon conservation and self-consistently generates the power-law component of the spectrum of an accreting BH using the accretion-disk component as input.

We have chosen to apply our spectral model to the two bright transient X-ray

sources H1743–322 (hereafter H1743), which we feature, and XTE J1550–564 (hereafter J1550). Both transients are sources of large-scale relativistic jets and high-frequency QPOs (Remillard & McClintock 2006, and references therein). For a detailed comparison of the spectral and timing characteristics of these very similar transients during their principal outbursts, see McClintock et al. (2009). Presently, the distance to J1550 is poorly constrained (see Orosz et al. 2002), and no useful distance estimate or dynamical information whatsoever is available for the black hole candidate H1743. Consequently, we cannot yet accurately estimate the spins of these black holes. In this work, we adopt fiducial values of M, i and D. Of course, $R_{\rm in}$ (and a_*) depend strongly on these fiducial values. However, as we show in Section 3.3.3, for any reasonable range of these input parameters, the dependence of $R_{\rm in}$ on luminosity or on time during the outburst cycle is slight, which is an important conclusion of this work.

We show that the very widely-used additive XSPEC models of Comptonization, namely the empirical model POWERLAW and the physical model COMPTT (Titarchuk 1994; Section 3.3), are inadequate for extracting measurements of spin from spectra with substantial power-law components. A self-consistent model such as SIMPL is required.

3.2 Observations & Analysis

We apply the model described below to the full archive of spectral data for the 2003 outburst of H1743 (the most intense observed for this source) and for all five outburst cycles of J1550 obtained using the Rossi X-ray Timing Explorer's (*RXTE*'s)

Proportional Counter Array (PCA; Swank 1999). We rely solely upon "standard 2" spectra obtained using the PCU-2 module, *RXTE*'s best-calibrated detector. All spectra have been binned into approximately half-day intervals, background subtracted, and have typical exposure times ~ 3000 s. For the first 5 weeks of PCA observations (through 2003 May 1 UT) the detector was pointed 0.32° from H1743. We have corrected the fluxes to full collimator transmission assuming a triangular response with FWHM = 1°. We applied similar collimator corrections ($\approx 0.1^\circ - 0.3^\circ$) to three observations of J1550 performed on 1998 September 7–8 and 1999 January 5 UT.

A 1% systematic error has been included over all channels to account for uncertainties in the response of the detector (details on *RXTE*'s calibration can be found in Jahoda et al. 2006). As in our earlier work (e.g., McClintock et al. 2006), we have corrected for detector dead time while using contemporaneous Crab observations and the canonical Crab spectrum of Toor & Seward (1974) in order to calibrate the PCA effective area. The resultant pulse-height spectra are analyzed from $2.8 - 25$ keV using XSPEC v12.5.0.

In XSPEC, the model we employ is PHABS(SIMPL⊗KERRBB2), where PHABS is a widely-used model of low-energy photoabsorption. SIMPL redirects photons from the seed distribution, described here by the accretion-disk model KERRBB2, into a Compton power law. Like POWERLAW, SIMPL has just two parameters: (1) the fraction of seed photons $f_{\rm SC}$ scattered into the power law, and (2) the photon power-law index Γ. SIMPL does not incorporate higher-order effects such as geometry-dependent scattering or reflection. The relativistic disk model KERRBB2 similarly has two fit parameters: (1) the spin parameter a_*, which we express equivalently

in terms of $R_{\rm in}$ (Section 3.1), and (2) the mass accretion rate $\dot{M}$. From these two parameters we compute the Eddington-scaled disk luminosity, $L_D(a_*, \dot{M})/L_{\rm Edd}$, where L_D is the luminosity of the seed photons and $L_{\rm Edd} \approx 1.3 \times 10^{38} M/{\rm M}_\odot$ erg s^{-1} (Shapiro & Teukolsky 1983). The low-energy cutoff is parameterized in the PHABS component by the column density $N_{\rm H}$, which we fix at $2.2{\times}10^{22}$ cm^{-2} for H1743 and $8{\times}10^{21}$ cm^{-2} for J1550 (McClintock et al. 2009; Miller et al. 2003). We include an additional model component to account for disk-reflection using the XSPEC model SMEDGE for J1550, which was not required for H1743.

In our analyses described in Sections 3.3.1 and 3.3.2, we adopt the following dynamical model parameters: For H1743, $M = 10$ M$_\odot$, $i = 60°$ and $D = 9.5$ kpc; and for J1550, $M = 10$ M$_\odot$, $i = 70°$, and $D = 5$ kpc. The values for H1743 are chosen arbitrarily to place the maximum outburst disk luminosity at $L_D/L_{\rm Edd} \approx 0.7$, and those for J1550 are round numbers based on the model described in Orosz et al. (2002). In Section 3.3.3, we allow i and D to vary and consider six disparate dynamical models.

For H1743 and J1550 we only select data over an order of magnitude in luminosity, between $0.05 < L_D/L_{\rm Edd} < 0.5$ for the values of M, i, and D given above. This intermediate range in luminosity is chosen in order to eliminate both hard-state spectra that have little or no detectable thermal component and high-luminosity data for which the thin-disk approximation likely no longer applies. Further requiring goodness-of-fit $(\chi^2/\nu) < 2$ and that the inner radius is well-determined ($R_{\rm in}/\Delta R_{\rm in} > 5$, where $\Delta R_{\rm in}$ is the 1σ statistical uncertainty on $R_{\rm in}$) leaves us with a total of 117 spectra for H1743 and 151 spectra for J1550.

We include for KERRBB2 the effects of limb darkening and returning radiation and set the torque at $R_{\rm in}$ to zero (e.g, McClintock et al. 2006), and for the dimensionless viscosity parameter we adopt $\alpha = 0.01$. (Our results in the following section are modestly affected if one instead uses $\alpha = 0.1$: $R_{\rm in}$ is increased by $\approx 5\%$ and becomes weakly dependent on luminosity, increasing by $\lesssim 10\%$ for an order of magnitude increase in L_D.) A color correction resulting from spectral hardening in the disk atmosphere is internally calculated for KERRBB2 using models KERRBB and BHSPEC (Davis & Hubeny 2006) as described in McClintock et al. (2006). The upscattering-only implementation of SIMPL, known as SIMPL-1, was used exclusively throughout unless otherwise noted. Larger values of $f_{\rm SC}$ are obtained using the double-sided scattering kernel SIMPL-2 (see Table 3.1), but $R_{\rm in}$ and the other fit parameters are completely unaffected by the choice of kernel.

3.3 Results

3.3.1 Final Selection of the Data via the Scattered Fraction

The scattered fraction $f_{\rm SC}$ sets the strength of the Compton power-law component relative to the disk. Figure 3.1 shows for H1743 the inner disk radius $R_{\rm in}$ versus $f_{\rm SC}$. For $f_{\rm SC} < 0.25$ the radius is quite stable and its value for the SPL data is very nearly the same as for the TD data. However, at large values of $f_{\rm SC}$ the inner disk radius $R_{\rm in}$ apparently recedes, indicating that either the model breaks down or a real change takes place in the disk. One possible physical explanation was proposed by Done & Kubota (2006), who argue that in regimes of extremely-high

Comptonization an inner disk corona can truncate the disk and increase $R_{\rm in}$ by tens of percent, consistent with the high values shown in Figure 3.1.

We have computed and compared plots of $R_{\rm in}$ versus $f_{\rm SC}$ for four BH binaries (H1743, J1550, XTE J1655–40, and LMC X–3) and find that divergent behavior in their values of $R_{\rm in}$ sets in for $f_{\rm SC} \gtrsim 0.2 - 0.3$ (or $f_{\rm SC} \gtrsim 0.25 - 0.4$ for SIMPL-2). Based on a consideration of these results, we adopt $f_{\rm SC} < 0.25$ as a data-selection criterion in this work. The application of this criterion leaves a final data sample of 100 spectra for H1743 and 136 for J1550.

3.3.2 Comparison with Other Comptonization Models

Having applied our Comptonized accretion disk model PHABS(SIMPL⊗KERRBB2) and obtained final data samples for H1743 and J1550 (Section 3.3.1), we now analyze these selected data using alternative models for the Compton component. We employ (1) COMPTT, a widely-used model of Comptonization that describes the up-scattering of blackbody-like radiation by coronal electrons (Titarchuk 1994), and (2) the empirical model POWERLAW. The full model formulations are respectively PHABS(KERRBB2+COMPTT) and PHABS(KERRBB2+POWERLAW). We now use these models to derive values of $R_{\rm in}$ for both sources and compare these results to those obtained using our model.

Figure 3.2 shows a side-by-side comparison of H1743 (left panels) and J1550 (right panels), where $R_{\rm in}$ is now plotted versus $L_D/L_{\rm Edd}$ (Section 3.2). The results in the upper pair of panels were obtained using our self-consistent Comptonization model SIMPL, while those in the lower panels were obtained using POWERLAW.

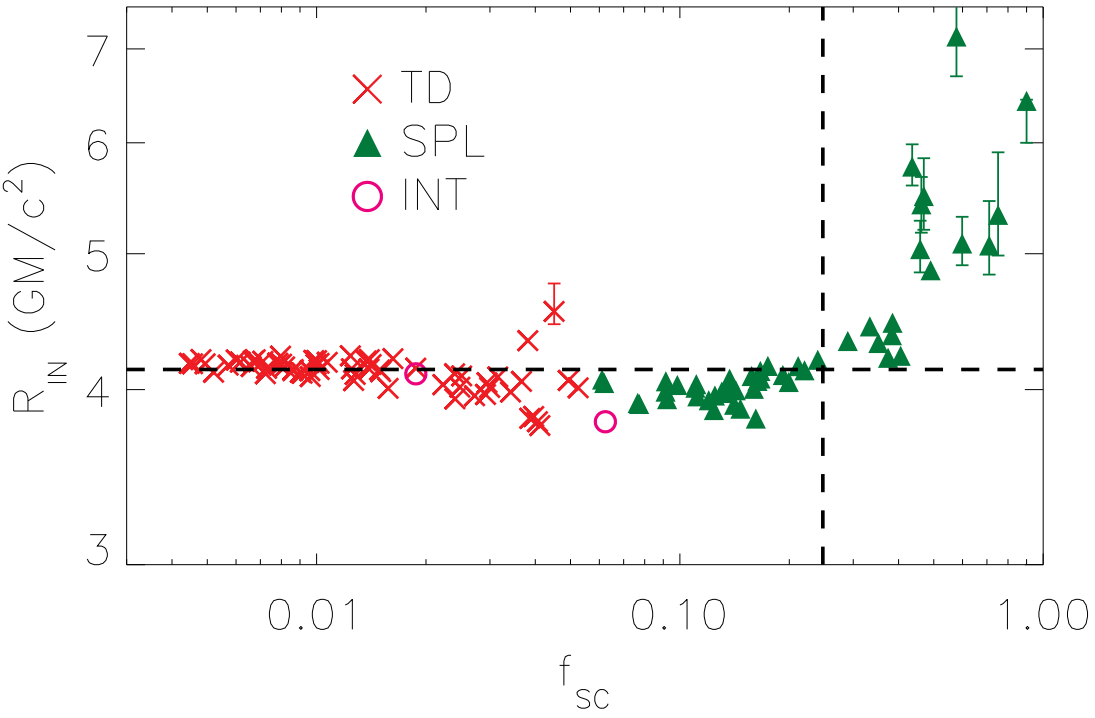

Figure 3.1.— The inner disk radius $R_{\rm in}$ versus the scattered fraction $f_{\rm SC}$ for H1743. As indicated in the legend, the symbol types denote X-ray state (see Remillard & McClintock 2006). For $f_{\rm SC} < 0.25$, which is our adopted selection criterion, $R_{\rm in}$ is generally constant; the median value for the TD-state data alone is indicated by the dashed line. However, for larger values of $f_{\rm SC}$, to the right of the vertical dashed line, the values of $R_{\rm in}$ diverge. Results are shown for all 117 spectra with $\chi^2/\nu < 2$ and $R_{\rm in}/\Delta R_{\rm in} > 5$ over the range $L_D = 5\% - 50\%\ L_{\rm Edd}$ (see Section 3.2). Error bars (1σ) on $R_{\rm in}$ that are smaller than the plotting symbols have been omitted for clarity. Error bars on $f_{\rm SC}$ are not shown; they are smaller than the plotting symbols except for extreme values of $f_{\rm SC}$ (< 0.02 and > 0.6).

Plainly, for both sources SIMPL harmonizes the extreme discord between the SPL/intermediate (INT) data and the TD data that results from analyzing these data using POWERLAW (Fig. 3.2*b* & *d*). The reconciliation achieved using SIMPL (Fig. 3.2*a* & *c*) indicates that the inner disk radii determined in the weakly-Comptonized TD state are very nearly the same as in the moderately-Comptonized INT and SPL states. Only data matching the selection criteria in Sections 3.2 and 3.3.1 are considered.

Table 3.1 provides a summary of the results shown in Figure 3.2 and extends the comparison by including results for COMPTT. Qualitatively, the results for both sources are very similar; here we comment only on the results for H1743. Comparing SIMPL with POWERLAW, we see that for the former model $R_{\rm in}$ is consistent between the TD and SPL states, 4.13 ± 0.05 and 4.01 ± 0.06, respectively (values and errors here are the median and median absolute deviation). On the other hand, POWERLAW delivers a radius for the SPL state that is $\approx 24\%$ smaller than for the TD state: 3.10 ± 0.24 versus 4.10 ± 0.06. While POWERLAW fails dramatically to reconcile the TD- and SPL-state data, COMPTT provides only a modest improvement, giving an $\approx 16\%$ smaller value of $R_{\rm in}$ for the SPL state: 3.46 ± 0.27 versus 4.10 ± 0.07. The failure of COMPTT and POWERLAW to deliver a constant radius occurs because these additive models compete with the disk component for thermal flux and because they make no allowance for the flux which the disk contributes to the power law.

Table 3.1. Comparison of $R_{\rm in}$ Across Spectral States

				$R_{\rm in}$ (in $\frac{GM}{c^2}$): KERRBB2 used with		
BH	State	N	$\overline{f_{\rm SC}}$[a]	SIMPL-1	POWERLAW	COMPTT [b]
H1743	TD	65	0.012	4.13 ± 0.05	4.10 ± 0.06	4.10 ± 0.07
	INT	2	0.062	3.79 − 4.10	3.48 − 4.02	3.73 − 4.08
	SPL	33	0.135	4.01 ± 0.06	3.10 ± 0.24	3.46 ± 0.27
J1550	TD	100	0.016	5.20 ± 0.06	5.05 ± 0.09	5.14 ± 0.10
	INT	18	0.183	5.16 ± 0.19	4.37 ± 0.57	4.93 ± 0.20
	SPL	18	0.123	5.00 ± 0.15	4.36 ± 0.21	4.91 ± 0.26

[a]Calculated for SIMPL-1. For fits using SIMPL-2, $\overline{f_{\rm SC}}$ is ≈30% larger.

[b]Geometry switch set to 1 (slab geometry) and redshift to 0. All other parameters are left free.

Note. — The values and errors quoted for $R_{\rm in}$ are medians and median absolute deviations (MADs); we have chosen these quantities for their robustness. For Gaussian-distributed data, $1\sigma \approx 1.5$ MAD. $R_{\rm in}$ is calculated using the fiducial M, i, and D specified in Section 3.2.

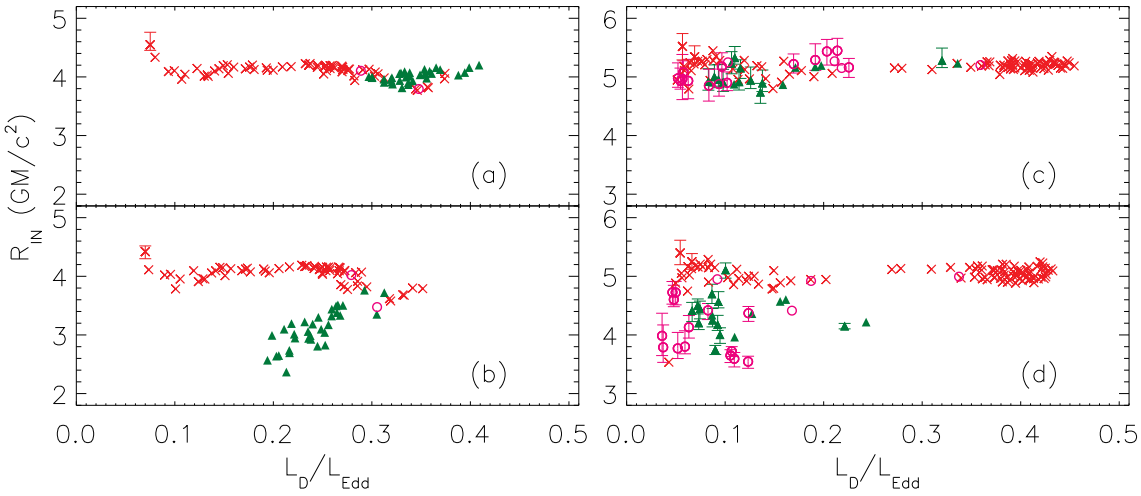

Figure 3.2.— The inner disk radius $R_{\rm in}$ versus the Eddington-scaled disk luminosity $L_D/L_{\rm Edd}$ for H1743 (left) and J1550 (right). Symbol types are defined in Fig. 3.1. For the upper pair of panels the Comptonization model employed is SIMPL and for the lower panels it is POWERLAW. The data sample considered here is that described in Section 3.3.1. For J1550 note in panel *c* the many INT-state data that are brought into agreement with the SPL- and TD-state data when applying SIMPL. Error bars are omitted when smaller than the symbols.

3.3.3 Dependence on the Dynamical Model

So far, our results are based on the specific and rather arbitrary dynamical model defined for each source in Section 3.2. We now demonstrate that the quality of our results does not depend on the choice of a particular triplet of M, i, and D. For H1743 we analyze the data for six disparate dynamical models chosen as follows: We fix the mass at $M = 10$ $M_\odot$ and vary the inclination from $i = 30°$ to $i = 80°$ in $10°$ increments, adjusting the distance in order to maintain the peak disk luminosity at $L_D/L_{Edd} \approx 0.7$; this prescription leaves our selection criteria (Sections 3.2 and 3.3.1) largely unaffected. For this demonstration we restrict ourselves to a contiguous set of pristine data that are free of both edge and line features (see McClintock et al. 2009).

Figure 3.3*a* shows a portion of the 2003 outburst light curve of H1743. Figure 3.3*b* shows corresponding values of R_{in} versus time for the six models described above. We draw the following key conclusions from Figure 3.3: (1) R_{in} is constant for each model to within $\approx 2\%$ as the source passes from the SPL state to the TD state, and as the source flux decays by a factor of ≈ 6. We furthermore note that R_{in} is stable during the two strong SPL-state flares that occur on days 75.6 and 79.5. (2) The character of the small systematic variations that occur in R_{in} during this entire 4-month period are essentially the same for all six models. For completeness, we recomputed all the results shown in Figure 3.3*b* using first $M = 5$ $M_\odot$ and then $M = 15$ $M_\odot$. Apart from offsetting the value of R_{in}, the character of these results is the same, including the level of scatter, as for the case of $M = 10$ $M_\odot$. We conclude that, apart from setting the median value of R_{in}, the choice of model has

no significant effect on the results presented in Figure 3.3.

Likewise, for J1550 we analyzed a $\sim$ 130-day stretch of data obtained during the 1998 outburst cycle (MJD 51110 – 51242; Sobczak et al. 2000a). We assumed fiducial values of M and i and explored a wide range of distances from $D = 3 - 8$ kpc. We obtained results very similar to those presented for H1743 (Figure 3.3*b*), consistent with an internal scatter of $\approx 2\%$.

3.4 Discussion

Kubota et al. (2001) and Kubota & Makishima (2004) present the first self-consistent treatment of disk-dominated accretion at high luminosity in black hole binaries. They showed for GRO J1655–40 and J1550 that what previously had appeared to be anomalous behavior was a natural result of strong inverse-Compton scattering. In particular, they demonstrated that the inner disk radius was stable when the flux attributed to the power law was properly associated with the disk. Their results have been confirmed recently by Steiner et al. (2009b) using SIMPL (Sections 3.1 and 3.2). In this chapter, we provide additional support for the work of Kubota et al., while supplying in this context the first relativistic analysis of the accretion disk component. Both the earlier work by Kubota et al. and this chapter demonstrate that, when modeling Comptonization, a self-consistent treatment is necessary in order to explain BH behavior across spectral states.

In all of our earlier work measuring the spins of BHs using KERRBB2, we have selected data with $L_{\rm D}/L_{\rm Edd} < 0.3$, which corresponds to the thin-disk limit

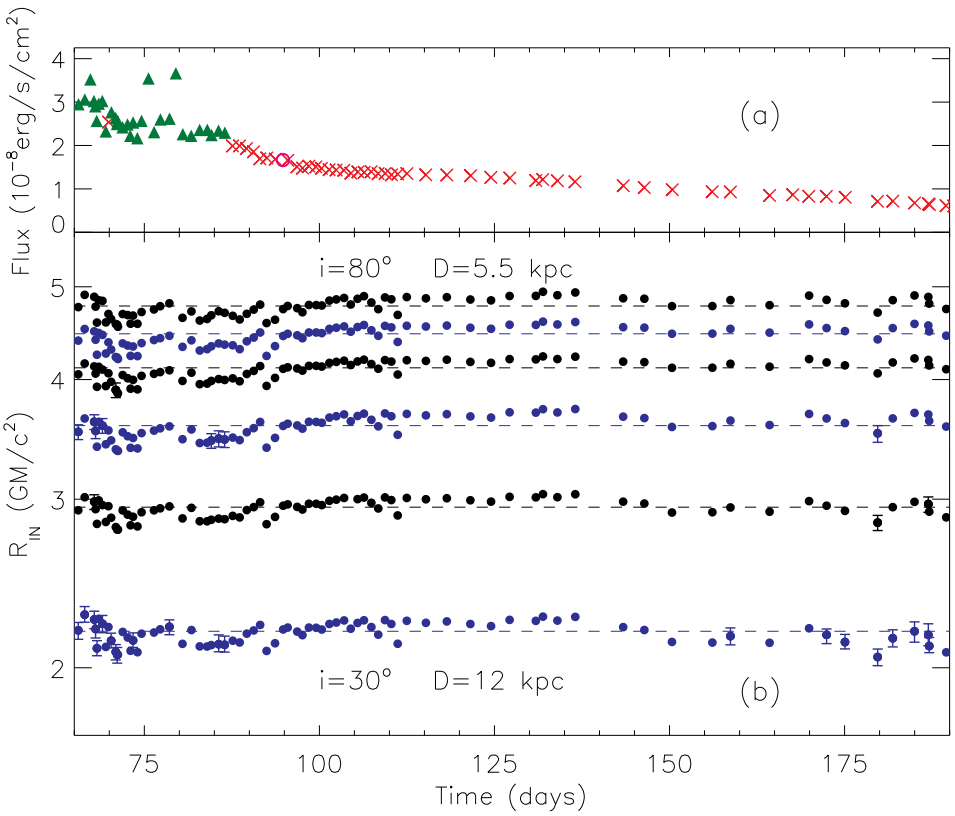

Figure 3.3.— (*a*) A contiguous 126-day portion of the 225-day *RXTE* PCA light curve of H1743, which is shown in full in Figure 3*a* of McClintock et al. (2009). The 2–20 keV unabsorbed fluxes were obtained by modeling the PCA spectral data. Time zero is the date of discovery of H1743 during its 2003 outburst, which occurred on 2003 March 21 (MJD 52719). (*b*) $R_{\rm in}$ versus time for the six models described in the text, shown as alternating black/blue tracks for clarity. The median absolute deviations for the extreme models with $i = 30°$ and $i = 80°$ are 2.2% and 1.8%, respectively. Fluxes for 83 spectra are plotted in panel *a* and 79 values of $R_{\rm in}$ are plotted in panel *b* (except for $i = 40°$ with 78); i.e., four (five for $i = 40°$) spectra failed to meet our selection criteria. Error bars are omitted where they are smaller than the symbols.

($H/R \lesssim 0.1$; McClintock et al. 2006). In the present work, the luminosity of J1550 is very uncertain and that of H1743 is unconstrained. For this reason, we present a broad range of luminosities, which likely exceeds the thin-disk limit. In work aimed at determining BH spin, when reliable distance estimates and dynamical data are available, one should apply the aforementioned luminosity restriction.

In conclusion, we have analyzed a selected sample of ~ 100 spectra for each of two bright transient sources using the self-consistent Comptonization model SIMPL convolved with a relativistic accretion disk model. We have thereby shown that the derived inner disk radii – or, equivalently, the derived spins of these BHs – remain stable to a few percent whether the source is in the TD state or the more strongly-Comptonized SPL state. We have further shown that this stability holds for $f_{\rm SC} \lesssim 0.25$ and for a wide range of input model parameters. We conclude that the continuum-fitting method of estimating BH spin can be applied to far more X-ray spectral data and more sources than previously thought possible.

Chapter 4

The Constant Inner-Disk Radius of LMC X–3: A Basis for Measuring Black Hole Spin

J. F. Steiner, J. E. McClintock, R. A. Remillard, L. Gou, S.-Y. Yamada, & R. Narayan *The Astrophysical Journal*, Vol. 718, pp. L117-L121, 2010[1]

Abstract

The black-hole binary system LMC X–3 has been observed by virtually every X-ray mission since the inception of X-ray astronomy. Among the persistent sources, LMC X–3 is uniquely both habitually soft and highly variable. Using a fully relativistic

[1]Reproduced by permission of the AAS.

accretion-disk model, we analyze hundreds of spectra collected during eight X-ray missions that span 26 years. For a selected sample of 391 *RXTE* spectra we find that to within ≈ 2 percent the inner radius of the accretion disk is constant over time and unaffected by source variability. Even considering an ensemble of eight X-ray missions, we find consistent values of the radius to within $\approx 4-6$ percent. Our results provide strong evidence for the existence of a fixed inner-disk radius. The only reasonable inference is that this radius is closely associated with the general relativistic innermost stable circular orbit (ISCO). Our findings establish a firm foundation for the measurement of black hole spin.

4.1 Introduction

The X-ray binary LMC X–3 was discovered by *Uhuru* in 1971 (Leong et al. 1971). Observations of its B3V optical counterpart revealed an orbital period of 1.7 days and a mass function of 2.3 ± 0.3 $M_\odot$. Because of its massive companion star, this established LMC X–3 as a strong dynamical black-hole (BH) candidate (Cowley et al. 1983; Kuiper et al. 1988). Subsequent X-ray observations spanning decades have revealed a complex behavioral pattern that includes transitions between soft and hard states (Wilms et al. 2001) and long-term ($\gtrsim 100$ d) variability cycles (Cowley et al. 1991). While by some metrics LMC X–3 is a nearly archetypal BH binary, its combined qualities of persistence and strong variability set it apart as unique.

Among the black hole systems, LMC X–3 bridges the divide between low-mass X-ray binaries powered by Roche-lobe overflow and wind-fed, high-mass X-ray

binaries (Soria et al. 2001). The former are transients, usually locked in a deep quiescent state, whereas the latter systems are persistently X-ray bright. Among the classical persistent BH sources (Cyg X–1, LMC X–1, and LMC X–3), LMC X–3 habitually shows the softest X-ray spectrum, reaches the highest luminosity, and exhibits the largest variations in intensity.

Because of its persistence LMC X–3 has been observed by nearly every X-ray astronomy mission. In this chapter, we apply our relativistic accretion disk model (KERRBB2; McClintock et al. 2006) to essentially all available X-ray data in order to examine the presumed constancy of the inner radius of the BH's accretion disk. We draw upon data collected by eight missions, with *RXTE* providing the lion's share.

For thin accretion disks, recent MHD simulations provide support for identifying the inner-disk radius $R_{\rm in}$ with the radius of the innermost stable circular orbit $R_{\rm ISCO}$ (Reynolds & Fabian 2008; Shafee et al. 2008; Penna et al. 2010; but see Noble et al. 2009), a proposition that has a long history of theoretical and observational support (e.g., see Section 6 in Gou et al. 2009). With this identification and the simple monotonic relationship between $R_{\rm ISCO}$ and the BH spin parameter (Shapiro & Teukolsky 1983), a measurement of $R_{\rm in}$ is equivalent to a measurement of the spin of the BH. This is the basis for both the continuum-fitting (Zhang et al. 1997) and Fe-K (Fabian et al. 1989) methods of measuring spin. In recent years, both methods have been used to estimate the spins of stellar BHs (e.g., Shafee et al. 2006; McClintock et al. 2006; Davis et al. 2006; Reis et al. 2008; Miller et al. 2009b; Blum et al. 2009).

The mass of LMC X–3's BH primary is presently very uncertain (Cowley 1992),

and we adopt a round value that is typical for BH binaries of $M = 10$ $M_{\odot}$. For the inclination we adopt the provisional value $i = 67°$ (Kuiper et al. 1988). Because of the uncertainties in both M and i, in this chapter we do not attempt to estimate the BH's spin. Rather, we assume a reasonable value for the mass and employ the X-ray continuum-fitting method in order to study the constancy of $R_{\rm in}$. We describe our data set comprised of hundreds of multi-mission spectra in Section 4.2, our analysis in Section 4.3, and present our results in Section 4.4. In Section 4.5, we explore the systematics associated with our spectral model and conclude by discussing our results in the context of ongoing studies of BH spin.

4.2 Observations

RXTE: The *Rossi X-ray Timing Explorer* (*RXTE*) is our workhorse instrument, providing a total gross sample of 712 spectra. Individual spectra were defined by grouping all the archival pointed data from 1996 through 2009 into approximately half-day bins with $\approx 90\%$ of exposure times ranging from 1–10 ks. We only use pulse-height spectra obtained by the best-calibrated PCA detector, PCU-2 (Jahoda et al. 2006). Count rates have been renormalized to correct for detector dead time and a systematic error of 1% has been included to account for uncertainty in the instrumental response (Jahoda et al. 2006). These data have been analyzed from 2.55–25 keV over all reliable gain epochs ($\geq$ epoch 2). Here and elsewhere, the analysis work has been performed using XSPEC v.12.5.1o (recent enough that an early coding error in kerrbb has been fixed[2]; Arnaud 1996).

[2]http://heasarc.nasa.gov/docs/xanadu/xspec/issues/archive/issues.12.5.0an.html

EXOSAT: Seven observations from 1983–1984 were obtained via the HEASARC archive[3]; only data from the ME instrument are currently available. Spectra were extracted as described in Treves et al. (1988) and analyzed from 1–25 keV. The customary systematic error of 1% was included.

Ginga: The LAC detector observed LMC X–3 on 18 occasions during 1987–1990. To extract these spectra, we followed the procedures described in Ebisawa et al. (1993). Each spectrum has been analyzed from 1.5-25 keV with a 1% systematic error included.

ASCA: LMC X–3 was observed twice, once on UT 1993 September 22 and later on UT 1995 April 14. We extracted and separately combined spectra from the two GIS and two SIS instruments. Data were calibrated relative to the GIS-2 detector and analyzed from 0.8-9 keV(GIS) and 0.6-9 keV(SIS) using a 2% systematic uncertainty.

BeppoSAX: Following the standard reduction guide (Fiore et al. 1999), we have generated spectra for the narrow-field instruments from each of the 23 available observations. We extracted spectra using $8'$ apertures in the imaging instruments and used a fixed rise-time threshold for the PDS. For each observation we employed all usable LECS, MECS, and PDS data. Throughout, we adopted the standard inter-detector floating normalizations calibrated relative to the MECS. Data were analyzed from 0.12–4 keV (LECS), 1.65–10 keV (MECS) and 15–80 keV (PDS). A 1% systematic error has been included.

XMM-Newton: All photon-counting data were severely piled up and therefore

[3]http://heasarc.nasa.gov

rejected because of uncertainties in the flux calibration. We use the single available 19 ks timing-mode observation of LMC X–3 obtained on UTC 2000 November 25. Because of the large number of accumulated counts, $\sim 2 \times 10^6$, uncertainties in the response of the detector are dominant, and we therefore included a 3% systematic error and fitted over $0.5 - 10$ keV. Reduction and processing has been performed using *XMM* SAS v9.0.0[4].

Swift: The sole XRT windowed-timing mode observation of LMC X–3, taken on UTC 2007 November 26, has been procured and analyzed following the procedures outlined in Capalbi et al. (2005). We rejected all the photon-counting data because they suffer from extreme pile-up. Calibration version 11 files have been used for the data reduction. In consultation with the *Swift* Help Desk, we have included an extra model component to account for an instrumental artifact near the Si edge around 1.7 keV. Analysis has been conducted over 0.4–10 keV using a 1% systematic error.

Suzaku: Two observations were made on Dec. 22 2008 and Dec. 21 2009 (UT). The Suzaku attitude calibration was improved using the *AEattcor* routine[5]. We applied the appropriate reduction procedures for a bright point source[6]. Pile-up was kept well below $\sim 3\%$ by excluding the innermost $10''$ and $30''$ for the 2008 and 2009 observations, respectively. In all other respects, we have followed the methods of Kubota et al. (2010), including using their energy intervals and adopting a 1% systematic error. A fixed cross-normalization of 1.16 is used between XIS and

[4]http://xmm.esac.esa.int/sas/

[5]http://space.mit.edu/CXC/software/suzaku/

[6]http://www.astro.isas.ac.jp/suzaku/analysis/xis/pileup/HowToCheckPileup_v1.pdf

HXD-PIN detectors (Maeda 2008).

4.2.1 Flux Calibration

Just as deducing the radius of a star from its spectrum requires knowledge of its luminosity, in order to estimate the inner radius of an accretion disk it is also necessary to determine its luminosity. However, the measurement of X-ray luminosity is problematic in X-ray astronomy because of the significant flux-normalization differences, often $\gtrsim$10%, between missions. We address this issue by using the power-law spectrum of the Crab Nebula as measured by Toor & Seward (1974): $\Gamma = 2.1$ and $N = 9.7$ photons s^{-1} keV^{-1} at 1 keV.

For each mission considered herein (excepting *Swift*; see Table 1), we either rely on the Crab calibration performed by the instrument team, or we compute a correction to the effective area by comparing the spectrum predicted by Toor & Seward (1974) to parameters obtained by analyzing proximate, archival observations of the Crab. Toor & Seward normalization coefficients $f_{\rm TS}$ and slope differences $\Delta\Gamma_{\rm TS}$ are presented for each mission in Table 1. This table also summarizes for LMC X–3 the gross number of observations available from each mission, $N_{\rm obs}$, as well as the number of observations that meet our selection criteria, $N_{\rm sel}$ (Section 4.3.1).

4.3 Analysis

At energies above $\sim 5 - 10$ keV, the spectra of BH binaries in all states show a contribution from a power-law component. This power law is widely attributed

to inverse-Compton scattering of thermal disk photons by hot coronal electrons. The power-law model we employ, SIMPL, generates this Compton component by upscattering seed photons from the thermal component (Steiner et al. 2009b).

The thermal and principal component of our model is KERRBB2, a thin accretion disk model that includes all relativistic effects, self-irradiation of the disk ("returning radiation"), limb darkening, and the effects of spectral hardening (Li et al. 2005; McClintock et al. 2006). During analysis, this latter effect is handled on the fly via a look-up table of the spectral hardening factor f for a given value of the disk viscosity parameter α (we adopt $\alpha = 0.01$ as default). These tables were computed using BHSPEC, a second relativistic disk model (Davis et al. 2006; Davis & Hubeny 2006).

Our fit to the thermal component of the spectrum effectively determines the solid angle subtended by the accretion disk: $\Omega = \pi(R_{\rm in}/D)^2 \cos i$, where D is the distance and i is the inclination of the accretion disk with respect to the line of sight. For D we use the average distance to the LMC, $D = 48.1$ kpc (e.g., Orosz et al. 2009), while for inclination we use $i = 67^\circ$ (Section 1). Finally, we express $R_{\rm in}$ in dimensionless form, $r_{\rm in} \equiv R_{\rm in}/(GM/c^2)$ using $M = 10$ $M_\odot$ (Section 1). We have recently shown that the choice of M, i and D, which effectively sets the absolute scale for $r_{\rm in}$ and the luminosity, is quite unimportant for testing the stability of $r_{\rm in}$ (see Fig. 3 and text in Steiner et al. 2009a). (These values are crucial, however, when it comes to estimating the spin of the black hole.)

Using our adopted values of the source M, i, and D, our source model has four fit parameters: two for KERRBB2, $R_{\rm in}$ and the mass accretion rate $\dot{M}$, and two for SIMPL, the photon index Γ and $f_{\rm SC}$, which is the fraction of disk

photons that get re-directed via scattering into the power law. Our full model is TBABS(SIMPL⊗KERRBB2), where TBABS models the effects of photoelectric absorption; we fix its sole parameter: $N_{\rm H} = 4 \times 10^{20}{\rm cm}^{-2}$ (Page et al. 2003), using abundances from Wilms et al. (2000). For KERRBB2 we include limb darkening and returning radiation effects, set the torque at the inner boundary of the accretion disk to zero, and fix the normalization to unity. We use the efficient, up-scattering-only version of SIMPL, and in Section 4.5 we show that this choice is unimportant.

4.3.1 Data Selection

Our preliminary analysis of all the data showed that for many spectra the power-law index Γ was essentially unconstrained, even for the *BeppoSAX*, *EXOSAT*, *Ginga*, and *RXTE* missions, which have the requisite coverage to detect this component. This is because the source is relatively faint ($\lesssim 50$ mCrab) and its Compton power-law component is generally very weak, showing a median normalization $f_{\rm SC} \approx 0.3\%$. The extreme dominance of the thermal component in LMC X–3 makes it an ideal source for accretion-disk studies such as this.

Restricting our census to the 134 *RXTE* spectra for which the photon index is measured to a precision better than $\sigma_\Gamma = 0.5$, we find a strong clustering of values in the range $\Gamma \approx 2 - 2.6$. For our baseline model we fix $\Gamma = 2.35$ which matches the constant index derived from 22 deep *RXTE* pointings by Smith et al. (2007), and in Section 4.5 we show that our results depend very weakly on this choice for $2 \lesssim \Gamma \lesssim 3$.

Meanwhile, three missions, *ASCA*, *Swift* and *XMM*, have no sensitivity above

Table 4.1. Data and Instrument Summary

Instrument	$N_{\rm obs}$	$N_{\rm sel}$[a]	$f_{\rm TS}$[b]	$\Delta\Gamma_{\rm TS}$[b]	Ref.
RXTE (PCU-2)	712	391 (568)	1.097	0.010	···
Suzaku (XIS0)	2	2 (2)	0.98	-0.01	1,2
Swift (XRT)	1	1 (1)	1.01	-0.04	3[c]
XMM (MOS-1)	1	0 (1)	1.00	0.01	4,5,6
BeppoSAX (MECS)	23	2 (23)	0.95	0.00	7
ASCA (GIS-2)	2	2 (2)	0.97	-0.01	8,9
Ginga (LAC)	18	7 (11)	0.94	-0.02	10
EXOSAT (ME)	7	6 (6)	0.98	0.00	11

References. — (1) Serlemitsos et al. 2007; (2) http://heasarc.gsfc.nasa.gov/docs/suzaku/prop_tools/suzaku_td/suzaku_td.html; (3) Godet et al. 2009; (4) Guainazzi et al. 2009; (5) Stuhlinger et al. 2006; (6) private communication with Ignacio de la Calle; (7) Fiore et al. 1999; (8) Makishima et al. 1996; (9) Ebisawa 1996; (10) Turner et al. 1989; (11) Parmar & Smith 1985

[a] Number of selected observations. Parentheses indicate the selection numbers when high luminosities $L_{\rm D}/L_{\rm Edd} > 0.3$ are allowed (see Fig. 4.2).

[b] $f_{\rm TS}$ is the ratio of the Crab normalization to that of Toor & Seward and $\Delta\Gamma_{\rm TS}$ is the difference between photon indices.

[c]The *Swift* values are derived from a comparison between *RXTE* and *Swift* observations of 3C 273.

$E \approx$10 keV, and therefore only very loosely measure the power-law normalization parameter, $f_{\rm SC}$. At the same time, a self consistent and fruitful analysis of the thermal and Compton components requires that $f_{\rm SC}$ be sensibly constrained. Therefore, and because the power law is generally so weak, we impose an additional data-selection requirement, namely that for each fit $f_{\rm SC}$ falls within the lower 95% span of the *RXTE* rank-ordered values.

We further adopt a goodness-of-fit requirement, $\chi^2/\nu < 2$, and a lower limit on the Eddington-scaled disk luminosity, $L_{\rm D}/L_{\rm Edd} \equiv L_{\rm D}/L_{\rm Edd} > 0.05$. This latter criterion removes any hard state data in which the disk is likely truncated at $r > r_{\rm in}$ (e.g., Esin et al. 1997). Finally, in consonance with the thin-disk model employed, we select only data for which $L_{\rm D}/L_{\rm Edd} < 0.3$ (McClintock et al. 2006).

4.4 Results

The top panel of Figure 4.1 shows a 26-year record of the disk luminosity of LMC X–3, which is seen to vary by orders of magnitude. Two-thirds of the data meet our thin-disk selection criterion $L_{\rm D}/L_{\rm Edd} < 0.3$. In the lower panel, we show the time history of the inner disk radius $r_{\rm in}$ for just those data that meet all of our selection criteria (Section 4.3.1). The radius is constant over the 26 years of monitoring to within $\sim 2\%$ for *RXTE* alone and $\sim 4\%$ considering all missions.

Figure 4.2 explores the dependence of $r_{\rm in}$ on luminosity. In this figure we include the high-luminosity data ($L_{\rm D}/L_{\rm Edd} > 0.3$) that meet all of our other selection criteria (Section 4.3.1). For $L_{\rm D}/L_{\rm Edd} < 0.3$ there is a gentle, nonlinear rise of $r_{\rm in}$

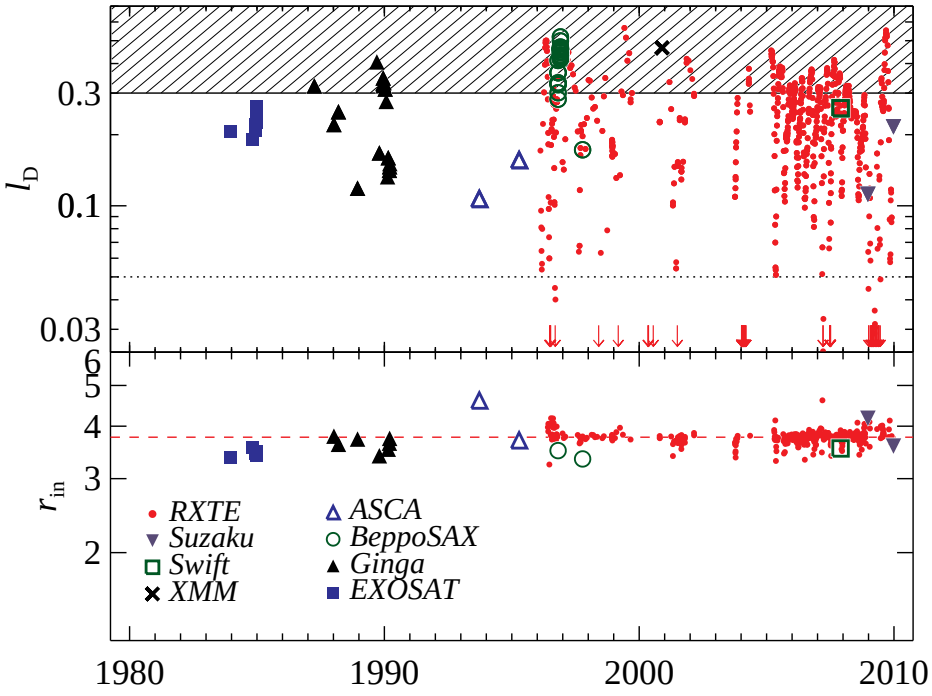

Figure 4.1.— **top:** Accretion-disk luminosity in Eddington-scaled units ($M = 10\,M_\odot$) versus time for all the data considered in this study (766 spectra). Red arrows show *RXTE* data which are off scale. Data in the unshaded region satisfy our thin-disk selection criterion ($H/R < 0.1$, which implies $L_D/L_{Edd} < 0.3$; McClintock et al. 2006). The dotted line indicates the lower luminosity threshold (5% L_{Edd}) adopted in Section 4.3.1. **bottom:** Values of the dimensionless inner disk radius r_{in} are shown for thin-disk data in the top panel that meet all of our selection criteria (411 spectra; see Section 4.3.1). Despite large variations in luminosity, r_{in} remains constant to within $\approx 4\%$ over time. The median value for the *RXTE* data alone ($r_{in} = 3.77$) is shown as a red dashed line.

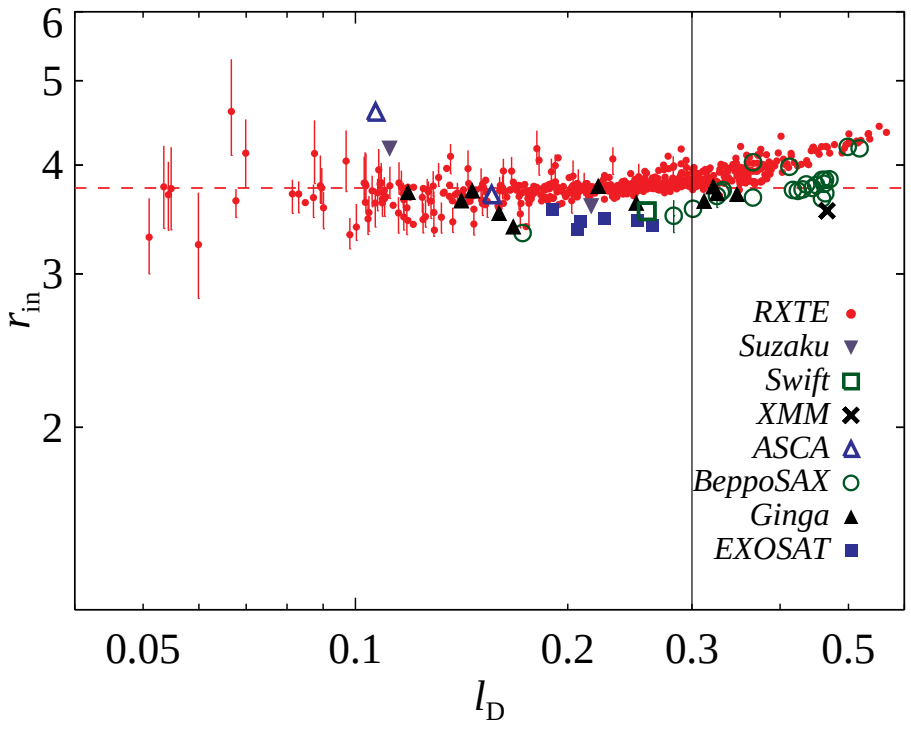

Figure 4.2.— The dimensionless inner-disk radius $r_{\rm in}$ versus luminosity for the filtered data (Section 4.3.1) and our baseline model. The vertical black line shows our adopted thin-disk upper limit, $L_{\rm D}/L_{\rm Edd} = 0.3$. As in Figure 4.1, the red-dashed line shows the *RXTE* average below this limit.

with luminosity. Especially visible in the *RXTE* data, this rise becomes prominent beyond $L_{\rm D}/L_{\rm Edd} \sim 0.25$, above which there is a $\sim 12\%$ increase in $r_{\rm in}$. No significant change in χ^2/ν is associated with the apparent increase of $r_{\rm in}$. We cannot say if this represents a real increase in $r_{\rm in}$ at high luminosities or is simply an artifact of using the thin-disk model, which is expected to be increasingly inaccurate at higher luminosities (Penna et al. 2010; Abramowicz et al. 2010) at which a transition may occur to an advective slim-disk accretion mode. Interestingly, however, despite this rapid rise, we note that the *RXTE* data appear tightly clustered along a well-defined curve. We approximate this dependence using a non-parametric curve-fit (LOWESS; Cleveland 1979) that allows us to detrend the data. We conclude that results from all eight missions, including the high-luminosity data, are in agreement with one another to within $\approx 6\%$.

4.5 Discussion

Figure 4.2 clearly demonstrates the limitations of the thin-disk model at high luminosities. We further illustrate this point in Figure 4.3 using LOWESS fits to the abundant *RXTE* data. We vary, one-at-a-time, the model components and parameters of our baseline model, grouping these trials into four separate "families." In order of increasing importance, these families are (1) column density $N_{\rm H}$, (2) power-law index Γ, (3) choice of power-law model, and (4) α. Figure 4.3 illustrates the changes introduced by adjusting each family of settings.

We highlight two conclusions from Figure 4.3: (1) Our results are relatively insensitive to all settings with the single exception of the choice of α-viscosity;

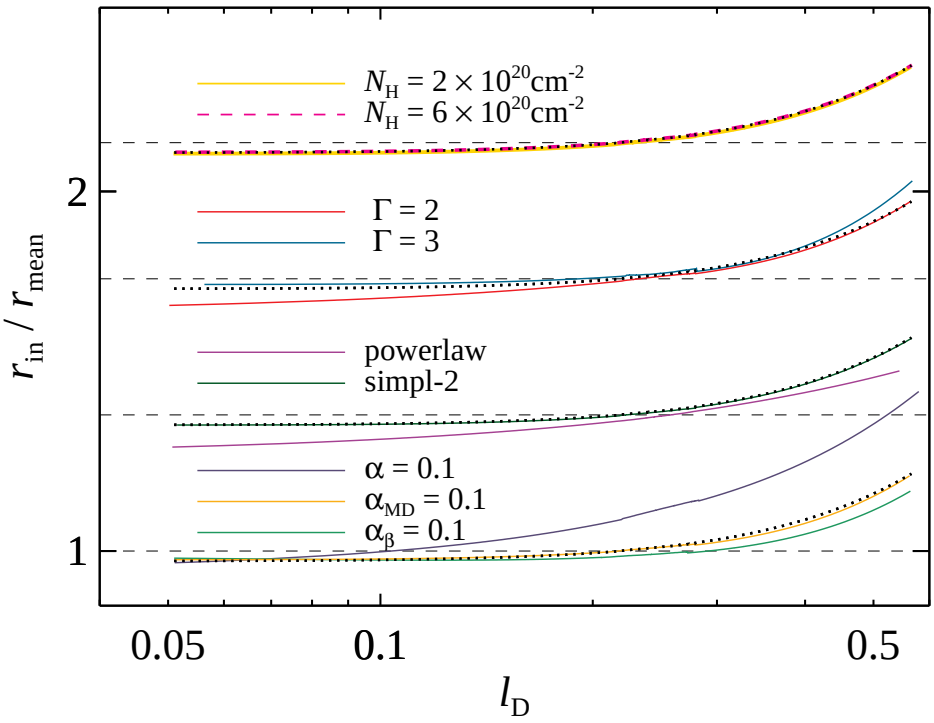

Figure 4.3.— Four families of models showing how our baseline results in Figure 4.2 are affected when a single model component or parameter is varied. The black dotted line drawn with each family of curves represents our fiducial model: $N_{\rm H} = 4 \times 10^{20}{\rm cm}^{-2}$; $\Gamma = 2.35$; SIMPL-1; and $\alpha = 0.01$. The horizontal dashed line for each family is set by the average value of $r_{\rm in}$ (see Figures 4.1 & 4.2), and each family is offset by 30% for clarity. Each curve represents a LOWESS curve fit to the *RXTE* data alone. Both axes are scaled logarithmically.

the value $\alpha = 0.1$ increases significantly the dependence of $r_{\rm in}$ on luminosity. (2) The positive correlation between $r_{\rm in}$ and luminosity is generally present for all families over the full range of luminosity, but it becomes prominent only above $L_{\rm D}/L_{\rm Edd} \approx 0.2 - 0.3$.

Inspecting the families of curves in Figure 3 from top to bottom, one concludes the following: As the first two families show, our results are insensitive to the choice of $N_{\rm H}$ and only modestly sensitive to the choice of Γ. In modeling the Compton tail component (third family), one sees that our results are essentially identical whether one uses our baseline up-scattering-only model SIMPL $\equiv$ SIMPL-1 or a a two-sided scattering model SIMPL-2 (Steiner et al. 2009a), while the results obtained using the standard power law model POWERLAW differ only modestly ($\lesssim 5\%$).

The fourth family considers the primary setting for BHSPEC, the viscosity parameter α, used to compute spectral hardening (Section 4.3). Here, we examine several distinct cases: our fiducial value, $\alpha = 0.01$ (dotted), the value $\alpha = 0.1$ (Section 4.3; dark blue), and alternative stress prescriptions $\alpha_{\rm MD} = 0.1$ (orange) and $\alpha_\beta = 0.1$ (green). The parameter α typically refers to viscosity in the disk which is proportional to the total pressure at the disk midplane. However, other choices exist such as "beta disk" and "mean disk" models in which α_β and $\alpha_{\rm MD}$ respectively describe viscosities which scale proportionally to the gas pressure or the geometric mean of gas and total pressures (Done & Davis 2008). Both latter options produce spectral hardening values quite similar to those obtained for $\alpha = 0.01$. In conclusion, only the second option, $\alpha = 0.1$, has an important effect on our results.

Our results indicate that the value of the inner disk radius $r_{\rm in}$ – and hence spin

– is stable over decades, as is expected given the minute effects of accretion torques on a BH over such a time scale. We also confirm that $r_{\rm in}$ is nearly independent of luminosity provided that the disk is geometrically thin. The stability of $r_{\rm in}$ over time (for $L_{\rm D}/L_{\rm Edd} < 0.3$) despite large fluctuations in the mass accretion rate provides strong evidence that $r_{\rm in}$ and $R_{\rm ISCO}$ are closely associated, as we tacitly assume in measuring BH spin (Section 4.1).

The inter-mission consistency of our results ($\approx 4\%$ below $L_{\rm D}/L_{\rm Edd} < 0.3$ and 6% overall) is very important for future X-ray continuum measurements of BH spin: For some transient BH sources (e.g., A0620–00 and GRS 1009–45) only one or a few spectra are available in the data archives. Our results for LMC X–3 show that, as long as the power-law component is reliably measured, even a single, suitable spectrum can deliver an estimate of the disk inner radius accurate to several percent, and thereby a reliable measurement of spin.

Chapter 5

Modeling the Jet Kinematics of the Black Hole Microquasar XTE J1550–564: A Constraint on Spin-Orbit Alignment

J. F. Steiner & J. E. McClintock *The Astrophysical Journal*, Vol. 745, pp. 136-144, 2012[1]

[1]Reproduced by permission of the AAS.

Abstract

Measurements of black hole spin made using the continuum-fitting method rely on the assumption that the inclination of the black hole's spin axis to our line of sight is the same as the orbital inclination angle i of the host binary system. The X-ray and radio jet data available for the microquasar XTE J1550–564 offer a rare opportunity to test this assumption. Following the work of others, we have modeled these data and thereby determined the inclination angle θ of the jet axis, which is presumed to be aligned with the black hole's spin axis. We find $\theta \approx 71^\circ$ and place an upper limit on the difference between the spin and orbital inclinations of $|\theta - i| < 12$ deg (90% confidence). Our measurement tests for misalignment along the line of sight while providing no constraint on the alignment in the plane of the sky. Our constraint on the misalignment angle supports the prediction that the spinning black hole in XTE J1550–564 has aligned itself with the orbital plane and provides support for the measurement of its spin via the continuum-fitting method. Our conclusions are based on a simple and reasonable model of a pair of symmetric jets propagating into a low density cavity whose western wall is $\approx 20\%$ closer to XTE J1550–564 than its eastern wall.

5.1 Introduction

Although it is thought that the Galaxy is host to tens of millions of stellar-mass black holes, only about 50 have been discovered (Özel et al. 2010). All of them are accretion-powered X-ray sources that are located in X-ray binary systems. Most

such systems, which are similar to our featured black hole binary XTE J1550–564, have short orbital periods ($P \sim 1$ d) and are comprised of a low-mass ($\lesssim 1$ $M_\odot$) donor star and a ~ 10 $M_\odot$ black hole. A stream of gas from the Roche-lobe-filling star feeds into the outer part of an accretion disk that encircles the black hole. On a time scale of weeks, viscous forces in the disk cause this gas to move radially inward to the center. Within a few hundred kilometers of the black hole, the optically-thick gas reaches a temperature of $\sim 10^7$ K and produces an X-ray luminosity that is near the Eddington limit ($L \sim 10^{39}$ erg s^{-1}). Accretion onto the black hole is not a steady process: A typical source is luminous for only about a year, and then it fades into a quiescent state for years or decades.

XTE J1550–564 (hereafter J1550) is a much-studied Galactic black-hole transient system that was discovered on 1998 September 6 using the All-Sky Monitor onboard the *Rossi X-ray Timing Explorer* (*RXTE*). Thereafter, it was observed almost daily during its entire 8-month outburst cycle using RXTE's pointed instruments (Sobczak et al. 2000a). Two weeks into outburst, the source abruptly rose fourfold in intensity and produced a brilliant 7-Crab flare. During this X-ray flare, J1550 was approximately at its Eddington limit for ≈ 1 day (Steiner et al. 2011). Four days later, radio observations made using the Australian Long Baseline Array (LBA) revealed relativistic ejecta moving both eastward and westward from J1550 (Hannikainen et al. 2009). The two components were observed to be separated by ~ 250 mas and moving at relative speed of $\mu_{\rm app} \approx 65$ mas/d, equivalent to an apparent separation velocity of ~ 1.7c. Nearly two years later, *Chandra* imaging observations revealed large-scale ($\gtrsim 20''$) relativistic jets undergoing deceleration (Corbel et al. 2002). This landmark discovery of a pair of ballistic X-ray jets was the

first detection of its kind for a Galactic source.

By modeling an extensive collection of optical and infrared data for J1550, Orosz et al. (2011) have determined the mass of the black hole primary, $M = 9.1 \pm 0.6$ M$_\odot$, the distance to the binary, $D = 4.38^{+0.58}_{-0.41}$ kpc, and the inclination of its orbital plane, $i = 74.^\circ7 \pm 3.^\circ8$. Assuming that the black hole's spin is aligned with the orbital angular momentum, Steiner et al. (2011) have measured the spin using the continuum-fitting method to be $a_* = 0.34^{+0.20}_{-0.28}$, where $a_* \equiv cJ_{\rm spin}/GM^2$ is the black hole's dimensionless spin parameter and $J_{\rm spin}$ its angular momentum. Steiner et al. also measured the spin using the independent Fe-line method and found $a_* = 0.55^{+0.10}_{-0.15}$; taken together, the two measurements imply $a_* \approx 0.5$. The continuum-fitting method relies on a model for the thermal emission from an accretion disk (Zhang et al. 1997), while the Fe-line method relies on a model of the relativistically broadened fluorescence features emitted by the disk (Fabian et al. 1989).

For a black-hole binary system like J1550, with a low-mass companion, the ratio of the orbital angular momentum to the spin angular momentum of the black hole is given by

$$J_{\rm orb}/J_{\rm spin} \approx 65\ a_*^{-1} \left(\frac{M}{10\ {\rm M}_\odot}\right)^{-4/3} \left(\frac{M_2}{{\rm M}_\odot}\right) \left(\frac{P}{1\ {\rm d}}\right)^{1/3}, \qquad (5.1)$$

where M_2 is the mass of the secondary star. For J1550, this ratio is ≈50, and thus it is reasonable to expect that, given a means of interaction, the spin of the black hole will eventually come into alignment with the orbital angular momentum. The time scale for this to occur is an important question for continuum-fitting spin measurements because in applying this method one generally must assume that the two vectors are aligned.

If there is an initial misalignment between the spin and the orbital angular momenta, then Lense-Thirring precession will cause the inner X-ray-emitting portion of the disk to line up with the spin of the black hole (Bardeen & Petterson 1975). At the same time, at very large scales, the disk will align itself with the orbital plane, and the transition between these regimes will manifest as a warp in the disk. When a misalignment is present, the black hole will be torqued into alignment by the accreting matter acting with a lever arm of order the size of the warp radius (e.g., Natarajan & Pringle 1998). Using a maximally conservative (minimum-torque) assumption, Fragos et al. (2010) concluded (based on a population synthesis study) that the spin axes of most black hole primaries will be tilted less than 10°. Fragos et al. assumed that the torque acts at the innermost stable circular orbit, $R_{\rm ISCO} < 6GM/c^2$ for $a_* > 0$, whereas the warp radius has been estimated to be located at $R_{\rm w} \approx 200GM/c^2$ (King et al. 2005; Lodato & Pringle 2006).

For a typical system, the time scale for accretion to torque the black hole into alignment has been estimated to be $t_{\rm align} \sim 10^6 - 10^8$ years (Martin et al. 2008; Maccarone 2002)[2]. Therefore, one expects alignment to occur early in the lifetime of an old-population transient system, such as J1550, and that most such systems will presently be well aligned.

It is obviously important to test this theoretical expectation. However, it has proved challenging to obtain a firm measurement of the degree of alignment for any black hole binary. Such a measurement requires a determination of the position

[2]Maccarone (2002) overestimated $t_{\rm align}$ as the result of a numerical error in his Eqn. 6, which implies a time scale that is 50 times longer than that implied by his Eqn. 1.

angle of the binary on the plane of the sky. While this may be possible in the future for J1550, we lack the requisite orbital astrometric data for the system and are therefore limited to testing for alignment along the line of sight. Measuring the orbital inclination angle of the binary is relatively simple and is routinely done by modeling optical data (e.g., Orosz et al. 2009). In contrast, it has proved difficult to obtain reliable estimates of the inclination of the inner disk.

Currently, the most direct way of determining the inner-disk inclination is by modeling jet ejecta, which are presumed to be aligned with the black hole's spin axis. For the case of symmetric ejecta, see the review by Mirabel & Rodríguez (1999). The jet ejecta that are relevant to this paper are pairs of discrete, detectable condensations of radio-emitting plasma, which we generally refer to in shorthand as "jets."

An alternative approach to measuring the inner-disk inclination is via the same Fe-line method that is used to measure black hole spin (Reynolds & Nowak 2003). However, existing models make simplifying assumptions concerning how the ionization state of the disk varies with radius. Given that there is a degeneracy between ionization and inclination in Fe-line/reflection models for stellar-mass black holes, these inclination estimates are subject to a systematic uncertainty of unknown magnitude. Meanwhile, prospects are good that more advanced reflection models will provide robust estimates of inclination.

Based on observations of radio jets, two confirmed black hole systems, GRO J1655–40 and SAX 1819–2525, are good candidates for hosting misaligned black holes. In the case of GRO J1655–40, using a kinematic model for the jets and

measurements of proper motion, Hjellming & Rupen (1995) reported a jet inclination angle of 85°. However, the authors give no error estimate for either the jet inclination angle or the proper motion. Furthermore, the reliability of the estimate for the jet inclination angle is called into question by the intrinsic and variable asymmetries that were observed for the opposing jets (Mirabel & Rodríguez 1999). Taking the 85° jet inclination angle at face value, one concludes that the jet axis and orbital vector are misaligned by $> 15°$ (Greene et al. 2001).

In the case of SAX J1819–2525, the evidence is less certain. There is only a single observation of extended radio emission (because the source faded promptly). By making the assumption that this emission was associated with a major X-ray outburst that occurred hours earlier, superluminal motion ($\beta_{\rm app} > 10c$) and a misalignment angle of $> 50°$ were inferred (Orosz et al. 2001; Hjellming et al. 2000). However, as Chaty et al. (2003) have argued, the jet may have been ejected a couple of weeks before the major outburst, in which case the Lorentz factor of the jet was modest and its inclination was consistent with the inclination of the binary. This is a reasonable possibility given that the source was observed to be active at optical wavelengths for several weeks before the X-ray outburst.

Compared to the jets in these two systems and those in other Galactic microquasars, the jet ejections observed for J1550 are remarkable. They were observable for years (rather than weeks or months), and therefore their physical separation from J1550 was observed to become exceptionally large. These are possibly the largest resolved jets observed for any black hole when considering the dimensionless distance between them, i.e., d/M (Hao & Zhang 2009, and see Heinz 2002). By this measure, the maximum 0.7 pc distance between the jet and J1550

corresponds to 7 Mpc for a supermassive black hole of 10^8 $M_\odot$.

In a previous study, Wang et al. (2003) modeled the evolution and light curve of J1550's ballistic jets using the same model we employ, namely, an expanding jet interacting with the interstellar medium (ISM). They modeled the data for the eastern jet, attributing the X-ray emission to a reverse shock, and found that the gas density around J1550 is unusually low. Later, their work was extended by Hao & Zhang (2009) to include the western jet. Both groups focused their attention on the properties of the environment around J1550; accordingly, they adopted nominal and fixed values for jet inclination (50° and 68°, respectively), initial Lorentz factor (3), and jet energy (3.6×10^{44} erg). Both groups found evidence for the existence of a low density cavity around J1550 (modeled in more detail by Hao & Zhang), and a possible east-west asymmetry in the ambient gas.

While we follow in the footsteps of Wang et al. and Hao & Zhang, our aim is different. We are focused on the question of the alignment of the inclination angle of the black hole's spin axis and the orbital inclination angle. Therefore, in distinction with the earlier work, we disregard the X-ray light-curve data, which are primarily useful in constraining the emission mechanisms or the electron density and magnetic fields in the jet. Rather, we concentrate on modeling the kinematics of the ballistic jets and deriving reliable values and error estimates for the kinematic parameters. The parameter of chief interest is the inclination of the black hole's spin axis.

5.2 Data

We use archival *Chandra X-ray Observatory* data for eight observations of J1550 that were obtained using the Advanced CCD Imaging Spectrometer (ACIS) between 2000 June and 2003 October. The exposure times range from $4 - 50$ ks. Pipeline processed level-2 event files[3] were used to produce images of the field of J1550. When detected, images of the eastern (approaching) jet yielded 16–40 counts and the western (receding) jet 100–400 counts; J1550 itself was always detected and yielded 60–3000 counts.

These same *Chandra* data were used by Hao & Zhang (2009) in their analysis of the X-ray jets. They relied on the absolute astrometric precision of *Chandra* in order to derive positions for each jet and thereby its offset from J1550. We have reduced the astrometric errors severalfold by directly measuring in each image the relative separations between J1550 and the jets.

In measuring the precise jet positions, which are given in Table 5.1, we smoothed each image using a $1''$ Gaussian kernel and then determined the centroid of each jet using the DAOphot FIND routine (Stetson 1987). This procedure was used to derive initial estimates for all the jet positions. Then, 1000 Poisson random realizations of each field were produced, and the centroid measurements were repeated. In most cases, the positions for a given jet were tightly clustered about a single value, and a separation and its error were derived from this distribution. However, for three observations of the eastern jet (Obs. X1, X3, and X6 in Table 5.1) the images are

[3]using CXC DS-7.6.10

particularly faint (possibly because the emission is extended), which resulted in a broad distribution of positions. In these cases, a Gaussian-weighted mean based on the jet position angle ϕ_j for each realization j was used to derive the separation between the jet and J1550. As a reference value, we used the average position angle for the jets $\phi_{\rm PA}$ along with its error $\sigma_{\rm PA}$, $\phi_{\rm PA} = 94\overset{\circ}{.}25 \pm 0\overset{\circ}{.}3$ (measured east of north). This value is consistent with those determined by Hannikainen et al. (2009) and Corbel et al. (2002) and was measured for a single frame generated by coaligning and coadding all of the X-ray images. The weights w_j were calculated according to $\log(w_j) = -\frac{1}{2}(\phi_j - \phi_{\rm PA})^2/\sigma^2_{\rm PA}$. Typically, the position errors for the eastern jet were several tenths of an arcsec, while for the brighter western jet they were $\lesssim 0.1''$.

In addition to the positions derived using the *Chandra* data, we include in our analysis two radio positions (Obs. R1 and R2 in Table 5.1). These measurements are taken from Corbel et al. (2002), who derived positions from observations obtained using the Australia Telescope Compact Array (ATCA) on 2000 June 1 and 2002 January 29. In the first observation, only the eastern jet is observed, whereas in the second, the eastern jet has faded and the western jet alone is present.

As a final constraint on our kinematic jet model, we require that the apparent separation speed of the jets at launch match the value measured using the LBA, 65.5 ± 13.2 mas/d Hannikainen et al. (2009). This speed and the jet positions are the sole inputs to our principal model in Section 5.5. However, in Section 5.6, we additionally consider radio intensity measurements given by Hannikainen et al. (2009). They report 2.29 GHz flux densities taken four and six days after the X-ray flare with intensity ratios of $S_{E1}/S_{W1} = 3.55$ and $S_{E2}/S_{W2} = 2.40$, respectively; we assume that these ratios are uncertain by 25%. We also adopt their measurements

of the radio spectral index, $\psi_1 = -0.43$ and $\psi_2 = -0.21$, taken from flux densities measured with the ACTA at 4.8 and 8.6 GHz. The spectral index measurements and corresponding LBA images, while not strictly simultaneous, were obtained within several hours of one another.

5.3 The Jet Model

The development of our kinematic jet model follows Hao & Zhang (2009) and Wang et al. (2003). The model we use has been designed to describe gamma-ray bursts, but it is applicable to a relativistic, adiabatically expanding jet. To begin, we consider a pair of symmetric jets, each launched with a kinetic energy E_0 and a Lorentz factor Γ_0. As the jets expand into their environments, they entrain material from the surrounding medium, dissipate their kinetic energy at the shock front and heat the ISM. We neglect radiative losses and assume that the jets are confined and evolve adiabatically. Following Wang et al. (2003), we assume that particles are accelerated uniformly and randomly at the shock front. Each such jet obeys the relation

$$E_0 = (\Gamma - 1)M_0c^2 + \sigma(\Gamma_{\rm sh}^2 - 1)m_{\rm sw}c^2, \tag{5.2}$$

where Γ is the instantaneous bulk Lorentz factor of the jet, M_0 is the mass of the jet ejecta, and $\Gamma_{\rm sh}$ is the Lorentz factor at the shock front. The mass of the entrained material, $m_{\rm sw}$, that has been swept up by the shock is approximately $m_{\rm sw} = \Theta^2 m_{\rm p} n \pi R^3/3$, where Θ and R are respectively the jet half opening angle and the distance the jet has traveled. The numerical factor σ varies from ≈ 0.35 for ultrarelativistic shocks to ≈ 0.73 in the nonrelativistic limit (Wang et al. 2003; Blandford & McKee 1976). Following Huang et al. (1999), we adopt a simple

Table 5.1. Relative Jet Positions

Obs.	$\Delta t'$[a](d)	Eastern Offset (arcsec)	Western Offset (arcsec)
R1	620.5	21.9±0.3[b]	···
X1	628.5	21.5±0.5	···
X2	701.4	22.7±0.2	···
X3	722.2	23.7±0.5	···
R2	1227.5	···	22.6±0.3[b]
X4	1268.8	28.5±0.2	22.78±0.05
X5	1368.5	···	23.19±0.07
X6	1466.0	29.6±0.6	23.44±0.10
X7	1591.3	···	23.76±0.10
X8	1859.6	···	24.4 ±0.2

[a]Time since the jets were launched: MJD - 51076.

[b]ACTA position from Corbel et al. (2002).

numerical scaling to interpolate between the two regimes: $\sigma = 0.73 - 0.38\beta$, ($\beta = \sqrt{1 - 1/\Gamma^2}$).

At the shock front, the jump condition relates the bulk Lorentz factor of the jet to that of the shocked gas (Blandford & McKee 1976):

$$\Gamma_{\rm sh}^2 = \frac{(\Gamma + 1)[\hat{\gamma}(\Gamma - 1) + 1]^2}{\hat{\gamma}(2 - \hat{\gamma})(\Gamma - 1) + 2}. \tag{5.3}$$

The adiabatic index $\hat{\gamma}$ varies between 4/3 and 5/3, which are respectively its ultrarelativistic and nonrelativistic limits. We interpolate between these regimes via $\hat{\gamma} = (4\Gamma + 1)/3\Gamma$ (Huang et al. 1999; Wang et al. 2003; Hao & Zhang 2009).

On the plane of the sky, the apparent proper motions of the approaching and receding jets, μ_a and μ_r, are given by

$$\mu_a = \frac{\beta\ c\ \sin\theta}{D(1 - \beta\ \cos\theta)}, \qquad \mu_r = \frac{\beta\ c\ \sin\theta}{D(1 + \beta\ \cos\theta)}. \tag{5.4}$$

As we show in Section 5.5, the simple model governed by Eqn. 5.2 fails to fit the observations. Motivated by the results of Hao & Zhang and Wang et al., we have generalized Eqn. 5.2 to allow for the jets to first propagate through a low density cavity before encountering and shocking against the ISM. In the east-west direction, we allow for the cavity to differ in size. We additionally consider the possibility of an intrinsic asymmetry in the jets. Eqn. 5.2 becomes:

$$\eta E_0 = (\Gamma - 1)\eta M_0 c^2 + \sigma(\Gamma_{\rm sh}^2 - 1) m_{\rm sw} c^2, \tag{5.5}$$

and the entrained mass is now

$$m_{\rm sw} = \frac{\Theta^2 m_{\rm p} n \pi}{3} \times \begin{cases} R^3, & R \leq \zeta R_{\rm cr}, \\ (\zeta R_{\rm cr})^3 + \delta[R^3 - (\zeta R_{\rm cr})^3], & R > \zeta R_{\rm cr}, \end{cases} \tag{5.6}$$

where $R_{\rm cr}$ and δ are respectively the radius of the cavity centered on J1550 and the density jump at the cavity boundary. The ratio of the western-to-eastern cavity dimensions is given by ζ. Similarly, $\eta \equiv \frac{(E_0/n\Theta^2)_{\rm west}}{(E_0/n\Theta^2)_{\rm east}}$ parameterizes the asymmetry of the jets. In application, the asymmetry parameters ζ and η are taken to be unity for the eastern jet and can vary for the western jet.

In order to obtain a model solution for a particular set of parameters, we evolve the energy equation as the jet expands (either Eqn. 5.2 or Eqn. 5.5) in 4-hour time-steps by sequentially solving for $\Gamma(t)$ in the rest frame of J1550. At each time step, we calculate the separation between each jet and the central source by integrating $\beta(t)$ and by calculating the projected angles α: $\alpha(t') = R(t)\sin\,\theta/D$. Here, $t' = t \mp R(t)\cos\,\theta/c$ is the observer's time, which takes into account the time delay between J1550's rest frame and that of the observer for whom the light-travel paths of the approaching and receding jets are respectively shortened and elongated.

Our model requires up to eight physical parameters: θ, Γ_0, D, $R_{\rm cr}$, δ, η, ζ, and lastly the "effective energy" $\tilde{E}$ which we now define. As alluded to above, a degeneracy exists in our model between jet energy, ambient gas density, and the jet opening angle. These three quantities appear as a single and inseparable term in the kinematic equations, $E_0/n\Theta^2$. To make physical sense of this combined quantity, we assume that the density of the ISM is a standard $n_{\rm ISM} = 1$ cm^{-3}, so that $n = 1/\delta$ cm^{-3}, and adopt $\Theta = 1^\circ$ (Kaaret et al. 2003). Predicated upon our assumed values for $n_{\rm ISM}$ and Θ, the jet energy E_0 is then $E_0 = \tilde{E}$.

Finally, we go beyond our principal, kinematic model to consider the ratio of the radio intensities of the two jets. We consider the simplest case of the ejection of a

pair of identical and unimpeded condensations. When measured at equal separation from the black hole, one has

$$\frac{S_a}{S_r} = \left(\frac{1+\beta\,\cos\,\theta}{1-\beta\,\cos\,\theta}\right)^{3-\psi}, \tag{5.7}$$

where ψ is the spectral index and the subscripts a and r refer to the approaching and receding jets, which are taken to be discrete ejecta (Mirabel & Rodríguez 1999). Because the jets are observed at unequal distances from the black hole, we must adopt a model of how jet intensity varies with time; we assume a simple power-law dependence. Then, allowing for our case of intrinsically asymmetric jets, Eqn. 5.7 becomes

$$\frac{S_a}{S_r} = \left[\frac{\Gamma_r(1+\beta_r\,\cos\,\theta)}{\Gamma_a(1-\beta_a\,\cos\,\theta)}\right]^{3-\psi-\Delta} \eta^q, \tag{5.8}$$

where Δ is a fit parameter, which for positive values describes a decay in brightness with time. The effect of jet asymmetry on the radio emission is captured by q, which can range from -1 to 1.5 depending on the source of asymmetry: E_0 ($q = -1$), n ($q = 0$), or Θ ($q \in [1, 1.5]$).

5.4 Markov Chain Monte Carlo

Markov Chain Monte Carlo (MCMC) is a powerful statistical technique by which random samples are drawn from a posterior distribution of arbitrary form. In our case, the posterior distribution is the probability of our model parameters, given the data. MCMC algorithms perform a "guided walk" of transitions through parameter space such that, after an initial burn-in phase, the chain directly reproduces the likelihood surface for the model. MCMC has several advantages over traditional

gridded-search algorithms when the number of parameters is large. For example, the search time with MCMC scales approximately linearly with the number of parameters rather than exponentially (Martínez et al. 2009). Furthermore, the ergodic property of the Markov Chain guarantees (asymptotically) that the chain will fully explore parameter space and reach the optimum global solution.

Transitions in the chain are effected via a "jump" distribution[4] $J(x^*|x_n)$ (e.g., a multivariate Gaussian) that defines a probability of selecting a candidate transition to a new state x^* given the current state x_n. The transition probability from x_n to x^* is governed by the Metropolis-Hastings algorithm (Hastings 1970) and is determined by the ratio r of probability densities

$$r = \frac{p(x^*|y)J(x_n|x^*)}{p(x_n|y)J(x^*|x_n)}, \tag{5.9}$$

where y refers to the data, and $p(a|b)$ should be read in the usual way as the probability of a given b. The term $p(x^*|y)/p(x_n|y)$ in the equation above gives the likelihood ratio of the two states, while the remaining term corrects for bias introduced by the jump-distribution density at each state. The state of the next link in the chain, x_{n+1}, is then chosen according to

$$x_{n+1} = \begin{cases} x^*, & \text{with probability } \min[r, 1], \\ x_n, & \text{otherwise.} \end{cases} \tag{5.10}$$

The likelihood ratio appearing in Eqn. 5.9 is calculated by evaluating the χ^2 for each state while taking into account the prior $\wp$ on all of the model parameters. In this

[4]We implement a particular class of the algorithm known as random-walk MCMC. In this approach, a sequence of transitions from the current parameter values are proposed and are then incrementally accepted or rejected.

case, the priors are introduced independently so that $\wp \equiv \prod_{k=1}^{\mathrm{N}} \wp_k$, where N is the number of parameters and $\wp_k$ gives the prior for parameter k. Omitting additive constants, the log-likelihood for state x is

$$\log\left(p(x|y)\right) = -\frac{1}{2}\left[\chi^2(x) - 2\,\log\left(\wp(x)\right)\right]. \tag{5.11}$$

5.4.1 MCMC in Practice

As Eqn. 5.11 makes apparent, the prior acts as a penalty to χ^2, and for the special case that a prior is "flat" (i.e., independent of x), one recovers the usual least-squares formula. It is also worth noting that because the prior only enters into the MCMC chain generation as a ratio (Eqn. 5.9) the scaling of the prior is arbitrary. We introduce a new term for this penalized χ^2, namely $\chi^2_\wp$, such that

$$\chi^2_\wp(x) \equiv \chi^2(x) - 2\,\log\left(\wp(x)\right). \tag{5.12}$$

Unless stated otherwise, we choose to normalize the prior so that the penalty term ($2\,\log[\wp(x)]$) is zero at the best fit, i.e., at the minimum value of $\chi^2_\wp$.

We adopt an asymmetric Gaussian prior on the distance to match its measurement in previous work (see Section 5.1; Orosz et al. 2011). For the asymmetry parameters, we adopt a log-flat prior on the difference from unity, i.e., $\wp_\eta \propto \min[1/\eta, \eta]$ (and likewise for $\wp_\zeta$). As an example and stated differently, we consider a term implying a 10-fold asymmetry to be *a priori* one tenth as likely as one that is symmetric. We adopt flat priors on θ and R_{cr} and flat priors on the log-values of scale parameters (i.e., the jet energy, Γ_0 and δ). The priors and

parameter ranges[5] are discussed further and illustrated in Section 5.5.

In order to initialize the chain and the jump distribution, we make starting guesses for the model parameters and step sizes. These initial values are improved upon by running a sequence of "training" iterations. The training phase incrementally improves the jump function until its shape is a close approximation to the posterior covariance matrix, thereby greatly increasing the MCMC efficiency. The sequence becomes increasingly tuned to the likelihood surface, simultaneously refining Σ (the covariance estimate)[6] and optimizing the solution.

The training phase continued for a minimum of 15 iterations, each of which generated a trial chain with 2000 elements. Training terminated either after 25 cycles were completed or when the chain attained an acceptance fraction between 24% and 37%[7].

Upon completing the training cycle, 8 chains were generated and run in parallel using the trained jump function, each to a length of 110 thousand elements. Seven of the starting positions were chosen by sampling using a dispersed covariance $\Sigma' = 10\ \Sigma$ about the final training position, and the eighth was started directly

[5]While it is optimal to use an unbounded parameter space in performing MCMC sampling, it is also sensible to set physically meaningful constraints on the parameters (e.g., $\Gamma_0 > 1$). To achieve both objectives, we have transformed each parameter using a logit function to map a parameter z from its range $[z_{\rm min}, z_{\rm max}]$ onto an infinite scale: $\mathrm{logit}(t) \equiv z_{\rm min} + (z_{\rm max} - z_{\rm min})/(1 + e^{-t})$ for $-\infty < t < \infty$.

[6]Σ is calculated from the chain positions and is used to define the jump function for each sequence. The jump function is taken to be a $t-$distribution with 4 degrees of freedom that is symmetric about the present position.

[7]The target acceptance fraction was set at $\approx 32\%$. The optimal value ranges from $\approx 23\%$ for an infinite-dimensional problem to $\approx 45\%$ for a univariate problem (Gelman et al. 1996). Each run produced an acceptance fraction of at least 20%

from the end location reached by the training sequence. The initial 10,000 elements of each chain were rejected as the "burn-in" phase during which the chains relax toward a stationary distribution. Our final results are based on a total of 8×10^5 MCMC samples. Convergence of the MCMC run is determined using the criterion of Gelman & Rubin (1992), $\hat{R}$. The closeness of this criterion to unity is the measure of convergence.

In Figure 5.1, we plot a trace of our parallel runs over time for inclination in our adopted model (see Section 5.5). In the bottom panel, we show the Gelman & Rubin convergence diagnostic of the chain over time. Typically, a chain is considered converged if $\hat{R} \leq 1.1$, or 1.2 (see, e.g., Verde et al. 2003)[8]. For θ, our parameter of interest, we obtain $\hat{R} < 1.01$.

5.5 Results

In this section we consider three symmetric-jet models, including our adopted model. For these models, and for the additional models discussed in the following section, we assume that the jets were launched at the time of J1550's giant X-ray flare (Section 5.1).

[8]Larger values of $\hat{R}$ suggest that either the parameter space is insufficiently sampled or that the chains are not fully evolved.

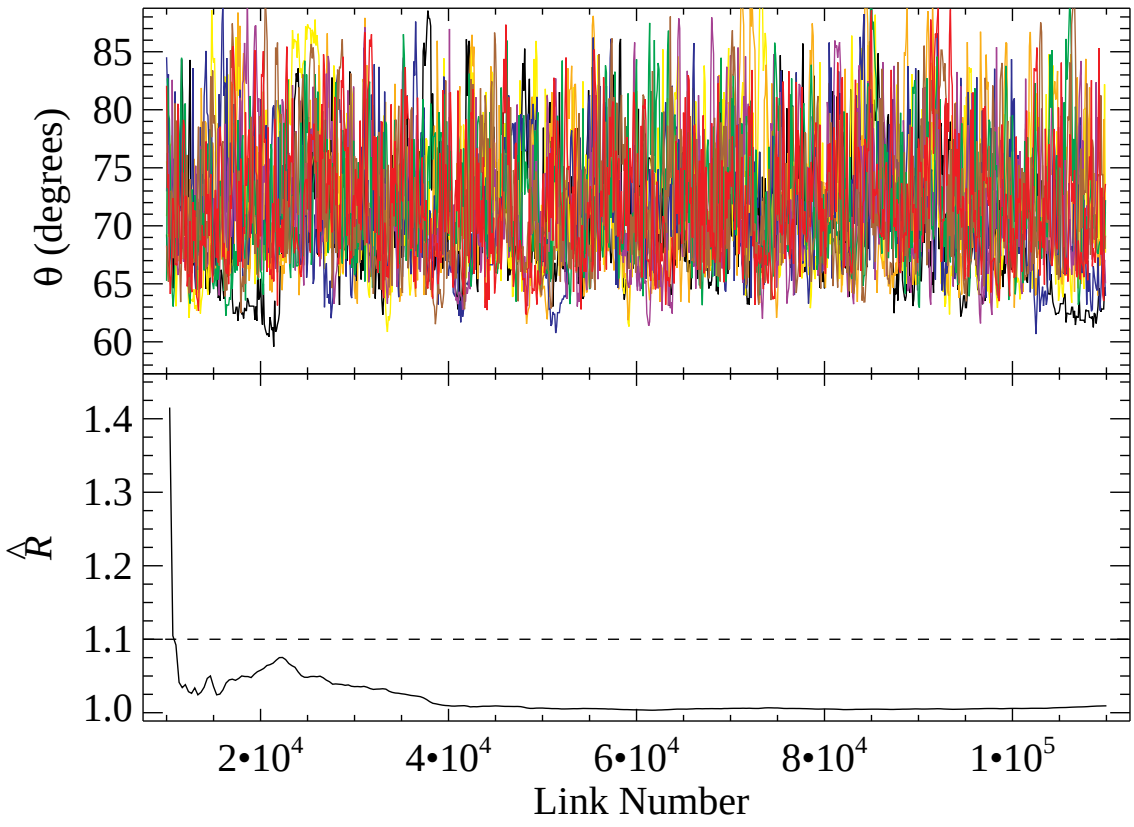

Figure 5.1.— *top*: The trace of θ for Model AC of Section 5.5. Eight parallel chains are used; for each, the initial 10^4 elements are generated during the burn-in phase and discarded from the analysis. *bottom*: The convergence of the chain over time. The chains reach convergence quickly, which is indicative of efficient sampling.

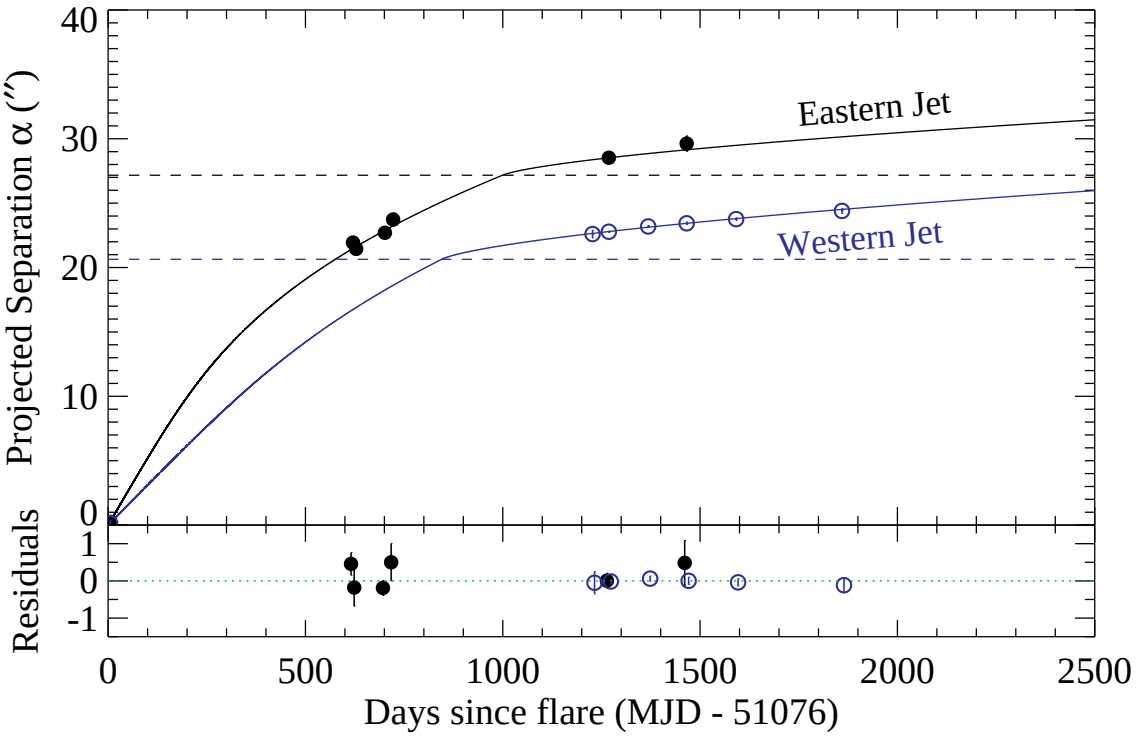

Figure 5.2.— The best-fitting model and fit residuals for the eastern jet (filled circles) and the western jet (open circles). The cavity locations are marked by dashed horizontal lines, which indicate that the western wall (for the receding jet) is closer to the black hole than the eastern wall. For clarity, residuals for the coincidentally detected eastern and western jets are shown slightly offset in time. In the top panel, the error bars are smaller than the symbols.

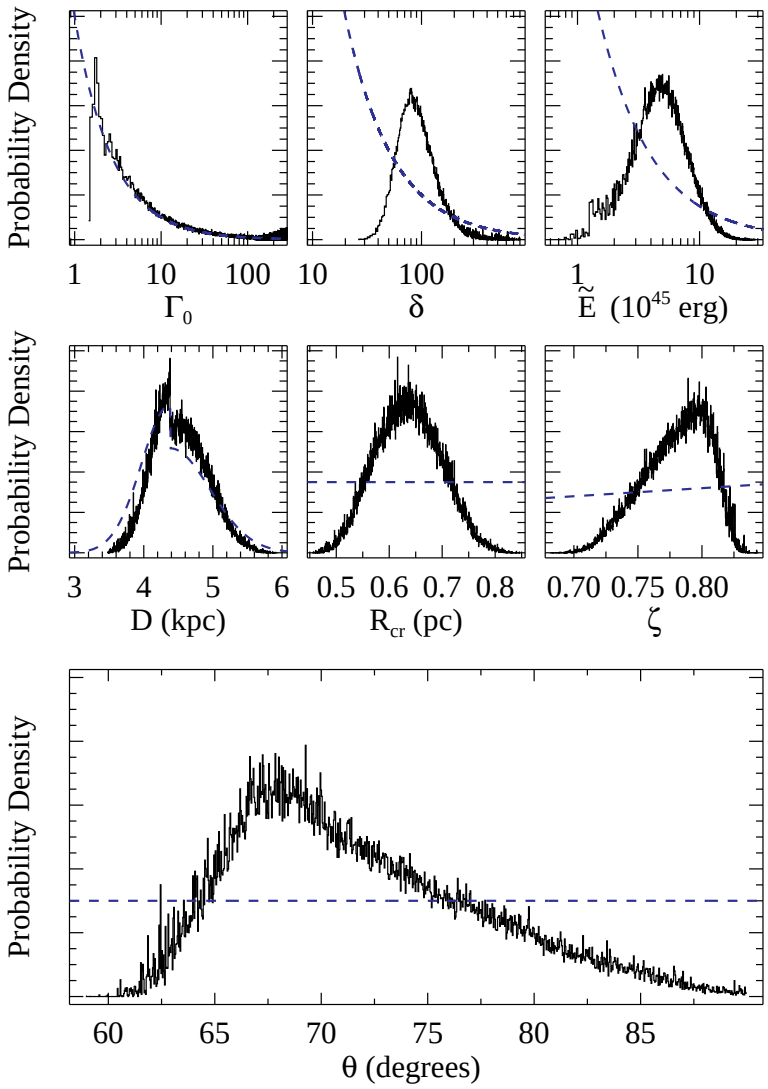

Figure 5.3.— MCMC results for Model AC. Probability densities are shown for each parameter on an arbitrary scale and have been obtained by marginalizing over all other parameters. An overlay for each prior shape is drawn as a dashed line. Note that the only two parameters which closely track the prior function are the system distance and Γ_0 (at high values only). Otherwise, the prior contributes minimally to the parameter distribution.

5.5.1 Two Preliminary Models

We first consider and rule out two simple models. For the simpler of these, which we refer to as Model S1, the jets are symmetric and propagate through a uniform medium (Eqn. 5.2; i.e., $\eta = \zeta = \delta = 1$ and $R_{\rm cr} = 0$). The strong deceleration of the jets at late times is not accommodated by this model, and the best fit achieved is unacceptable, $\chi^2_\wp/\nu = 68$. For Model S2, we introduce a symmetric cavity centered on J1550 with δ and $R_{\rm cr}$ as free fit parameters. The fit is significantly improved, $\chi^2_\wp/\nu = 42$, but it is still far from acceptable. The results for both models are given in Table 5.2.

5.5.2 Our Adopted Model

We now consider our primary model – an extension of Model S2 that allows the source to be positioned off-center in the cavity. This asymmetric cavity model (Model AC) is obtained by freeing the fit parameter ζ (while leaving η fixed at unity; see Eqn. 5.5). As illustrated in Figure 5.2, for a modest (22%) degree of asymmetry, this model produces a successful fit to the data with $\chi^2_\wp/\nu = 1.44$. Results are given in Table 5.2 and marginal distributions from the MCMC run are shown for each parameter in Figure 5.3.

The eastern and western cavity walls are located respectively at 0.6 pc and 0.5 pc from the black hole and the density contrast at the boundary of the cavity is ~ 100. The gas density within the cavity is much lower than that of the ISM. This must be the case in order for the jets to have passed through without sweeping up enough mass to halt their expansion. Motion within the cavity lasted for $\approx$1.5 years

(in the frame of J1550), until the receding western jet impacted the dense ISM at its cavity wall and abruptly began decelerating in advance of its eastern counterpart (see Fig. 5.2).

The total energy for both jets is an impressive $E_{\rm tot} \approx 10^{46}$ erg $\frac{n_{\rm ISM}}{1{\rm cm}^{-3}} \left(\frac{\Theta}{1 \deg}\right)^2$. At launch, the Lorentz factor of the jets is constrained to be $\Gamma_0 > 1.6$ (99.7% confidence). However, the data provide no upper limit on Γ, as implied by Figure 5.3, which shows that for large values of Γ the distribution closely tracks the prior. Likewise, the data only weakly constrain J1550's distance. However, the remaining five parameters are well determined by the data and are quite independent of their priors (Fig. 5.3). For the key parameter, the jet inclination angle, we obtain $\theta \approx 71^\circ$ ($64^\circ < \theta < 83^\circ$ at 90% confidence) and find only moderate correlations with the other fit parameters. The strongest of these correlations are with ζ and with $R_{\rm cr}$, which are illustrated in Figure 5.4.

5.5.3 Constraining Spin-Orbit Alignment

We now use Model AC and the results of our MCMC analysis to examine the relationship between the spin axis of the black hole (the same as that of the jet; see Section 5.1), and the orbital angular momentum vector. We assume that the inclination of the orbital plane i is Gaussian distributed: $i = 74\overset{\circ}{.}7 \pm 3\overset{\circ}{.}8$ (Orosz et al. 2011).

Our constraints on the locations of both axes are illustrated in Figure 5.5, which was derived using one million Monte-Carlo draws to represent each axis. This figure shows how readily our results are able to falsify the alignment hypothesis,

even though we lack a measurement of the position angle of the orbital plane. Specifically, (1) over 80% of the sky, we are able to rule out the possibility that the spin and orbital axes are aligned[9]; and (2) the probability by random chance that the inclination angles agree so closely (see Fig. 5.6) is less than 10%.

Because the continuum-fitting method depends only on the inclination angle (and not the position angle), and because the difference between the inclination θ of the spin/jet axis and the inclination i of the orbital plane is of critical importance in measuring the spin of J1550, we now use Model AC to determine $\theta - i$. Our results are shown in Figure 5.6 where it is obvious that there is no evidence for any misalignment along the line of sight. That is, our results are consistent with $\theta = i$. We place upper limits on the absolute difference between orbital and spin inclinations of 8° and 12° at the 68% and 90% levels of confidence, respectively.

Given the $< 10\%$ a priori chance that the inclination angles agree as closely as measured, our results provide support for the hypothesis that the two axes are aligned. However, without knowledge of the position angle of the binary axis (which can lie anywhere along the grey band in Fig. 5.5), we cannot conclude whether they are, in fact, aligned.

5.6 Radio Intensities and Asymmetric-Jet Models

We now consider the radio intensity measurements discussed in Section 5.2 in order (1) to identify any intrinsic asymmetry in the jets and (2) to check the consistency

[9]at 90% confidence

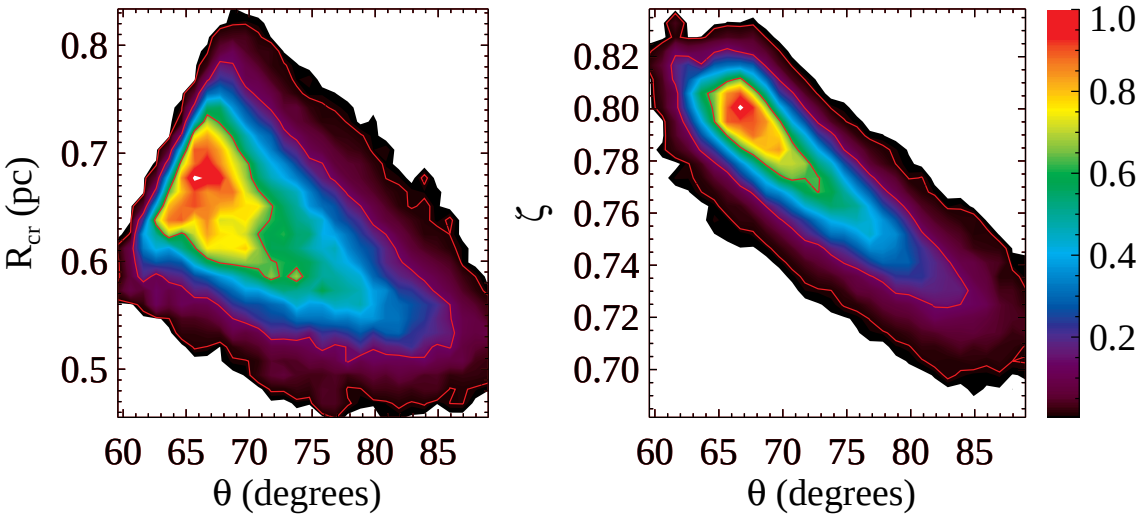

Figure 5.4.— Shown for Model AC are the MCMC density contours for the two parameters that correlate most strongly with inclination: cavity size $R_{\rm cr}$ and cavity asymmetry parameter ζ. The densities are calculated by marginalizing over all unshown parameters. Red contours mark the 68%, 95%, and 99.7% confidence regions about the most likely value, which is normalized to a density of unity. The central value of θ changes from 70° to 80° as $R_{\rm cr}$ varies from 0.65 pc to 0.58 pc, and as ζ decreases from 0.78 to 0.74.

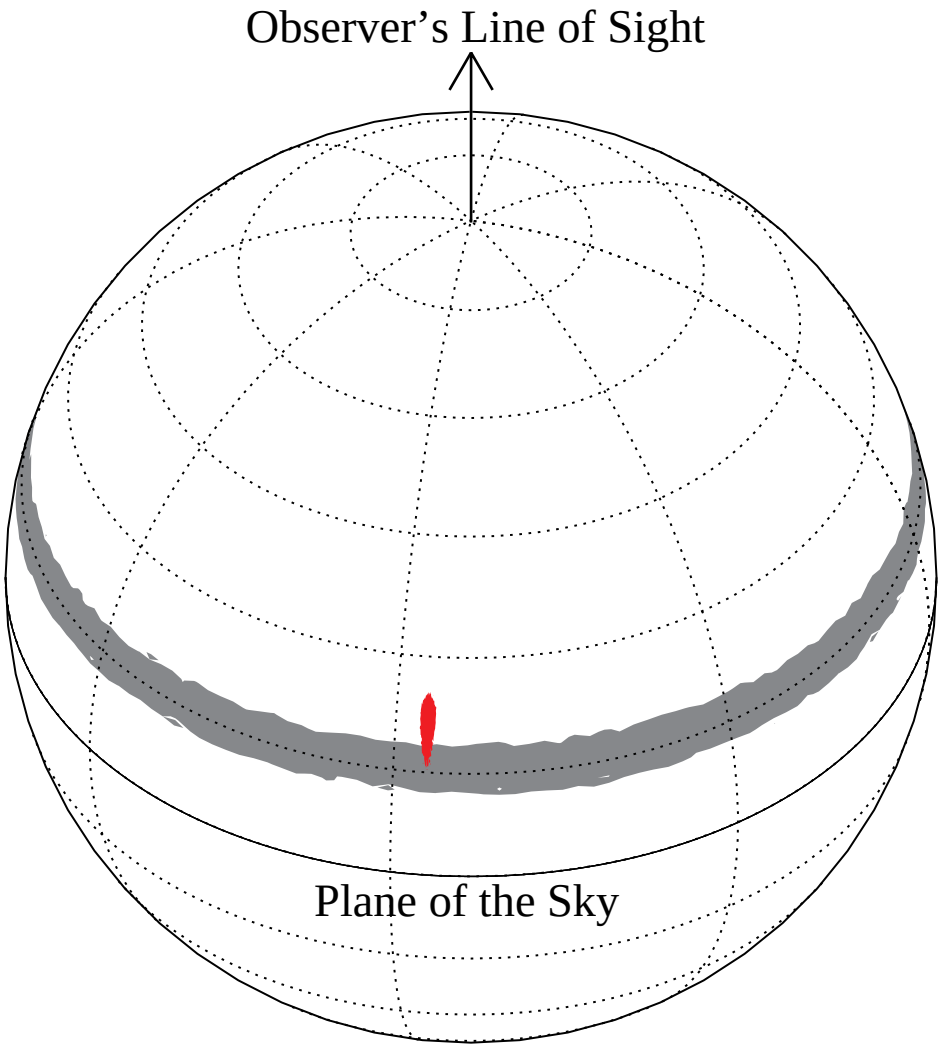

Figure 5.5.— The celestial sphere centered about J1550 with the observer situated along the pole. The angular momentum of the orbital plane is constrained to lie along the grey band (drawn with 1σ width), and the spin angular momentum axis derived from the jets is overlaid in red (1σ about the most likely value). The position angle is completely unbounded for the orbital angular momentum, whereas the jets provide a tight constraint on the position angle of the black hole's spin axis (Section 5.2). In fact, the uncertainty in the position angle of the jets is so small (± 0.3 deg) that for purposes of illustration it has been tripled to make it visible in this figure.

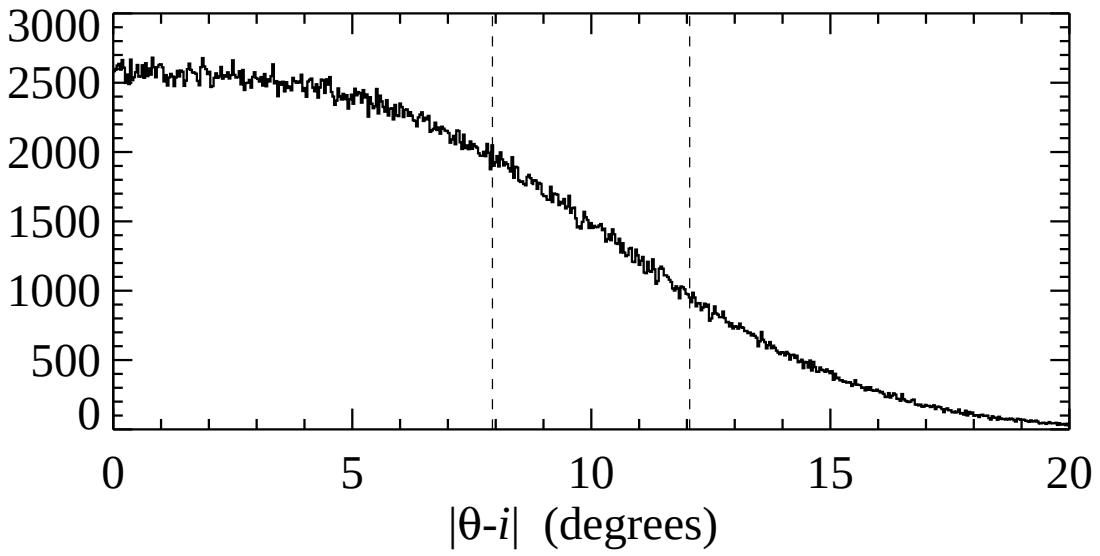

Figure 5.6.— The difference in orbital and jet inclination angles derived from the MCMC run of Model AC. The results show no sign of a misalignment along the line of sight; 68% and 90% upper limits on the difference between inclinations are 8° and 12°, respectively.

Table 5.2. Kinematic Model Settings and Fit Results

Parameter	Range	Prior Shape[a]	Model S1	Model S2	Model AC
θ (degrees)	$0 - 89.99$	F	53.9 ± 0.7	58.16 ± 1.7	$70.8^{+7.3}_{-4.5}$
Γ_0	$1 - 1000$	LF	210^{+390}_{-160}	50^{+320}_{-43}	36^{+300}_{-32}
$\tilde{E}$[b](10^{45} erg)	$10^{-10} - 10^{10}$	LF	$91.8^{+9.6}_{-6.7}$	74^{+18}_{-14}	$5.9^{+3.6}_{-2.3}$
D (kpc)	$3 - 7$[c]	N($4.38^{+0.58}_{-0.41}$)	3.07 ± 0.06	$4.30^{+0.29}_{-0.23}$	$4.48^{+0.43}_{-0.34}$
$R_{\rm cr}$ (pc)	$0 - 5$	LF	$\cdots$	0.46 ± 0.03	0.63 ± 0.06
δ	$0.1 - 10^4$	LF	$\cdots$	940^{+4900}_{-790}	104^{+70}_{-34}
ζ	$10^{-2} - 10^2$	LF (max[ζ,ζ^{-1}])	$\cdots$	$\cdots$	0.78 ± 0.03
$\min(\chi^2_{\wp}/\nu)$	$\cdots$	$\cdots$	67.93 (543.4/8)	41.59 (249.6/6)	1.44 (7.21/5)
$\min(\chi^2/\nu)$	$\cdots$	$\cdots$	67.61	40.94	1.22

Note. — The values quoted are the median parameter and symmetric 68% confidence interval (1σ equivalent) derived from the MCMC run (as opposed to the single best-fit values).

[a]F is flat, LF is log-flat, and N is a normal distribution.

[b]Assumes $n_{\rm ISM} = 1$ cm^{-3} and $\Theta = 1^\circ$.

[c]The lower bound on distance is taken from Hannikainen et al. (2009) and the upper bound is derived using $D \leq \frac{c}{\sqrt{\mu_a \mu_r}}$ (Mirabel & Rodríguez 1999).

of our kinematic model. In doing this, we are motivated by observations of the microquasar GRO J1655–40, which in 1994 displayed multiple ejection events, each of which expanded and decayed on a time scale of a few days. The approaching and receding jets were found to be intrinsically asymmetric; additionally, the sense of the asymmetry changed from event to event (Hjellming & Rupen 1995; Mirabel & Rodríguez 1999).

Before introducing intrinsic jet asymmetry into the model, we first proceed by extending Model AC to create Model RAC. This latter model retains the traits of Model AC but now incorporates Eqn. 5.8 and uses the additional free parameter Δ to model the radio data. The data set for Model RAC is likewise extended and includes its two radio intensity measurements (Section 5.2; Hannikainen et al. 2009). Re-fitting the data using Model RAC and comparing with the results obtained for Model AC, we find a slight (2°) increase in the jet angle and similar small changes in the other parameters (Table 5.3). The fit is good, $\chi^2_\wp/\nu = 1.44$, and Δ, the decay rate of the jet emission, is positive and in the range $\approx 1 - 5$.

We now examine intrinsic jet asymmetry, and introduce Model RAJ, a model that considers both kinematics and radio emission. In this case, the cavity is presumed to be symmetric, while the energy term ($E_0/n\Theta^2$) is allowed to vary between the eastern and western jets. Specifically, we set $\zeta = 1$, free η, and introduce the parameter q, which characterizes the type of asymmetry in the jets (Eqn. 5.8). The fit results for Models RAC and RAJ are shown in Table 5.3. Model RAJ returns a significantly larger jet inclination angle than Model RAC, $\theta \approx 82°$, and it implies a large difference between the eastern and western jets, $\eta^{-1} \sim 15$. Because $q \approx 0$, for this model the gross asymmetry can be attributed to an east-west difference in the

gas density (rather than an asymmetry in the energies or opening angles of the jets; see Section 5.3).

To assess the performance of Model RAC relative to Model RAJ, we exploit the similarities in the way these models are structured. In particular, their respective priors have identical form. Therefore, because we attribute equal likelihood to either type of asymmetry, we can apply the penalty normalization from Model RAC to Model RAJ. This yields the goodness-of-fit results shown in Table 5.3. Model RAJ is effectively ruled out: $\min(\chi^2_{\wp,\mathrm{RAJ}})-\min(\chi^2_{\wp,\mathrm{RAC}}) = 8.2$.

We now test the strength of this result by considering a kinematic-only variant of this asymmetric-jet model, Model AJ, which ignores the radio intensity data. Model AJ has the virtue that it can be directly compared with our primary model, Model AC, because both models have the same number of parameters (seven) and their priors are identically structured. As in the comparison above, we apply the penalty normalization of Model AC (Section 5.5) to Model AJ. The fit results for the two models are given respectively in Tables 5.2 and 5.3. Based on the substantial difference in $\chi^2_\wp$, $\min(\chi^2_{\wp,\mathrm{AJ}})-\min(\chi^2_{\wp,\mathrm{AC}}) = 7.5$, and the even larger difference obtained when the radio-intensity data are included, we conclude that the asymmetric cavity model is favored over the asymmetric jet model at the 99% level of confidence.

Unlike the manifestly asymmetric jets of GRO J1655–40, the available evidence indicates that the jets of J1550 are likely intrinsically symmetric: Model AC is favored over Model AJ, and Model RAJ implies an implausibly large (factor of 15) difference in the density of the ISM from west to east.

In comparison with Model AJ or RAJ, our adopted Model AC gives a reasonable and satisfying description of J1550 as a system comprised of intrinsically symmetric jets propagating through an evacuated cavity with eastern and western walls located out at 0.6 pc and 0.5 pc, respectively.

5.7 Discussion

If we assume that the jets were produced continuously over the day-long Eddington-limited X-ray flare (Steiner et al. 2011), then the nominal total jet energy of $\approx 10^{46}$ erg implies that a significant fraction of the mass accreted onto J1550 during the flare was directly used to fuel the jets. Roughly, the initial mass in the jets was then $\sim 10^{24}$ g and the matter was accelerated to $\Gamma_0 \sim 10$.

We note that the moderate asymmetry we find (with the western cavity $\approx 20\%$ smaller in radius than the eastern one) is opposite in sense from the asymmetry determined by Hao & Zhang (2009). We attribute this difference to several factors: Hao & Zhang simply adopted reasonable, ad-hoc values for several key parameters (θ, $\tilde{E}$, and Γ_0), and they found a high degree of asymmetry with $\eta^{-1} \approx 30$ and $\zeta = 1.4$. (We note that this particular pair of values of η and ζ allowed a reasonable fit to be achieved to their data set.) By improving the quality and quantity of the astrometric data, we were able to determine that just one asymmetry parameter is required to explain the data, and that the resultant asymmetry is less extreme.

Based on results obtained for the sub-pc scale ($\lesssim 0.1$ pc) jets of GRS 1915+105 and GRO J1655–40, Heinz (2002) has proposed that black hole microquasars

Table 5.3. Additional Model Results

Parameter	Model AJ	Model RAC	Model RAJ
θ (degrees)	$86.2^{+2.4}_{-3.1}$	$72.8^{+7.4}_{-5.4}$	$81.9^{+5.1}_{-6.8}$
Γ_0	22^{+270}_{-19}	37^{+390}_{-33}	$1.41^{+0.33}_{-0.14}$
$\tilde{E}^{\rm a}(10^{45}$ erg)	213^{+83}_{-65}	$6.1^{+3.8}_{-2.3}$	80^{+30}_{-34}
D (kpc)	4.83 ± 0.36	$4.49^{+0.43}_{-0.35}$	$3.57^{+0.50}_{-0.44}$
$R_{\rm cr}$ (pc)	0.46 ± 0.05	0.63 ± 0.06	$0.35^{+0.04}_{-0.05}$
δ	510^{+1700}_{-410}	98^{+57}_{-30}	740^{+3300}_{-590}
ζ	···	0.78 ± 0.03	···
$\eta^{\rm b}$	0.065 ± 0.014	···	$0.068^{+0.016}_{-0.013}$
$\Delta^{\rm c}$	···	$1.9^{+3.2}_{-1.1}$	$1.8^{+5.3}_{-6.5}$
$q^{\rm d}$	···	···	$-0.28^{+0.52}_{-0.35}$
$\min(\chi^2_\wp/\nu)$	2.95 (14.74/5)$^{\rm c}$	1.44 (8.63/6)	3.36 (16.81/5)$^{\rm c}$
$\min(\chi^2/\nu)$	1.11	1.11	1.31

Note. — The values quoted are the median parameter and symmetric 68% confidence interval (1σ equivalent) derived from the MCMC run.

[a]Assumes $n_{\rm ISM} = 1$ cm^{-3} and $\Theta = 1^\circ$.

[b]The forms of the prior for ζ and η are identical (see Table 5.2).

[c]A flat prior is used for both Δ and q. The former is allowed to take values between [-10,10] and the latter is constrained to the range [-1,1.5].

[d]The penalty normalization for Model AJ is taken from Model AC; likewise that for Model RAJ is from Model RAC.

preferentially inhabit environments that are under-dense compared to their AGN counterparts. Heinz offers several explanations, notably that microquasars may produce self-encasing low density bubbles either as a remnant of the birthing supernova explosion, or via persistent kinetic outflows from the compact source.

The enthalpy of the low density cavity in J1550, $\sim 10^{40} - 10^{42}$ erg, is likely maintained by the steady (or quasi-steady) AU-scale jets known to be present in the hard or quiescent state of black hole binaries (Remillard & McClintock 2006; Gallo et al. 2006). The $\sim 20\%$ measured asymmetry in the east-west extent of the cavity is unlikely to be a result of a high proper motion of the binary because this would require an extreme velocity $\sim 0.1c$. Rather, this asymmetry is easily explained as arising from a moderate 20% variation in the density of the ISM across the pc-scale region spanned by the jets. This supposition is quite plausible, given that J1550 is located only ~ 140 pc from the Galactic plane.

One interesting feature of our best-fitting model is shown in Figure 5.2: The onset of X-ray emission for the western jet is first observed after the jet has reached the outer wall of the cavity, whereas for the eastern jet it occurs well before reaching the outer wall. Although there are not enough data to draw a firm conclusion, this difference in behavior suggests that our model oversimplifies by describing a succession of low-grade density jumps (from previous episodes of jet activity) as one single jump at $R_{\rm cr}$. Alternatively, perhaps one or several dense filaments of gas breached the eastern cavity walls, causing X-ray brightening at the shock front, but without contributing appreciable mass.

We close our discussion by noting again that our lack of knowledge of the

position angle of the binary restricts us to testing for spin-orbit alignment along the line of sight. The test we have performed nevertheless provides important support for the continuum-fitting measurement of J1550's spin, which used the orbital inclination angle as a proxy for the inclination of the black-hole spin axis (Steiner et al. 2011). For the case of J1550, we have shown that these two inclination angles are consistent within several degrees.

5.8 Conclusions

Building on earlier work by Hao & Zhang (2009) and Wang et al. (2003), we have used *Chandra* and radio imaging data to model the ballistic motion of the jets of J1550. We take the time of J1550's giant X-ray flare, which was promptly accompanied by the ejection of small-scale ($\sim$ 1000 AU) relativistic radio jets, as the launch date of the large-scale ballistic jets. Using our MCMC code and a kinematic model of the jets, we find that J1550 is enclosed in a pc-scale cavity that is moderately asymmetric, and that the jets are inclined by between 64° and 83° to our line of sight (90% confidence). These impulsive jets are extremely energetic, having been launched with a total energy of $\sim 10^{46}$ erg $\frac{n_{\rm ISM}}{1{\rm cm}^{-3}} \left(\frac{\Theta}{1\ {\rm deg}}\right)^2$.

By comparing our derived inclination angle for the spin axis of the black hole (taken to be the jet inclination angle) to the orbital inclination angle, we arrived at our primary result: We find no evidence for misalignment in our comparison of orbital and jet inclinations, and we conclude that the spin and orbital inclinations differ by < 12 degrees (90% confidence). This result has a likelihood of less than 10% of occurring by chance.

Theory predicts that accretion torques acting over time will have brought most black holes into alignment with the orbital plane of their binary hosts. This prediction underpins the continuum-fitting method. In the case of J1550, our results provide support for such alignment and for the measured spin of its black hole primary.

Chapter 6

The Distance, Inclination, and Spin of the Black Hole Microquasar H1743–322

J. F. Steiner, J. E. McClintock, & M. J. Reid *The Astrophysical Journal*, Vol. 745, pp. L7-L11, 2012[1]

Abstract

During its 2003 outburst, the black-hole X-ray transient H1743–322 produced two-sided radio and X-ray jets. Applying a simple and symmetric kinematic model to the trajectories of these jets, we determine the source distance, 8.5 ± 0.8 kpc, and

[1]Reproduced by permission of the AAS.

the inclination angle of the jets, $75° \pm 3°$. Using these values, we estimate the spin of the black hole by fitting its *RXTE* spectra, obtained during the 2003 outburst, to a standard relativistic accretion-disk model. For its spin, we find $a_* = 0.2 \pm 0.3$ (68% limits); $-0.3 < a_* < 0.7$ at 90% confidence. We rule strongly against an extreme value of spin: $a_* < 0.92$ at 99.7% confidence. This makes H1743–322 the third known black hole known to produce jets and also have a moderate spin. Our result, which depends on an empirical distribution of black hole masses, takes into account all known sources of measurement error.

6.1 Introduction

About 50 stellar-mass black holes have been discovered and about two dozen of these have been well studied at optical or radio wavelengths (Remillard & McClintock 2006; Özel et al. 2010). They are all accretion-powered X-ray sources located in X-ray binary systems. In each system, the X-ray source is fueled by gas that feeds from a mass-donor star into the black hole's accretion disk. Within a few hundred kilometers of the black hole, the gas reaches a temperature of $\sim 10^7$ K and produces a luminosity that can approach the Eddington limit ($\sim 10^{39}$ erg s^{-1}). More than 80% of such sources are transient, with outbursts lasting a year or so followed by years or decades of quiescence. Typically, the host binaries have short orbital periods ($P \sim 1$ day) and are comprised of a low-mass ($\lesssim 1\ M_\odot$) secondary star and a $\sim 10 M_\odot$ black hole. Presently, neither the masses nor the orbital period of our featured system, H1743–322, are known. Nevertheless, as we now describe, the wealth of data available for H1743–322 (hereafter H1743) strongly indicates that it

is a typical short-period black hole transient.

Studies of X-ray spectral and timing data leave little doubt that H1743 contains a black hole primary (Kalemci et al. 2006; McClintock et al. 2009; Motta et al. 2010), notwithstanding the lack of dynamical evidence. While large outbursts of H1743 occurred in 1977, 2003 and 2008, our focus here is on the major 2003 outburst. During this 9-month active period, H1743 was observed 170 times using the PCA and HEXTE detectors aboard the *Rossi X-ray Timing Explorer* (*RXTE*) (McClintock et al. 2009). The source exhibited two distinct phases of evolution: (1) During the first three months (when the source was observed on an almost daily basis) H1743 flared continually and violently and was in the steep power-law (SPL) or intermediate (SPL:Hard) state (see Remillard & McClintock for discussion of these X-ray states). On the 47th day of outburst (MJD 52766), an event of central importance occurred – the radio/X-ray jets we model were launched during an intense power-law flare (discussed below). (2) During the next four months, the source was locked in the thermal dominant (TD) state, and the source intensity decayed smoothly and monotonically. It is primarily these TD-state data that we use to determine the spin of H1743.

An important X-ray timing result derived from the 2003 outburst was the discovery of a pair of quasi-periodic oscillations (QPOs) at 240 Hz and 165 Hz (Homan et al. 2005; Remillard et al. 2006). Similar high-frequency (HF) QPOs with a commensurate frequency ratio of 3:2 are seen for three other dynamically-confirmed black holes (XTE J1550–564, GRO J1655–40 and GRS 1915+105).

About one year after the onset of the 2003 outburst, bipolar X-ray jets were

discovered and observed a total of three times using *Chandra* (Corbel et al. 2005). Radio observations, which commenced several months before the X-ray observations, resulted in four detections of the eastern jet (only), followed about two months later by a single detection of the western jet (Corbel et al. 2005). Large-scale X-ray jets are rare, having been previously observed for only one other microquasar, namely XTE J1550–564, which is similar in many respects to H1743 (for comparisons, see McClintock et al. 2009). In its 1998 outburst, XTE J1550–564 produced relativistic jets at early times whose launch date was unambiguously tied to the occurrence of a remarkable X-ray flare (Hannikainen et al. 2009; Steiner & McClintock 2012).

H1743's X-flare on MJD 52766 showed striking similarities to the flare from XTE J1550–564 (see Figure 12 of McClintock et al. 2009). Of particular note, both flares occurred during a dip in the X-ray rms power (0.1–10 Hz), a jump in frequency of the low-frequency QPOs, onset of the high-frequency QPOs, and the apex of power-law emission (Sobczak et al. 2000b; Remillard et al. 2006). The similar character of these two flares, and the coincidence for XTE J1550–564 between the X-ray flare and the launch date of the jet, motivated us to search the VLA archive for additional observations of H1743. This search was fruitful, and in Section 6.2 we report three additional radio jet detections at early times that link the jets to the 2003 X-ray flare.

To deduce the source distance and jet inclination angle of H1743, we model the proper-motion data derived from the X-ray and radio observations. In doing so, we closely follow our recent study of the large-scale X-ray/radio jets of XTE J1550–564 (Steiner & McClintock 2012), which builds on the pioneering work of Wang et al. (2003) and Hao & Zhang (2009). Using a model originally applied to

gamma-ray bursts, we concluded that XTE J1550–564 is embedded in a pc-scale cavity in which the jets expanded unimpeded until they impacted the cavity walls and rapidly decelerated. We apply this same model to H1743 and obtain constraints on the distance and jet inclination angle (presumed to be the inclination of the spin axis; see Steiner & McClintock 2012).

The evolution of H1743's jets have already been studied by Hao & Zhang (2009); however, our aims differ from theirs. They were primarily interested in the environment of the black hole. While assuming an earlier launch date for the jets, they adopted the nominal values of distance and inclination ($D = 8$ kpc and $i = 73°$) suggested by Corbel et al. (2005). Our attention is focused on deriving accurate constraints on D and i for H1743, which we use in turn to constrain the spin of the black hole[2].

We estimate the spin of H1743 using the continuum-fitting (CF) method (McClintock et al. 2011; Zhang et al. 1997). In the CF method, one estimates the inner radius of the accretion disk $R_{\rm in}$, which is identified with the radius of the innermost stable circular orbit $R_{\rm ISCO}$. Knowing both $R_{\rm ISCO}$ and M is equivalent to knowing the spin parameter a_* because $R_{\rm ISCO}/M$ is a monotonic function of a_*, decreasing from 6 to 1 as the spin parameter increases from 0 to 1 (Bardeen et al. 1972)[3]. In the CF method, one determines $R_{\rm ISCO}$ by modeling the X-ray continuum spectrum of the dominant thermal component using a fully relativistic model of

[2]We express black hole spin in the customary way as the dimensionless quantity $a_* \equiv cJ/GM^2$ with $|a_*| \leq 1$, where M and J are respectively the black hole mass and angular momentum.

[3]Using $c = G = 1$.

a thin accretion disk. The observables are X-ray flux, temperature, distance D, inclination i, and mass M. In order to obtain reliable values of a_*, it is essential to select X-ray spectra that have a strong thermal component and to have accurate estimates of D, i and M. For H1743, we use our jet model to determine the first two parameters, and we estimate M using the known distribution of black hole masses for X-ray transient sources.

6.2 Data

To search for the presence of radio jets near the time of their expected production (Section 6.1), we examined high spatial resolution A-configuration VLA images taken early during H1743's 2003 outburst (see McClintock et al. 2009). Calibrated data from the VLA archive for MJD 52779.4, 52782.4, and 52786.4 were imaged using the Astronomical Image Processing System (AIPS) task IMAGR. The source was detected at 8.4 and 14.9 GHz, but here we only use the 14.9 GHz data, which had sufficient angular resolution to clearly resolve source components. The synthesized beam was approximately 0.6″ by 0.2″ elongated north-south. Fortunately, the jet position angle is almost exactly east-west (Corbel et al. 2005), allowing us to identify components separated by $\gtrsim 0.2''$. At all three epochs, the source displayed a dominant component and a weak component offset towards the west. At MJD 52779.4, just 13 days after H1743's X-ray flare, their separation was 166 ± 20 mas. Later, on MJD 52782.4 and MJD 52786.4 the separations were 256 ± 20 mas and 288 ± 20 mas, respectively.

The majority of jet data considered in our analysis are taken from Tables 1 and

3 of Corbel et al. (2005). These tables provide jet-source separation measurements for radio and X-ray observations which were conducted from 6 months onward following H1743's jet-launching flare. The X-ray data consist of three $\sim$ 30 ks *Chandra* X-ray observations in which both jets were detected. In radio, Corbel et al. (2005) report on five observations from the Australian Telescope Compact Array (ATCA). The eastern jet was present in each image, but the western jet was detected only in the final observation. All of the X-ray and radio observations were carried out between MJD 52955 and MJD 53092, when the jet-source separations were in the range $\sim 4'' - 7''$. The substantially larger angular separations of the eastern jet indicate that it is approaching and the western jet is receding.

In determining the spin of H1743, we analyze the full set of *RXTE* PCU-2 "standard 2" data obtained during the 2003 outburst, with the spectra binned into 170 half-day intervals. These spectra have been modeled in detail by McClintock et al. (2009) and Steiner et al. (2009a), and we use the same data reduction procedures here. Briefly, all the data are dead-time corrected, background subtracted, and analyzed with the inclusion of a 1% systematic uncertainty (Jahoda et al. 2006). We standardize all detector calibrations to the Toor & Seward (1974) values for the Crab using a custom model which adjusts both the overall flux normalization and the spectral shape (see Steiner et al. 2010). During the early weeks of the outburst cycle, *RXTE*'s pointing was offset by 0.32° from H1743. We have corrected the fluxes to the full collimator transmission by assuming a triangular response with FWHM = 1° (see Steiner et al. 2009a).

6.3 The Ballistic Jets: Model and Results

Our jet model, which is based on one developed by Wang et al. (2003), was first applied in describing gamma-ray-bursts. Here, we consider a pair of symmetric jets, each ejected with an initial kinetic energy E_0 and Lorentz factor Γ_0. During their expansion, the jets decelerate as they sweep up gas in their path. Assuming adiabatic expansion, the evolution of each jet is governed by:

$$E_0 = (\Gamma - 1)M_0c^2 + \sigma(\Gamma_{\rm sh}^2 - 1)m_{\rm sw}c^2, \tag{6.1}$$

where Γ is the bulk Lorentz factor of the jet, M_0 the mass of the ejecta, σ is a numerical factor of order unity[4], and $\Gamma_{\rm sh}$ is the Lorentz factor of randomly accelerated particles at the shock front. The entrained mass, $m_{\rm sw}$, is given by $m_{\rm sw} = \Theta^2 m_{\rm p} n \pi R^3/3$, where Θ is the jet half opening angle, n the gas density, $m_{\rm p}$ is the mass of a proton, and R the distance traveled by the jet.

We evolve Eqn. 6.1 in 2-hour time steps, using the inclination of the jet axis to the observer's line of sight (θ) to calculate the projected separation (δ) between each jet and the central source: $\delta(t') = R(t)\sin\,\theta/D$. Here, $t' = t \pm R(t)\cos\,\theta/c$ is the observer's time, which takes into account for each jet the time delay between H1743's rest frame and the frame of the observer.

Our full model requires just five parameters: D, θ, Γ_0, the launch date T_0, and $\tilde{E}$, the effective energy[5]. Because of the association with the X-ray flare, the prior on the launch date is taken to be MJD 52766 ± 5 days; we adopt a flat prior on θ, D,

[4] σ ranges from 0.35 in the ultrarelativistic limit to 0.73 in the nonrelativistic limit. For additional details concerning our model, see Steiner & McClintock (2012).

[5] $\tilde{E} \equiv E_0(n/10^{-2}{\rm cm}^{-3})^{-1}(\Theta/1^\circ)^{-2}$. Following our approach for XTE J1550–564

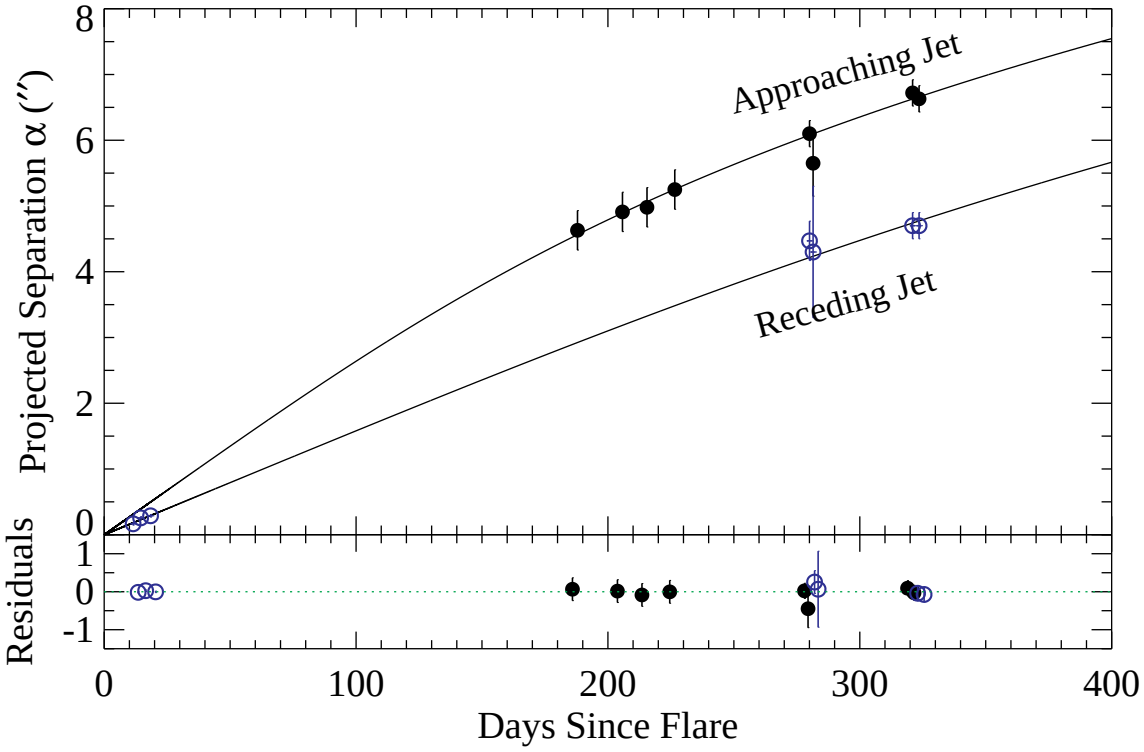

Figure 6.1.— Our best fit model for the motion of H1743's radio and X-ray jets. The eastern jet is marked by filled circles and the western jet by open circles. Fit residuals are shown in the bottom panel using a slight offset in time between eastern and western jets.

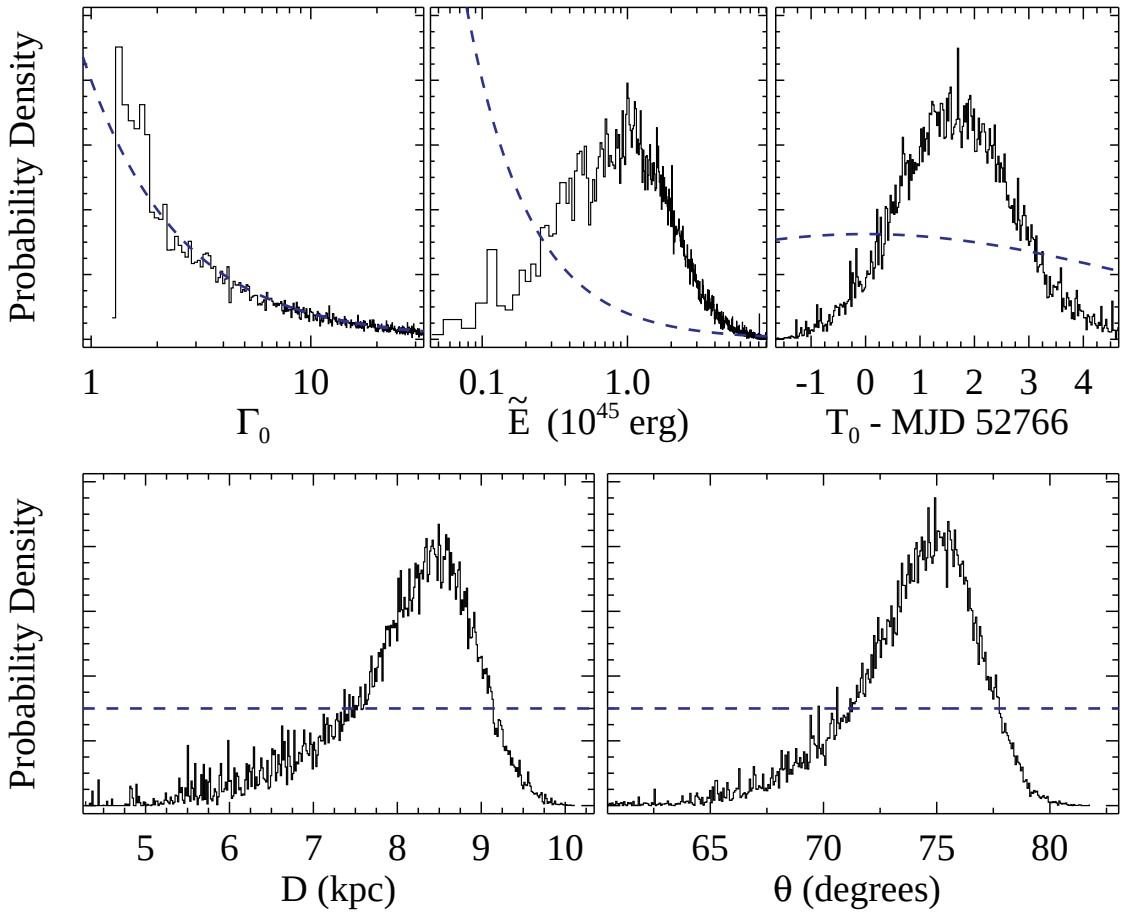

Figure 6.2.— Marginalized probability densities from the MCMC model are shown to arbitrary scale. The prior for each parameter is indicated by a dashed line. Γ_0 is constrained by its prior at large values, but the other parameters show little dependence on their priors.

$\log(\Gamma_0)$, and $\log(\tilde{E})$. Our model is fitted via a Markov chain Monte Carlo (MCMC) routine developed using the Metropolis-Hastings algorithm (Hastings 1970) which has been previously applied with this jet model in Steiner & McClintock (2012). The chains are evolved until they are well converged, using $\sim 2 \times 10^5$ elements total[6].

From the VLA data alone, the identification of the pair of radio sources is ambiguous. We have applied our model by attributing to the two radio sources each allowed combination of eastern jet, western jet, and core. The most probable interpretation is that the two sources correspond to core and western jet emission. Alternative pairings are ruled out at $> 97\%$ confidence by our model.

The best fit achieved by the MCMC run is shown in Figure 6.1 and reaches a goodness of fit $\chi^2/\nu = 4.9/9 = 0.54$. Obviously, further modification to the model is not needed[7]. Distributions for the model parameters are shown in Figure 6.2. Of chief importance, we find that distance and inclination are well constrained: $D = 8.5 \pm 0.8$ kpc and $i = 75^\circ \pm 3^\circ$. The time at which the jets were produced is strongly constrained to T_0 =MJD 52767.6 ± 1.1 days, independent of the prior. This timing supports a connection between H1743's X-ray flare and the production of its jets. The speed of the jets, Γ_0, has a relatively low maximum a posteriori estimate, $\Gamma_0 \sim 1.4$, but is poorly constrained at high values and tracks its prior. For the kinematic energy of each jet, we obtain a large uncertainty of ≈ 0.5 dex centered

(Steiner & McClintock 2012), we scale Θ and n using typical values, with density 100 times lower than for the interstellar medium.

[6]An additional $\approx 10^5$ chain elements were not used, which were generated during training and burn-in phases.

[7]We have explored the asymmetric models employed for XTE J1550–564 (Steiner & McClintock 2012); i and D are unchanged.

around $\tilde{E} \approx 10^{45}$ erg. This implies that H1743's jets are nearly tenfold less energetic than those produced in the 1998 outburst of XTE J1550–564, or alternatively that for H1743 either (1) the density of the surrounding medium is much lower or (2) the jet opening angle is substantially smaller.

6.4 X-ray Continuum-Fitting Analysis

We now estimate the spin of H1743 by fitting its X-ray spectra. For the three crucial input parameters, we use the values of D and i derived in the preceding section and the distribution of black hole masses discussed below. All of our analysis is performed using XSPEC v12.7.0 (Arnaud 1996). Following Steiner et al. (2009a) and making minor adjustments, our spectral model has the form TBABS(SIMPL⊗KERRBB2), where TBABS and KERRBB2 are respectively the low-energy-absorption and accretion-disk components. The component SIMPL scatters a fraction of the thermal disk photons into a Compton power law. For H1743, this simple convolution model describes only the broad continuum components and is unaffected by the inclusion of weaker features, e.g., warm absorbers or spectral reflection.

The four free parameters of the spectral model[8] are the (1) fraction of thermal photons $f_{\rm SC}$ scattered into the Compton power law; (2) power-law index Γ; (3) spin parameter a_*; and mass accretion rate $\dot{M}$. Mass, inclination, and distance are varied in 5×10^3 Monte-Carlo samples, and all 170 spectra are fitted for each

[8]Column density $N_{\rm H}$ is frozen at $2.0{\times}10^{22}$ cm^{-2} (Blum et al. 2009). For KERRBB2, limb darkening and returning radiation are switched on and the torque at the inner boundary is set to zero. For SIMPL, we use the faster upscattering-only option.

setting. Uncertainty in the absolute calibration of the X-ray flux is accounted for by randomly varying the overall flux normalization by 10% for each triplet setting of M, i, and D (e.g., Steiner et al. 2011). We similarly marginalize over uncertainty in the viscosity parameter α by randomly assigning either $\alpha = 0.01$ or $\alpha = 0.1$ (e.g., King et al. 2007; Pessah et al. 2007), which are two representative values available to our model. Both of these uncertainties have a small effect on a_* compared to our dominant uncertainty, the unknown black hole mass. (Uncertainty in the mass accounts for 50% of our final uncertainty in spin.)

For each of the 5×10^3 parameter settings, we apply our standard data selection criteria: disk luminosity between 3% and 30% of the Eddington limit; goodness of fit ($\chi^2/\nu < 2$); and a power-law normalization $f_{\rm SC} < 25\%$ (Steiner et al. 2009a). Typically, about 30 spectra pass this screening. Finally, each of the 5×10^3 samples is given a weight according to the mass distribution assumed, and random draws are made from the selected spectra to achieve an estimate of spin. The dependence between the inferred value of spin and the black hole's mass is illustrated in Figure 6.3. As mass is varied from $M = 5{\rm M}_\odot$ to $15{\rm M}_\odot$, spin changes from $a_* \approx -0.25$ to $a_* \approx 0.75$.

Recently, Özel et al. (2010) compiled all the dynamical measurements of mass for black hole transients and determined the following best-fit probability distribution, which we adopt:

$$P(M) = \begin{cases} {\rm Exp}[(6.30{\rm M}_\odot - M)/1.57{\rm M}_\odot]/1.57{\rm M}_\odot, & M > 6.3{\rm M}_\odot, \\ 0, & M \leq 6.3{\rm M}_\odot. \end{cases} \tag{6.2}$$

In Figure 6.4, we show the spin which results when the Özel et al. (2010) mass

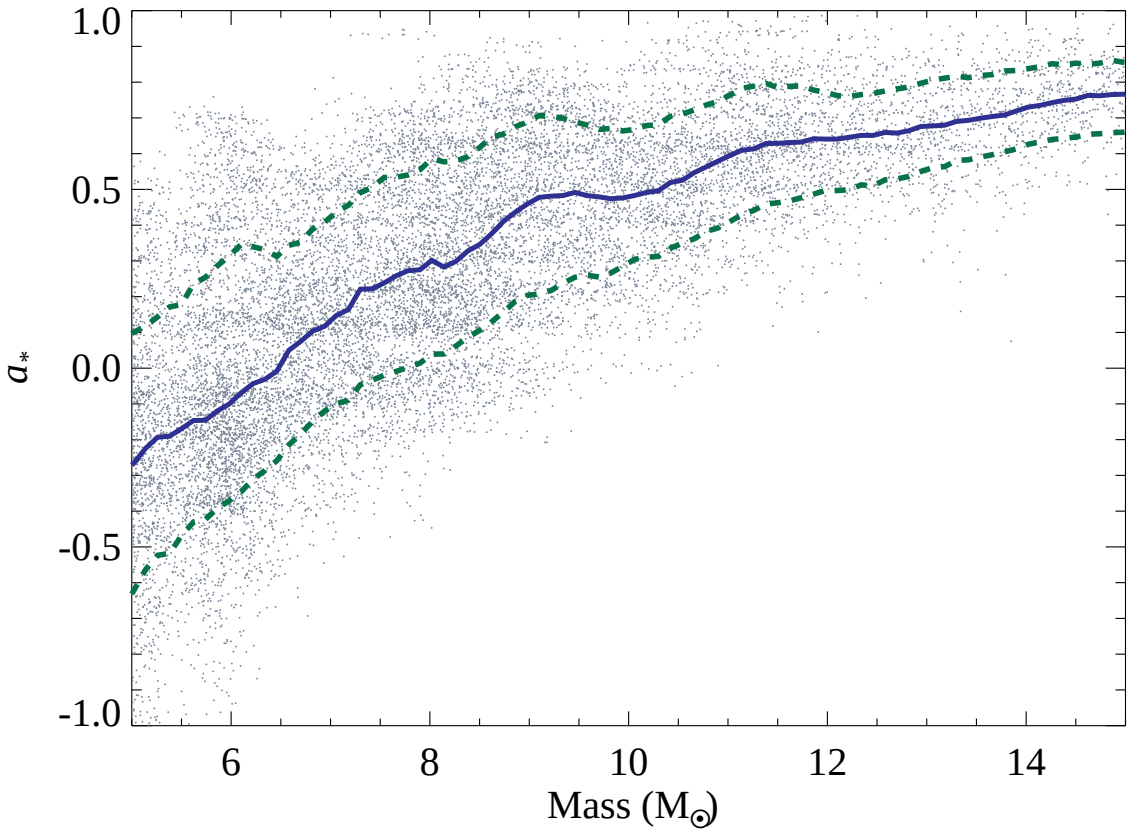

Figure 6.3.— The dependence of spin on black hole mass. These estimates incorporate all sources of measurement error. The solid line tracks the average spin at each mass, and the associated 68% confidence interval corresponds to the region between dashed lines.

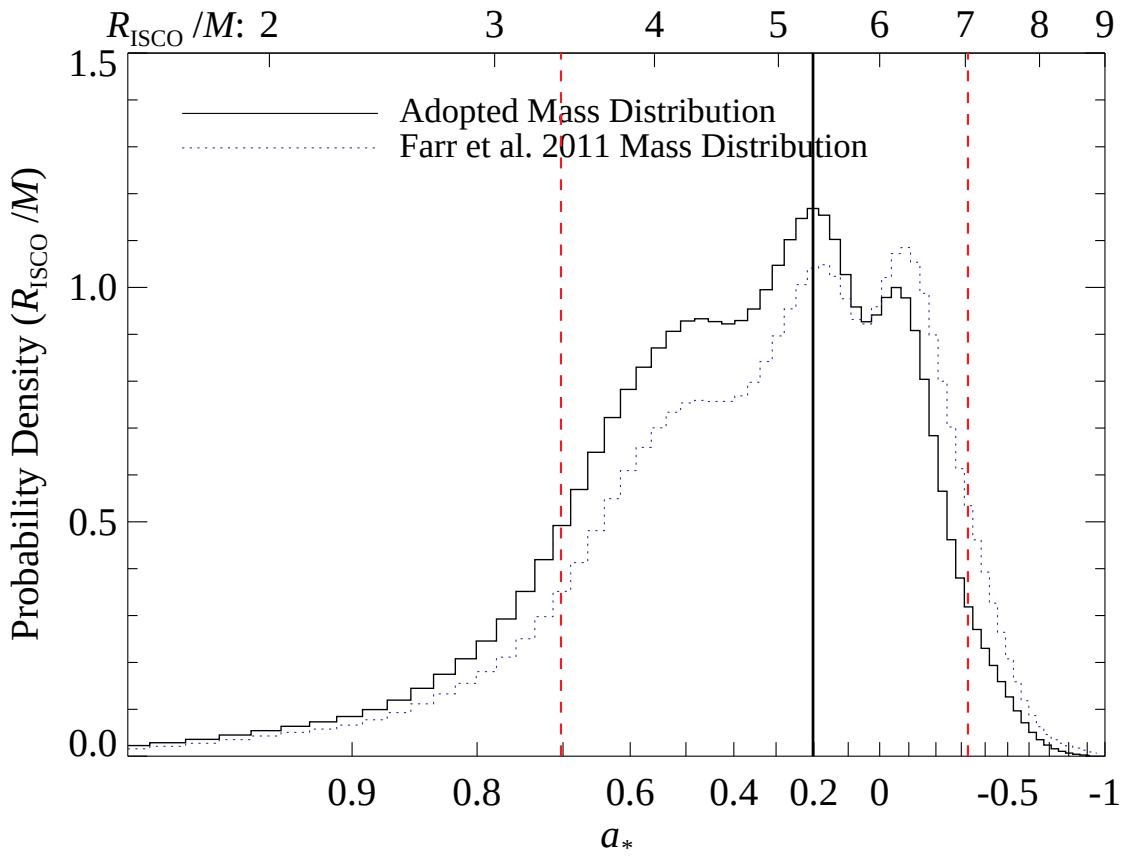

Figure 6.4.— Spin probability for the dimensionless measurement variable $R_{\rm ISCO}/M$ (top axis) which is uniquely associated with spin (bottom axis). This spin estimate is obtained by using the adopted transient black hole mass distribution from Özel et al. (2010) (solid curve). The vertical solid line indicates the maximum likelihood spin, while the 90% confidence range is bounded by dashed vertical lines. For comparison, we also show the spin estimate from using the mass distribution of Farr et al. (2011) (dotted curve). These results take into account uncertainties in M, i, D, α and the absolute X-ray flux calibration. For illustration, the distributions over $R_{\rm ISCO}/M$ have been smoothed using a Gaussian kernel with 10% width.

distribution is assumed. We find $a_* = 0.20^{+0.34}_{-0.33}$ (68% confidence interval) with a 90% confidence interval of $-0.33 < a_* < 0.70$. From this analysis, we find that high values of spin at $a_* > 0.92$ are ruled out at 3σ confidence. This makes H1743 one of a growing population of black-hole microquasars known to have moderate spin (e.g., A0620–00, $a_* \approx 0.1$; Gou et al. 2010, XTE J1550–564, $a_* \approx 0.5$; Steiner et al. 2011).

In addition to the adopted distribution of masses, in Figure 6.4, we also show results calculated using the favored mass distribution from Farr et al. (2011); those authors considered the same measurements used by Özel et al. (2010), but found that a power-law distribution gave the best fit, with form $P(M) \propto M^{-6.4}$ over the mass range $6.1\mathrm{M}_\odot \leq M \leq 23\mathrm{M}_\odot$ (and $P(M) = 0$ elsewhere). When comparing the Farr et al. (2011) distribution with our adopted result, the difference is minor: $\Delta a_* \approx 0.05$.

6.5 Conclusions

We have modeled the proper motion of the radio and X-ray jets of H1743 that were launched during an X-ray flare. Based on our purely kinematic model, we obtain firm estimates of the source distance, 8.5 ± 0.8 kpc, and the jet inclination angle, $75^\circ \pm 3^\circ$. Using these constraints on D and i, we fitted all 170 X-ray spectra collected during the 2003 outburst of H1743, applied our data selection criteria, and derived a relationship between spin and black hole mass. We then constrained the mass of H1743 using an analytic distribution for transient systems that are similar to H1743, thereby arriving at our final result: $a_* = 0.2 \pm 0.3$; $-0.3 < a_* < 0.7$ at 90% confidence. Meanwhile, we rule strongly against an extreme value of spin: $a_* < 0.92$

at 99.7% confidence. Two similar microquasars have been identified which also produced powerful jets while harboring black holes with moderate spins: A0620–00 ($a_* = 0.1$; Gou et al. 2010) and J1550–564 ($a_* = 0.5$; Steiner et al. 2011).

This is the first successful application of the X-ray continuum-fitting method that does not rely on any dynamical data to place constraints on one or more of the input parameters D, M and i – even the orbital period of H1743 is presently unknown! Our constraint on a_* can be tightened once a dynamical estimate of mass has been obtained.

Chapter 7

The Spin of the Black Hole Microqusar XTE J1550–564 via the Continuum-Fitting and Fe-Line Methods

J. F. Steiner, R. C. Reis, J. E. McClintock, R. Narayan, R. A. Remillard, J. A. Orosz, A. C. Fabian, & M. A. P. Torres *Monthly Notices of the Royal Astronomical Society*, Vol. 416, pp. 941-958, 2011

Abstract

We measure the spin of XTE J1550–564 using the two leading methods: modeling the thermal continuum spectrum of the accretion disc, and modeling the broad red wing of the reflection fluorescence Fe $K\alpha$ line. We find that these two independent measurements of spin are in agreement. For the continuum-fitting analysis, we use a data sample consisting of several dozen *RXTE* spectra, and for the Fe $K\alpha$ analysis, we use a pair of *ASCA* spectra from a single epoch. Our spin estimate for the black-hole primary using the continuum-fitting method is $-0.11 < a_* < 0.71$ (90 per cent confidence), with a most likely spin of $a_* = 0.34$. In obtaining this result, we have thoroughly explored the dependence of the spin value on a wide range of model-dependent systematic errors and observational errors; our precision is limited by uncertainties in the distance and orbital inclination of the system. For the Fe-line method, our estimate of spin is $a_* = 0.55^{+0.15}_{-0.22}$. Combining these results, we conclude that the spin of this black hole is moderate, $a_* = 0.49^{+0.13}_{-0.20}$, which suggests that the jet activity of this microquasar is powered largely by its accretion disc rather than by the spin energy of the black hole.

7.1 Introduction

During its principal 1998–1999 outburst cycle, the bright X-ray transient XTE J1550–564 produced one of the most remarkable flare events ever observed for a black-hole binary. For $\approx$ 1 day, the source intensity rose fourfold relative to neighbouring plateau values, reaching 6.8 Crab. The flux in the dominant

power-law component rose by the same factor, and then just as quickly its intensity declined (Sobczak et al. 2000a; McClintock et al. 2009). Four days later, AU-scale superluminal radio jets were observed (Hannikainen et al. 2009). Their separation angle (~ 255 mas) and relative velocity (~ 65 mas d^{-1}) links the birth of these jets to the impulsive X-ray flare. The subsequent detection of large-scale radio jets in 2000 led to the discovery of relativistic X-ray jets (Corbel et al. 2002; Kaaret et al. 2003; Tomsick et al. 2003). All of the available evidence strongly indicates that these pc-scale X-ray and radio jets were produced during the unique 7-Crab flare event, and we adopt this view.

The microquasar XTE J1550–564 (hereafter J1550) is further distinguished by a pair of high-frequency X-ray oscillations with a 2:3 frequency ratio (184 and 276 Hz; Miller et al. 2001; Remillard et al. 2002a). During its 1998–1999 eruption, J1550 displayed all of the active accretion states: hard, steep power law (SPL), thermal dominant (TD) and intermediate (INT; Remillard & McClintock 2006). The X-ray spectral and timing properties of this source have been comprehensively studied by many authors (e.g., Sobczak et al. 2000a; Homan et al. 2001; Remillard et al. 2002b; Kubota & Done 2004; Dunn et al. 2010), as have the properties of its radio counterpart (Corbel et al. 2001; Xue et al. 2008; Hannikainen et al. 2009).

Likewise, the optical counterpart of J1550 was the subject of a comprehensive dynamical study by Orosz et al. (2002). The measurement by these authors of a large mass function immediately established J1550 as a dynamically-confirmed black-hole binary with a $\approx 10\ M_\odot$ black-hole primary in a 1.55-day orbit with a late G or early K companion. This dynamical model was recently revisited using new photometric and spectroscopic data (Orosz et al. 2011). Our higher-resolution

spectra (60 km s^{-1}) revealed that the mass ratio is extreme ($Q \approx 30$) and yielded a refined value of the mass function, $f(M) = 7.65 \pm 0.38\ M_{\odot}$. Of central importance to the present chapter, Orosz et al. (2011) report accurate values of the three key quantities that are essential for determining the spin of the black hole via the continuum-fitting method, namely the distance $D = 4.38^{+0.58}_{-0.41}$ kpc, black-hole mass $M = 9.10 \pm 0.61\ M_{\odot}$, and orbital inclination angle $i = 74\overset{\circ}{.}7 \pm 3\overset{\circ}{.}8$.

Currently, the two principal methods for measuring black hole spin[1] are modeling the thermal spectrum of the accretion disc (Zhang et al. 1997) and modeling the profile of the Fe $K\alpha$ line (Fabian et al. 1989; Laor 1991). For both methods, spin is measured by estimating the inner radius of the accretion disc, $r_{\rm in} \equiv R_{\rm in}/M$, in standard GR units ($G = c = 1$). $R_{\rm in}$ is identified with the radius of the innermost stable circular orbit ($R_{\rm ISCO}$) about the black hole and is related to spin via a monotonic mapping between the dimensionless ISCO radius $R_{\rm ISCO}/M$ and the dimensionless spin parameter a_* (Shapiro & Teukolsky 1983). Strong support for linking $R_{\rm in}$ to $R_{\rm ISCO}$ is provided by decades of empirical evidence that $r_{\rm in}$ is constant in disc-dominated states of black-hole binaries (e.g., Tanaka & Lewin 1995; Done et al. 2007). This is shown most compellingly in our recent study of the persistent source LMC X-3 (Steiner et al. 2010). Theoretical support for identifying $R_{\rm in}$ with $R_{\rm ISCO}$ is provided by magnetohydrodynamic simulations of thin accretion discs (Reynolds & Fabian 2008; Shafee et al. 2008; Penna et al. 2010; Kulkarni et al. 2011;

[1]Black-hole spin is commonly expressed in terms of the dimensionless quantity $a_* \equiv a/M = cJ/GM^2$, where M and J are respectively the black-hole mass and angular momentum (Shapiro & Teukolsky 1983). Its limiting value is $a_* = +1$ (-1) for a maximal Kerr hole rotating in a prograde (retrograde) sense relative to the accretion disc; $a_* = 0$ corresponds to a non-spinning Schwarzschild hole.

but see Noble et al. 2009, 2010). In short, the relationship for thin accretion discs between $r_{\rm in}$, $R_{\rm ISCO}$ and a_* is the foundation of both the continuum-fitting and Fe $K\alpha$ methods of measuring spin.

In the continuum-fitting (CF) method, one determines $R_{\rm ISCO}$, and thereby a_*, via measurements of X-ray temperature and luminosity (i.e., using X-ray flux, distance D and inclination angle i) of the disc emission. In order to obtain reliable values of a_*, it is essential to (1) select X-ray spectra that have a strong thermal component and (2) have accurate estimates of D, M and i, like those given above for J1550. In practice, we fit the X-ray spectrum of the black hole's accretion disc to our version of the Novikov-Thorne thin accretion disc model (Novikov & Thorne 1973; Li et al. 2005; McClintock et al. 2006) using an advanced treatment of spectral hardening (Davis et al. 2005; Davis & Hubeny 2006). In this way, we have measured the spins of six other stellar black holes. We find spins ranging from $a_* \approx 0.1$ (Gou et al. 2010) to $a_* > 0.98$ (McClintock et al. 2006); four other spin values are relatively high, $a_* \approx 0.7 - 0.9$ (Shafee et al. 2006; Liu et al. 2008, 2010; Gou et al. 2009).

In the Fe $K\alpha$ method, one determines $R_{\rm ISCO}$ by modeling the profile of reflection-fluorescent features in the disc. Most prominent is the broad and asymmetric iron line, whose shape is determined by Doppler effects, light bending, and gravitational redshift (Reynolds & Nowak 2003). Of central importance is the effect of the redshift on the red wing of the line. This wing extends to very low energies for a rapidly rotating black hole ($a_* \sim 1$) because in this case gas can orbit near the event horizon, deep in the potential well of the black hole. Relative to the CF method, measuring the extent of this red wing in order to infer a_* is hindered

by the relative faintness of the signal. However, the Fe $K\alpha$ method has the virtues that it is independent of M and D, while the blue wing of the line even allows an estimate of i. What makes the Fe $K\alpha$ method enormously important is that it is the primary approach for measuring the spins of supermassive black holes in AGN. The spins of several stellar black holes (Reis et al. 2009, 2011; Miller et al. 2009b; Blum et al. 2009) and supermassive black holes (Brenneman & Reynolds 2006; Schmoll et al. 2009; Miniutti et al. 2009; Fabian et al. 2009; Zoghbi et al. 2010) have been reported using the Fe line method with values ranging from $a_* \approx 0$ to $a_* > 0.98$.

Knowledge of black-hole spin has broad importance to astrophysics: For example, spin is central to most of the many theories of relativistic jets observed for both microquasars and AGN (Blandford & Znajek 1977), and it is comparably important to collapsar models of long GRBs (Woosley 1993) and models of black-hole formation and black-hole binary evolution (Lee et al. 2002). Hierarchical models for the growth of supermassive black holes require knowledge of the spin distributions of the merging partners (Volonteri et al. 2005; Berti & Volonteri 2008), and the observed properties of AGN may be strongly conditioned by black-hole spin (McNamara et al. 2009; Garofalo et al. 2010; Tchekhovskoy et al. 2010). Spin measurements are likewise important to gravitational-wave astronomy in predicting the waveforms of merging black holes (Campanelli et al. 2006). Knowledge of black hole spin is becoming important to fundamental physics as well, and enlivening questions are being asked: e.g., Is the no-hair Theorem valid and can it be tested (Johannsen & Psaltis 2010)? Do we live in a string axiverse filled with light axions (Arvanitaki et al. 2010)?

There have been two prior estimates of J1550's spin from X-ray measurements.

The first of these, $a_* \approx 0-0.1$, was obtained using the CF method for a sample of ten *RXTE* spectra by Davis et al. (2006). Their result was based on an old dynamical model and derived using approximate values of M, i, and D (e.g., D was uncertain by ≈ 45 per cent; Orosz et al. 2002). We improve upon the work of Davis et al. by using our new dynamical model (e.g., with its fourfold better determination of D) and a ≈ 6-times larger sample of *RXTE* spectra, and by our detailed treatment of observational and model-dependent uncertainties. A second measurement of J1550's spin was performed by Miller et al. (2009b) in a forward-looking work that combined Fe $K\alpha$ and disc-continuum techniques in a preliminary study of eight sources. Their measurements were driven by constraints from the shape of the Fe $K\alpha$ component, and the spin was measured to be $a_* \approx 0.76$. Our work differs in that we have applied both methods independently, and by doing so we have been able to treat a much larger data set and also select the most reliable data suited to each method.

In this chapter, we present the spin of J1550 on two fronts. After introducing the data sets (Section 7.2), we begin by first applying the CF technique (Sections 7.3 and 7.4). This work is complemented with a thorough exploration of the statistical and systematic uncertainties inherent to the CF method (Section 7.5). Next, we measure the spin of J1550 using the Fe $K\alpha$ technique (Section 7.6), and we finish with a discussion of the results (Section 7.7) and our conclusions (Section 7.8).

7.2 Observations

The primary data set used in this study is a compendium of 347 *Rossi X-ray Timing Explorer* (*RXTE*) observations. The data include those obtained during the bright

discovery outburst in 1998–1999 on through four additional minor outbursts, the last ending in mid-2003. A light curve of the flux, showing the spectral evolution of the source, is presented in Fig. 7.1, where the spectral state assignments have been determined using precisely the model, procedures and criteria described in Remillard & McClintock (2006). Thermal dominant data, which are of primary importance for CF spin measurements, were obtained exclusively during the first outburst cycle.

RXTE spectral data are collected using PCU-2, the best calibrated and most frequently operating of the five Proportional Counter Array (PCA) detectors. Spectra are individually obtained by grouping sequential observations into approximately half-day bins, each with a typical exposure time ~ 3 ks. We follow the procedures described in McClintock et al. (2006): The data are background subtracted, a customary 1 per cent systematic error in the data count rates is included, and a dead time correction ranging from approximately 1 to 20 per cent is applied. Spectra are fitted over the energy range 2.55–45 keV using XSPEC version 12.4–12.6 (Arnaud 1996). Calibration over this range is achieved using the latest version of PCARMF (v11.7)[2].

A linear collimator correction (assuming an ideal 1° triangular response; Jahoda et al. 2006) has been applied to the data set to account for a series of offsets in the PCA pointing. Specifically, we normalised the flux upward by 4.4 per cent (a $2.'67$ offset) during the 1998–1999 outburst, and 7.1 per cent ($4.'28$ offset) during the 2000 outburst. After April 2001 the correction is just ~ 0.1 per cent. In addition to these global corrections, a handful of observations taken between 1998 September 7–9 and

[2]http://www.universe.nasa.gov/xrays/programs/rxte/pca/doc/rmf/pcarmf-11.7

on 1999 January 6 were off-target for unknown reasons by $\approx 0.2^{\circ}$ and required us to make large corrections (for details, see Steiner et al. 2009a). We estimate that the uncertainty in these flux corrections is no more than 1–2 per cent, which has a negligible impact on our spectral fitting results.

In addition to the *RXTE* data set, we also include a 25 ks *ASCA* Gas Imaging Spectrometer (GIS) observation taken on UT 1998 September 23 when the source was in an intermediate state (see the observation time in Fig. 7.1 marked by the black vertical line). Following Miller et al. (2009b) and Miller et al. (2005), we use these *ASCA* data, with twice the resolution of the *RXTE* PCA data, to examine the iron line. However, we do not report a CF analysis on these data because the Compton component in the X-ray spectrum is too strong. We use standard data products for the GIS-2 and GIS-3 spectra with version 4.0 response matrices. The two spectra are fitted jointly over the 1–10 keV energy range, and in Section 7.6 we present our analysis of these data using the Fe $K\alpha$ method.

7.3 Continuum-Fitting Analysis

We first enumerate our CF data selection requirements and define two tiers of data quality. Next, we introduce the first and principal of three Comptonised accretion-disc models which are applied to the *RXTE* data set. Then, in the following section we introduce two alternative models that differ principally in their treatment of the Compton reflection component. We find very close agreement in the spin estimate using all three models.

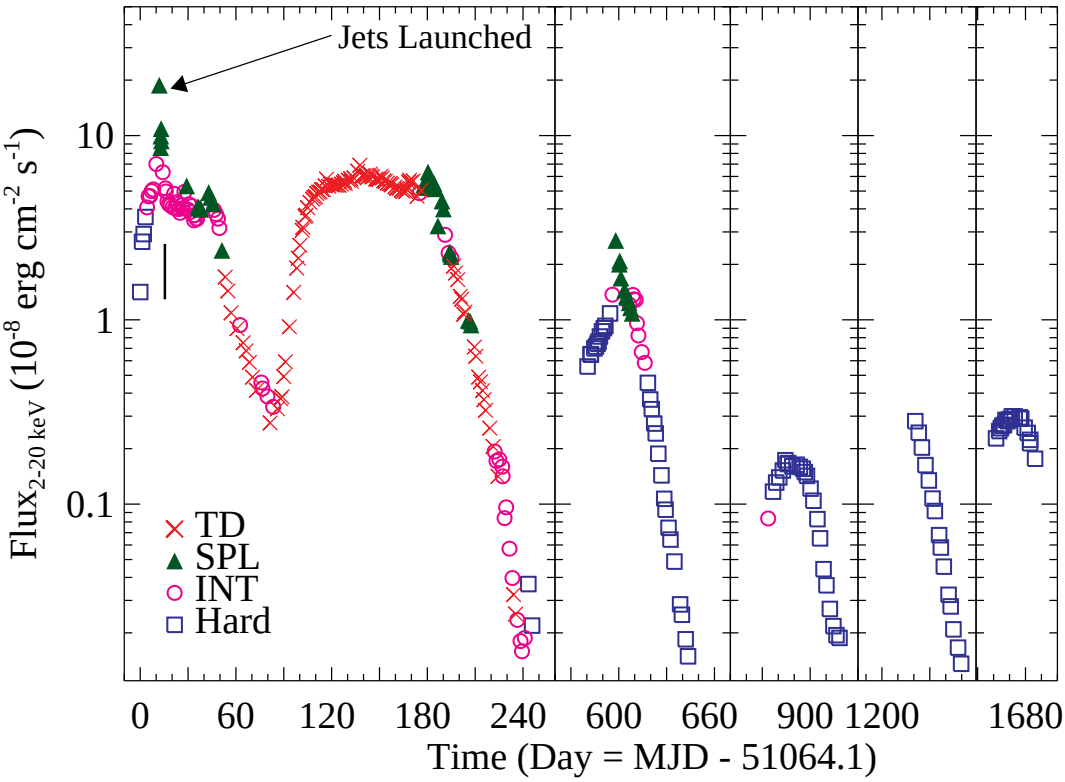

Figure 7.1.— A spectral-state encoded 2–20 keV light curve showing all five outburst cycles of J1550. Most disc-dominated data were obtained during the primary outburst in 1998–1999. The time of the *ASCA* observation, which is analysed in Section 7.6, is marked at day 15 by a solid black line. The powerful 7-Crab flare near day 12 was responsible for the ejection of superluminal radio jets.

7.3.1 *RXTE* Data Selection

We identify two tiers of quality in our data based largely on the strength of the disc component relative to the Compton component. First-class 'gold' spectra are selected from just the strongly disc-dominated TD-state observations (the most reliable for measuring spin via the CF method; e.g., Shafee et al. 2006). In these spectra, the Compton component is only a few per cent or less of the total photon flux. We additionally consider a set of second-tier 'silver' spectra in which Comptonisation is significantly stronger. These are selected from SPL-state and INT-state observations. The *gold* and *silver* spectra for J1550 are discussed and identified in an earlier study by our group, which we now describe briefly.

In Steiner et al. (2009a), we examined both J1550 and the BH candidate H1743–322, while comparing several models for the Compton power-law component (POWERLAW, COMPTT, and SIMPL), and using for J1550 the same data set considered in this work. For *gold* spectra, we showed that our spin results were weakly dependent on the choice of Comptonisation model, whereas for *silver* spectra, only SIMPL both adequately models the Compton power law and provides consistent measurements of $r_{\rm in}$. The SIMPL model achieves this performance because it ensures photon conservation and self-consistently generates the power-law component of the spectrum using the disc component as input. Following Steiner et al., we here consider only those SPL and INT spectra with strong thermal components that have power-law normalisations $f_{\rm SC} < 25$ per cent, roughly an order of magnitude greater than typical for the TD state.

For a spectrum to be classified as either *gold* or *silver* it must meet the following

requirements: (1) goodness of fit, $\chi^2/\nu < 2$; (2) $r_{\rm in}$, the parameter of interest, is determined to a precision of $r_{\rm in}/\sigma_{r_{\rm in}} > 5$; and (3) the disc luminosity lies in the range 5–30 per cent $L_{\rm Edd}$. The lower-luminosity threshold eliminates spectra that are associated with either advective flows (Esin et al. 1997) or coronal feedback effects (e.g., Beloborodov 1999). The upper luminosity threshold ensures the disc is geometrically thin (McClintock et al. 2006; Penna et al. 2010), as required by the model. The adoption of this upper limit is supported by studies of slim-disc accretion (high-luminosity disc solutions) by Sądowski et al. (2011). They show that slim-disc and scale-height effects cause significant deviations from the NT solutions above $L_{\rm D}/L_{\rm Edd} \gtrsim 0.1 - 0.5$.

7.3.2 Results I: Continuum Fitting using SMEDGE

In selecting our CF data and then determining spin, we employ a variant of the principal model from our earlier study of J1550 and H1743–322 (hereafter, Model S; Steiner et al. 2009a): CRABCOR×TBABS×SMEDGE(SIMPL⊗KERRBB2). The custom multiplicative component CRABCOR corrects the response of the PCA detector to the Toor & Seward spectrum of the Crab (see Steiner et al. 2010; Toor & Seward 1974). TBABS (Wilms et al. 2000) is a model of low-energy photoelectric absorption for which we fix the column density of J1550 to a high-precision measurement made using *Chandra* grating data: $N_{\rm H} = 8.0^{+0.4}_{-0.3} \times 10^{21}\,{\rm cm}^{-2}$ (90 per cent confidence; Miller et al. 2003).

The key component of this model is KERRBB2 (McClintock et al. 2006), a fully relativistic thin accretion-disc model, which includes self-irradiation of the disc

('returning radiation') and limb darkening (Li et al. 2005). The effects of spectral hardening are incorporated via a pair of look-up tables for the hardening factor f (Davis et al. 2005; Davis & Hubeny 2006) corresponding to two representative values of the viscosity parameter: $\alpha = 0.01$ and $\alpha = 0.1$. Here and throughout, motivated by the results of both observational data and global GRMHD simulations (Penna et al. 2010; King et al. 2007, and references therein), we adopt $\alpha = 0.1$ as our fiducial value. Following our previous work, we use a zero-torque inner boundary condition and assume alignment of the black-hole spin axis with the binary orbital plane; we turn on both limb-darkening and returning radiation flags and fix the KERRBB2 normalisation to unity. We fix the input parameters M, i and D to their nominal values (Section 7.1). The model KERRBB2 has just two fit parameters, namely the black-hole spin a_* and the mass accretion rate $\dot{M}$, which can be reparameterised uniquely and equivalently as $r_{\rm in}$ and $L_{\rm D}/L_{\rm Edd}$ (the Eddington-scaled bolometric disc luminosity; McClintock et al. 2006).

We model the high-energy power law by convolving the thermal component with SIMPL (Steiner et al. 2009b), a model that mimics the physics of Compton scattering of thermal disc photons by a hot corona. The model SIMPL converts a fraction $f_{\rm SC}$ of the seed photons into a power law with photon index Γ. We use the standard, upscattering-only version. For the reflected component, we assume here that the disc elastically backscatters all incident Compton photons (generated by SIMPL), apart from a broad iron absorption edge feature that is modeled phenomenologically using SMEDGE (Ebisawa et al. 1994). The parameters of SMEDGE are the edge energy $E_{\rm Edge}$ (fitted from 7–9 keV), its optical depth $\tau_{\rm max}$ (unconstrained in the fit), and the width of the feature $W_{\rm Edge}$ (fixed at 7 keV). In the section that follows, we consider

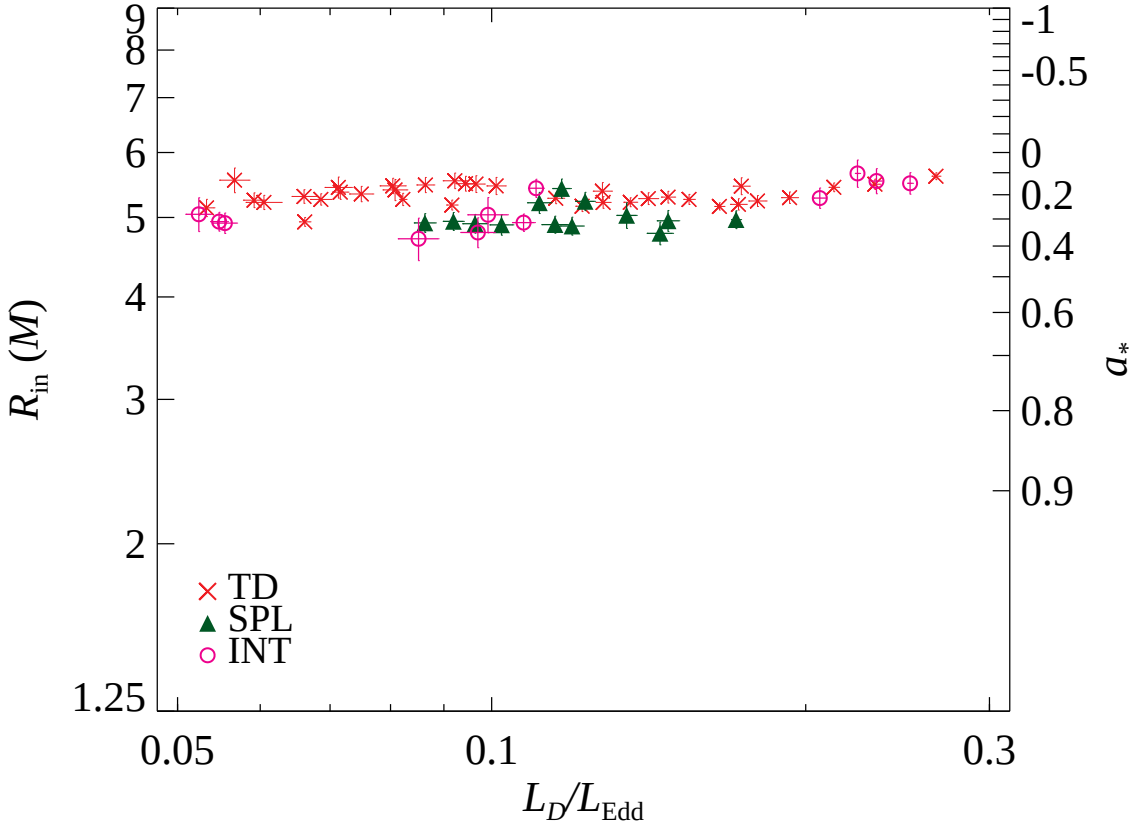

Figure 7.2.— The spin, expressed both in terms of $R_{\rm in}$ and a_*, versus luminosity. The TD spectra comprise the *gold* data set and the intermediate and SPL spectra the *silver* data set. The mean value of $R_{\rm in}$ is in agreement for the two data sets to within ≈ 5 per cent even though the Compton component is much stronger for the *silver* data. Error bars represent statistical uncertainties from X-ray spectral fitting only; they do not include the additional sources of error discussed in Section 7.5.

two models of reflection that are more physically motivated.

Applying our selection criteria to the full spectral model yields 35 *gold* spectra, where most of the winnowing is a result of our thin-disc limit on the intrinsic luminosity (i.e., prior to scattering) of the accretion-disc component: $L_{\rm D}/L_{\rm Edd} < 0.3$. We additionally select 25 *silver* spectra, 13 of which correspond to SPL-state observations and 12 to intermediate-state observations. Our spectral-fitting results are summarized in Table 7.1 (*gold* spectra correspond to entries 1–35 and *silver* to entries 36–60).

For all these selected data, in Fig. 7.2 we plot a_* versus the luminosity of the disc component $L_{\rm D}/L_{\rm Edd}$. In a departure from our earlier work, in addition to a_*, we also plot the inner disc radius $R_{\rm in}$. The two quantities are equivalent in the sense that they are simply related to each other via a monotonic analytical formula (Section 7.1). We have chosen to also show $R_{\rm in}$ because it is the quantity that is more directly determined via continuum fitting.

Fig. 7.2 shows that the *gold* and *silver* data sets give result that are in good agreement. The net weighted result for the combined data set is $a_* = 0.23 \pm 0.07$ ($r_{\rm in} = 5.22 \pm 0.24$). The *gold* data give a slightly lower value for the spin, $a_* = 0.20$, than do the *silver* data, $a_* = 0.27$; the corresponding shifts from the mean value of $r_{\rm in}$ are respectively $+2$ per cent and -3 per cent.

Although the data are clustered within a few per cent of a central value of $r_{\rm in}$, a small ~ 5 per cent increase in $r_{\rm in}$ is observed with increasing $L_{\rm D}$, which is most pronounced for $L_{\rm D}/L_{\rm Edd} > 0.2$. This pattern has been previously observed for other sources (e.g., GRS 1915+105, McClintock et al. 2006; LMC X–3, Steiner et al. 2010).

We tentatively attribute this effect to a thickening of the disc with luminosity and the limitation of our razor-thin disc model.

Table 7.1. Model S Continuum-Fitting Results

N	MJD	$\frac{L_D}{L_{\rm Edd}}$	SMEDGE		SIMPL		KERRBB2		χ^2_ν/DOF	State
			$E_{\rm Edge}$(keV)	$\tau_{\rm max}$	Γ	f_{sc}	a_*	$\dot{M}(10^{18}$g/s)		
1	51117.4	0.172±0.003	8.3 ± 0.1	1.1 ± 0.2	2.06 ± 0.03	0.029 ± 0.002	0.24 ± 0.02	3.30 ± 0.11	0.7/74	TD
2	51119.0	0.155±0.002	8.1 ± 0.1	1.3 ± 0.2	2.11 ± 0.03	0.030 ± 0.002	0.22 ± 0.02	3.01 ± 0.09	0.8/74	TD
3	51121.0	0.136±0.002	8.3 ± 0.1	1.5 ± 0.3	2.15 ± 0.06	0.011 ± 0.001	0.23 ± 0.02	2.62 ± 0.07	0.7/74	TD
4	51124.7	0.115±0.002	8.1 ± 0.1	1.7 ± 0.2	2.15 ± 0.04	0.023 ± 0.001	0.22 ± 0.02	2.25 ± 0.08	0.6/74	TD
5	51128.6	0.101±0.002	7.9 ± 0.1	1.7 ± 0.1	2.17 ± 0.03	0.036 ± 0.001	0.16 ± 0.04	2.04 ± 0.10	1.0/74	TD
6	51130.5	0.094±0.002	8.0 ± 0.1	1.7 ± 0.1	2.17 ± 0.02	0.038 ± 0.001	0.15 ± 0.03	1.92 ± 0.09	1.3/74	TD
7	51132.5	0.086±0.002	7.8 ± 0.1	1.7 ± 0.1	2.16 ± 0.02	0.035 ± 0.001	0.16 ± 0.03	1.75 ± 0.09	0.8/74	TD
8	51134.5	0.080±0.002	7.7 ± 0.1	1.9 ± 0.1	2.28 ± 0.03	0.027 ± 0.001	0.16 ± 0.03	1.63 ± 0.08	0.8/74	TD
9	51136.9	0.072±0.001	7.8 ± 0.1	2.0 ± 0.1	2.16 ± 0.03	0.025 ± 0.001	0.19 ± 0.03	1.42 ± 0.07	0.9/74	TD
10	51145.5	0.053±0.001	7.9 ± 0.1	1.8 ± 0.1	2.05 ± 0.02	0.025 ± 0.001	0.26 ± 0.04	1.01 ± 0.06	0.7/74	TD
11	51150.1	0.059±0.001	7.6 ± 0.1	1.8 ± 0.1	2.08 ± 0.03	0.030 ± 0.001	0.22 ± 0.03	1.15 ± 0.06	0.9/74	TD
12	51152.1	0.069±0.001	7.9 ± 0.1	2.6 ± 0.3	2.13 ± 0.07	0.015 ± 0.001	0.22 ± 0.02	1.33 ± 0.05	0.8/74	TD
13	51152.9	0.066±0.001	8.2 ± 0.1	3.3 ± 0.3	2.20 ± 0.08	0.010 ± 0.001	0.31 ± 0.02	1.21 ± 0.04	0.8/74	TD
14	51154.0	0.082±0.001	7.8 ± 0.2	2.8 ± 0.4	2.39 ± 0.13	0.012 ± 0.002	0.22 ± 0.03	1.60 ± 0.06	0.7/74	TD
15	51155.1	0.092±0.001	8.4 ± 0.2	2.1 ± 0.4	2.43 ± 0.13	0.008 ± 0.001	0.24 ± 0.02	1.75 ± 0.06	0.7/74	TD
16	51157.6	0.122±0.002	8.6 ± 0.4	1.3 ± 0.6	2.75 ± 0.25	0.007 ± 0.002	0.25 ± 0.02	2.33 ± 0.07	0.8/74	TD
17	51160.3	0.165±0.002	7 ± 3	0.1 ± 0.2	1.94 ± 0.27	0.002 ± 0.001	0.25 ± 0.01	3.15 ± 0.07	0.7/74	TD
18	51162.2	0.213±0.002	7.6 ± 0.1	1.4 ± 0.3	3.1 ± 0.7	0.004 ± 0.004	0.17 ± 0.02	4.29 ± 0.10	1.1/74	TD
19	51163.2	0.233±0.003	7.2 ± 0.2	1.6 ± 0.3	3.2 ± 1.3	0.004 ± 0.008	0.15 ± 0.02	4.74 ± 0.13	0.7/74	TD
20	51164.2	0.267±0.002	7.0 ± 0.3	1.3 ± 0.2	2.3 ± 1.1	0.001 ± 0.003	0.12 ± 0.02	5.55 ± 0.11	1.0/74	TD
21	51260.6	0.193±0.003	8.1 ± 0.1	1.1 ± 0.2	2.06 ± 0.04	0.030 ± 0.002	0.21 ± 0.02	3.77 ± 0.12	0.4/66	TD
22	51261.8	0.180±0.003	8.4 ± 0.2	1.0 ± 0.2	2.03 ± 0.03	0.029 ± 0.002	0.23 ± 0.02	3.48 ± 0.11	0.7/66	TD
23	51263.1	0.173±0.003	8.1 ± 0.1	1.4 ± 0.2	2.13 ± 0.03	0.036 ± 0.002	0.16 ± 0.04	3.51 ± 0.16	0.6/66	TD
24	51264.8	0.148±0.002	8.2 ± 0.1	1.6 ± 0.1	2.07 ± 0.03	0.031 ± 0.001	0.21 ± 0.03	2.89 ± 0.10	0.7/66	TD
25	51265.6	0.141±0.003	8.3 ± 0.1	1.4 ± 0.1	2.09 ± 0.03	0.035 ± 0.002	0.22 ± 0.03	2.75 ± 0.10	0.8/66	TD
26	51266.9	0.128±0.002	8.2 ± 0.1	1.6 ± 0.2	2.12 ± 0.03	0.024 ± 0.001	0.23 ± 0.02	2.46 ± 0.09	0.5/66	TD
27	51267.6	0.128±0.003	8.1 ± 0.1	1.8 ± 0.1	2.13 ± 0.02	0.040 ± 0.001	0.18 ± 0.04	2.54 ± 0.12	0.9/66	TD
28	51273.6	0.097±0.002	8.1 ± 0.1	1.8 ± 0.1	2.17 ± 0.02	0.040 ± 0.001	0.15 ± 0.04	1.96 ± 0.10	0.7/66	TD
29	51274.5	0.092±0.002	7.9 ± 0.1	1.9 ± 0.1	2.12 ± 0.03	0.033 ± 0.001	0.14 ± 0.04	1.89 ± 0.10	0.7/66	TD
30	51276.3	0.081±0.002	8.0 ± 0.1	2.6 ± 0.2	2.04 ± 0.05	0.019 ± 0.001	0.18 ± 0.05	1.61 ± 0.10	0.6/66	TD
31	51277.4	0.075±0.002	8.0 ± 0.1	2.2 ± 0.1	2.07 ± 0.03	0.026 ± 0.001	0.20 ± 0.03	1.48 ± 0.08	1.0/66	TD
32	51278.7	0.071±0.002	7.8 ± 0.1	2.0 ± 0.2	2.11 ± 0.04	0.027 ± 0.001	0.17 ± 0.05	1.44 ± 0.10	0.7/66	TD

Table 7.1—Continued

N	MJD	$\frac{L_D}{L_{\rm Edd}}$	SMEDGE		SIMPL		KERRBB2		χ^2_ν/DOF	State
			$E_{\rm Edge}$(keV)	$\tau_{\rm max}$	Γ	f_{sc}	a_*	$\dot{M}(10^{18}$g/s)		
33	51279.6	0.066±0.002	7.9 ± 0.1	2.2 ± 0.1	2.06 ± 0.03	0.023 ± 0.001	0.21 ± 0.03	1.30 ± 0.06	0.8/66	TD
34	51280.6	0.060±0.002	8.1 ± 0.1	2.2 ± 0.2	2.06 ± 0.04	0.021 ± 0.001	0.23 ± 0.03	1.17 ± 0.06	0.7/66	TD
35	51283.2	0.057±0.002	7.4 ± 0.2	1.6 ± 0.2	2.21 ± 0.05	0.027 ± 0.002	0.13 ± 0.06	1.17 ± 0.10	0.6/66	TD
36	51110.3	0.252±0.001	8.3 ± 0.1	1.1 ± 0.1	2.55 ± 0.02	0.223 ± 0.007	0.15 ± 0.05	5.13 ± 0.25	0.8/74	INT
37	51111.6	0.234±0.003	8.1 ± 0.1	1.1 ± 0.1	2.50 ± 0.02	0.240 ± 0.009	0.14 ± 0.06	4.79 ± 0.27	0.8/74	INT
38	51112.8	0.224±0.001	8.1 ± 0.1	1.2 ± 0.1	2.51 ± 0.02	0.249 ± 0.008	0.10 ± 0.06	4.70 ± 0.29	0.8/74	INT
39	51113.7	0.206±0.003	8.3 ± 0.1	1.2 ± 0.1	2.49 ± 0.02	0.208 ± 0.008	0.21 ± 0.04	4.03 ± 0.20	1.0/74	INT
40	51115.3	0.172±0.002	8.4 ± 0.1	1.3 ± 0.1	2.42 ± 0.02	0.153 ± 0.005	0.30 ± 0.03	3.14 ± 0.14	0.8/74	SPL
41	51126.6	0.110±0.002	8.2 ± 0.1	1.7 ± 0.1	2.29 ± 0.02	0.059 ± 0.001	0.17 ± 0.04	2.21 ± 0.11	1.0/74	INT
42	51140.0	0.056±0.001	8.0 ± 0.1	1.8 ± 0.1	2.17 ± 0.02	0.086 ± 0.002	0.32 ± 0.04	1.01 ± 0.07	1.0/74	INT
43	51140.7	0.055±0.001	8.1 ± 0.1	1.8 ± 0.1	2.19 ± 0.02	0.078 ± 0.002	0.31 ± 0.04	1.00 ± 0.07	1.1/74	INT
44	51143.8	0.052±0.001	8.0 ± 0.1	1.7 ± 0.1	2.21 ± 0.02	0.081 ± 0.003	0.28 ± 0.07	0.98 ± 0.10	0.8/74	INT
45	51269.7	0.117±0.002	8.2 ± 0.1	1.8 ± 0.1	2.25 ± 0.02	0.052 ± 0.001	0.17 ± 0.04	2.34 ± 0.13	1.0/66	SPL
46	51270.8	0.092±0.002	8.3 ± 0.1	1.6 ± 0.1	2.28 ± 0.01	0.110 ± 0.002	0.31 ± 0.03	1.68 ± 0.09	1.0/66	SPL
47	51271.4	0.086±0.002	8.3 ± 0.1	1.5 ± 0.1	2.30 ± 0.02	0.120 ± 0.003	0.32 ± 0.04	1.57 ± 0.09	0.9/66	SPL
48	51664.4	0.148±0.004	8.2 ± 0.1	1.5 ± 0.1	2.45 ± 0.02	0.165 ± 0.005	0.31 ± 0.04	2.70 ± 0.15	0.8/66	SPL
49	51664.7	0.145±0.004	8.4 ± 0.1	1.4 ± 0.1	2.42 ± 0.02	0.173 ± 0.005	0.35 ± 0.04	2.56 ± 0.15	0.9/66	SPL
50	51665.4	0.135±0.003	8.1 ± 0.1	1.5 ± 0.1	2.42 ± 0.02	0.145 ± 0.004	0.29 ± 0.05	2.50 ± 0.16	0.8/66	SPL
51	51667.7	0.119±0.003	8.2 ± 0.1	1.5 ± 0.1	2.36 ± 0.02	0.126 ± 0.003	0.33 ± 0.03	2.15 ± 0.11	0.7/66	SPL
52	51668.8	0.115±0.003	8.2 ± 0.1	1.5 ± 0.1	2.34 ± 0.02	0.117 ± 0.003	0.32 ± 0.03	2.08 ± 0.10	1.0/66	SPL
53	51669.2	0.123±0.003	8.1 ± 0.1	1.6 ± 0.1	2.38 ± 0.02	0.109 ± 0.003	0.23 ± 0.04	2.38 ± 0.13	1.1/66	SPL
54	51670.6	0.102±0.003	8.1 ± 0.1	1.6 ± 0.1	2.35 ± 0.02	0.143 ± 0.003	0.32 ± 0.04	1.85 ± 0.11	0.8/66	SPL
55	51670.8	0.107±0.003	8.3 ± 0.1	1.6 ± 0.1	2.33 ± 0.02	0.113 ± 0.003	0.31 ± 0.03	1.95 ± 0.10	0.8/66	INT
56	51671.4	0.111±0.003	8.0 ± 0.1	1.7 ± 0.1	2.35 ± 0.02	0.108 ± 0.003	0.23 ± 0.04	2.14 ± 0.13	1.1/66	SPL
57	51672.4	0.096±0.003	8.2 ± 0.1	1.7 ± 0.1	2.31 ± 0.02	0.121 ± 0.003	0.32 ± 0.04	1.75 ± 0.10	0.8/66	SPL
58	51673.0	0.097±0.004	8.2 ± 0.1	1.5 ± 0.1	2.39 ± 0.01	0.205 ± 0.005	0.35 ± 0.06	1.71 ± 0.14	0.7/66	INT
59	51673.4	0.099±0.004	8.1 ± 0.1	1.6 ± 0.1	2.42 ± 0.01	0.196 ± 0.004	0.28 ± 0.07	1.84 ± 0.17	0.8/66	INT
60	51674.7	0.085±0.004	8.1 ± 0.1	1.4 ± 0.1	2.31 ± 0.02	0.224 ± 0.006	0.37 ± 0.08	1.48 ± 0.16	0.6/66	INT

Note. —
1. Reported error estimates are symmetric 1σ statistical uncertainties.
2. M, i, and D are frozen at their fiducial values.

7.4 Continuum Fitting: Towards a Self-Consistent Disc + Reflection Model

In the previous section, we used the empirical model SMEDGE to crudely account for a prominent spectral feature in the reflection component, namely, the broad K-edge of iron. We now consider a more physically-motivated treatment of the full reflection spectrum, which is generated by that portion of the power-law flux that strikes the accretion disc (Ross & Fabian 1993). To this end, we first consider a generalised version of SIMPL that is more appropriate to the problem at hand. We then examine two reflection models, IREFLECT, and REFLIONX, concluding that the former model is better for CF fitting, while the latter model is better for fitting the profile of the Fe $K\alpha$ line (which is considered in Section 7.6). As we describe below, there is presently no unified reflection model that is well-suited to both approaches of measuring spin.

7.4.1 A Variant of the Power-Law Model SIMPL

As in Section 7.3, the core of our Comptonised-disc model consists of KERRBB2 and SIMPL. However, we now introduce a modified version of SIMPL that is appropriate when including a separate and additive reflection component. This model, SIMPL-R, is a generalisation of SIMPL that covers the two limiting cases described by equations 1 & 2 in Steiner et al. (2009b), and applies to intermediate cases as well:

$$n_{\rm out}(E)dE = (1 - f_{\rm SC})n_{\rm in}(E)dE + (f_{\rm SC}/x)\left[\int_{E_{\rm min}}^{E_{\rm max}} n_{\rm in}(E_0)G(E;E_0)dE_0\right]dE. \quad (7.1)$$

Here, $n_{\rm in}(E)$ and $n_{\rm out}(E)$ are the seed input and model output photon number densities at energy (E). The normalisation constant $f_{\rm SC}$ is again the fraction of photons directed into a power law with photon index Γ, and $G(E;E_0)$ is the distribution function of the output power law (see Steiner et al. 2009b; Ebisawa 1999). The one new parameter is x, which determines the fraction of the power-law photons that strike the disc. *These are the photons which will be considered in modeling the reflection component.*

The standard version of SIMPL, which was used in the preceding section, assumes either that none of the Compton-scattered photons strike the disc, or adopting an equivalent interpretation, that reflection acts like a perfect mirror with no absorption. This corresponds to the limiting case $x = 1$, which is described by Equation 1 in Steiner et al. (2009b). In the opposite limit, $x = 2$, half of the scattered photons are redirected downward, illuminating the disc, while failing to reach an observer at infinity, As they encounter the disc atmosphere, the returning photons are absorbed and reprocessed, thereby generating the reflection component. This limit corresponds to Equation 2 in Steiner et al. (2009b).

The variant SIMPL-R (Eq. 7.1) generalises this dichotomy, making it possible to treat separately the reprocessed emission coming from the illuminated disc via the tunable parameter x. This allows one to model a corona quite generally. The quantity $x - 1$ describes the solid angle subtended by the disc from the perspective

of the corona in units of 2π, which we refer to as a covering factor. In this chapter, we assume that the geometry of the corona is a disc-hugging slab with a covering factor of unity ($x = 2$); thus, half the photons escape the system and half strike the disc. As shorthand, we will refer to the portion of the Compton component produced by SIMPL-R which irradiates the disc as SIMPLC (i.e., the second term on the right-hand side of Eq. 7.1 multiplied by the covering factor).

7.4.2 Results II: Continuum Fitting using IREFLECT and REFLIONX

We first consider the model IREFLECT (Magdziarz & Zdziarski 1995), which computes the reflected spectrum (including scattering and edge absorption, but excluding line fluorescence) generated in an ionised disc atmosphere that is illuminated by an arbitrary external spectrum. We convolve the disc-illuminating component SIMPLC with IREFLECT and isolate the reflected component by setting the parameter *rel_refl* to -1. (Our model implicitly assumes that the observed and illuminating power-law spectra are identical.) The ionisation parameter $\xi \equiv L/nR^2$ is initially set to 10^4 and allowed to vary freely from $10^1 - 10^5$, while the characteristic disc temperature is fixed to $T_{\rm disc} = 5 \times 10^6$ K and the metallicity is assumed to be solar. Fe $K\alpha$ emission is included separately in an approximate fashion as an intrinsically narrow Gaussian line centred at a restframe energy of 6.5 keV. This composite reflection component is then convolved with the relativistic smearing kernel KERRCONV (Brenneman & Reynolds 2006) with the radial emissivity index q fixed at the best-fitting *RXTE* value $q = 2.5$ (see Section 7.6). The complete

model, which is comprised of an accretion-disc and a power-law component, is: CRABCOR×TBABS(SIMPL-R⊗KERRBB2 + KERRCONV⊗(IREFLECT⊗SIMPLC + GAUSS)).

The primary limitation of this model (referred to hereafter as Model I) is that although edges are included, the fluorescent line features (e.g., García & Kallman 2010), apart from Fe $K\alpha$, are missing. Also, the strength of the Fe $K\alpha$ feature should be tied to the depth of the corresponding edge feature, but here that is not possible. Below and in Section 7.5, we will demonstrate that these shortcomings of Model I have little effect on the CF spin results because for our primary *gold* spectra the reflected component is faint compared to the dominant thermal component. However, these issues are of critical importance in estimating spin via the Fe $K\alpha$ line (Section 7.6).

We now consider a second reflection model, REFLIONX (Ross & Fabian 2005), which we use as a replacement for (IREFLECT⊗SIMPLC+GAUSS) in Model I given above. We will refer to the new composite model as Model R. In REFLIONX, reflection is produced by a power-law spectrum illuminating a cold slab of constant density. The virtue of this model is that it properly couples line emission to absorption, and it also describes the full Fe K emission-line complex. A major drawback is that it is optimized for modeling AGN, which have cold discs of lower density. Consequently, in estimating spin via the Fe $K\alpha$ method (Section 7.6), we use a high-density variant of REFLIONX, REFBHB, which includes an intrinsic blackbody component (Ross & Fabian 2007). Because the blackbody component is hardwired into REFBHB, it can not presently be used with CF models. We therefore use REFLIONX in concert with KERRBB2 for our CF analysis.

In addition to the temperature/density limitations of REFLIONX just mentioned, this model has additional shortcomings. Of primary importance, it requires that the illuminating spectrum have a simple power law form. This power law is not truncated at low energies and its flux can rival or exceed the thermal flux, thereby leading to unphysical results (see e.g., Steiner et al. 2009b). In addition, the strength of the reflected component is not linked to the normalisation of the illuminating spectrum, and so there is no way to ensure that the Compton and reflection components are appropriately matched. Nevertheless, we employ Model R using REFLIONX as a second-tier CF model that gives us an independent check on the results obtained using Model I.

In summary, using a variant of SIMPL and considering two reflection models, we have progressed toward a model featuring a self-consistent treatment of thermal disc emission, Compton scattering, and disc reflection. For estimating spin via the CF method, we favor IREFLECT, while for the Fe $K\alpha$ method we elect to use REFLIONX and REFBHB (Section 7.6).

We now apply Model I (Section 7.4.2) to our set of *RXTE* spectra, while following the procedures described in Section 7.3.2. In this case, we find that only a total of 45 spectra (24 *gold* and 21 *silver*) meet our selection criteria (Section 7.3.1), compared to the 60 selected using Model S. Our fitting results for these 45 spectra are given in Table 7.2.

For the *gold* spectra, we find excellent agreement between the results obtained using Model I, $a_* = 0.23 \pm 0.06$, and Model S, $a_* = 0.20 \pm 0.04$. This agreement is illustrated in Fig. 7.3, where we also show results for Model R. As is apparent,

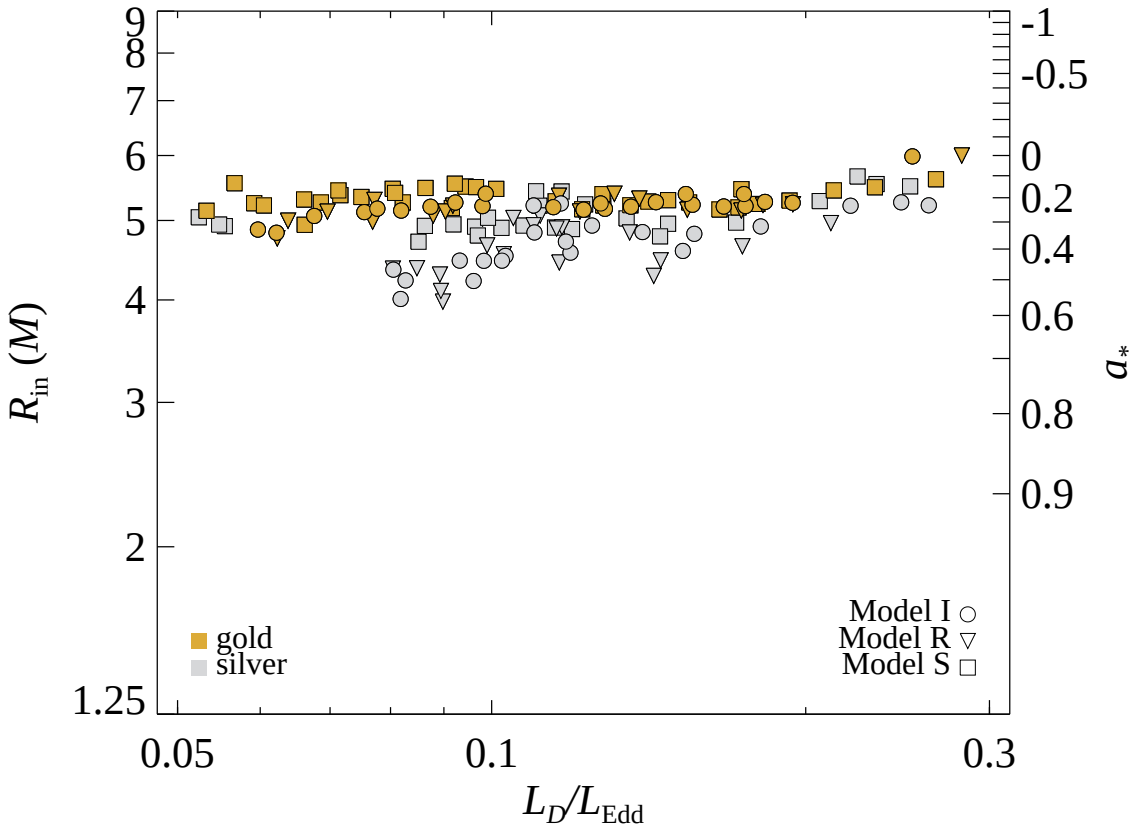

Figure 7.3.— As in Fig. 7.2, we again plot $R_{\rm in}$ and a_* versus luminosity, but we now show results for all three of the models discussed in the text. The data for Model S, which are repeated from Fig. 7.2, show the highest degree of internal consistency.

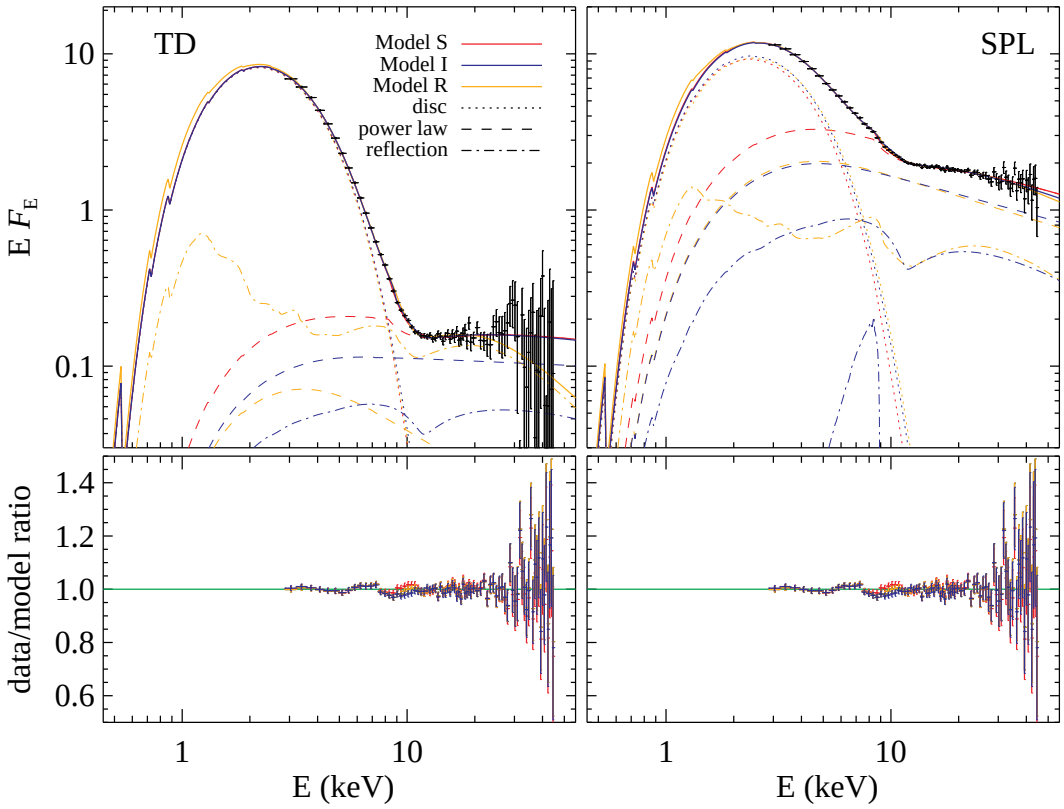

Figure 7.4.— Model fits for a *gold* spectrum (*left*) and a *silver* spectrum (*right*), which correspond respectively to observations made on MJD 51121.0 and MJD 51115.3 (see Tabs. 7.1 & 7.2). The models are differentiated by line colour and the individual components by line texture. Note how much weaker the power-law component is for the *gold* spectrum, and how closely all three models track the data.

considering only the *gold* spectra, all three models are in excellent agreement – the mean values of $r_{\rm in}$ are consistent with one another to within ≈ 2 per cent. However, for the *silver* spectra the mean values of $r_{\rm in}$ are depressed for all three models, by ≈ 10 per cent for the self-consistent reflection models (which track each other closely) and by only ≈ 5 per cent for Model S. Interestingly, the primitive Model S performs better than the self-consistent reflection models by harmonizing the results obtained from the two data sets and delivering the highest degree of internal consistency. Fig. 7.4 shows an overlay comparison of the best-fitting results using the three models for two representative spectra, one *gold* and the other *silver*. The total unfolded spectra and their components are plotted, as well as the data/model ratio. The key result of this section is that using our fiducial values of M, i and D (Section 7.1), all three models applied to the *gold* spectra give the same low estimate of spin: $0.15 < a_* < 0.35$.

7.5 Continuum Fitting: Error Analysis and Final Spin Result

In this section, we broadly consider three sources of observational error, both systematic and statistical, which bear on our final estimate of the spin. In order of increasing importance, these are (1) sensitivity to the details of the spectral models employed; (2) X-ray flux calibration uncertainties; and (3) the uncertainties in the input parameters M, i and D. We then perform a comprehensive analysis that incorporates these uncertainties and arrive at our final CF estimate of the spin of the

black hole. In the following, we present an overview; for details, see Appendix 7.9.

- *Sensitivity to X-ray spectral models.* In order to make this assessment, we determine the change in $r_{\rm in}$ when varying a single model component or parameter setting. Table 7.3 gives the mean fractional change in $r_{\rm in}$ for the *gold* data sample that arises from changing either a model parameter (rows P1-12) or model component (M1-5). The 'Change' column describes the alteration made to a parameter or model component relative to its nominal condition (where DISC, PL, and REFL refer to the accretion disc, power law, and reflection components). The third and fourth columns respectively list the fractional changes in $r_{\rm in}$ for Model I and Model S. As Table 7.3 demonstrates, the largest model uncertainty arises from the choice of viscosity parameter: Using $\alpha = 0.01$ instead of the default value ($\alpha = 0.1$) decreases $r_{\rm in}$ by ≈ 4 per cent for Model I and 3 per cent for Model S. Each of the other 16 changes considered affect $r_{\rm in}$ by < 3 per cent.

Table 7.2. Model I Continuum-Fitting Results

N	MJD	$\frac{L_D}{L_{\rm Edd}}$	SIMPL-R		KERRBB2		IREFLECT	GAUSS	χ^2_ν/DOF	State
			Γ	f_{sc}	a_*	$\dot{M}(10^{18}$g/s)	ξ(erg cm/s)	N(ph./cm^2/s)		
1	51117.4	0.175±0.002	2.04 ± 0.04	0.018 ± 0.002	0.24 ± 0.02	3.37 ± 0.11	1500 ± 1600	2.8 ± 2.7	0.7/74	TD
2	51119.0	0.156±0.002	2.07 ± 0.04	0.017 ± 0.002	0.23 ± 0.02	3.01 ± 0.09	1200 ± 1300	2.7 ± 2.0	0.7/74	TD
3	51121.0	0.136±0.002	2.06 ± 0.06	0.006 ± 0.001	0.24 ± 0.02	2.61 ± 0.07	2000 ± 3000	1.4 ± 1.1	0.7/74	TD
4	51124.7	0.115±0.002	2.07 ± 0.06	0.012 ± 0.002	0.24 ± 0.02	2.20 ± 0.07	1200 ± 2200	2.5 ± 1.5	0.6/74	TD
5	51128.6	0.098±0.001	2.09 ± 0.05	0.020 ± 0.003	0.24 ± 0.02	1.89 ± 0.07	1100 ± 1800	2.9 ± 1.5	0.9/74	TD
6	51130.5	0.092±0.001	2.15 ± 0.03	0.023 ± 0.001	0.22 ± 0.02	1.79 ± 0.05	310 ± 100	2.9 ± 0.9	1.1/74	TD
7	51132.5	0.082±0.001	2.07 ± 0.03	0.018 ± 0.001	0.25 ± 0.03	1.55 ± 0.07	1900 ± 1900	2.9 ± 1.2	0.8/74	TD
8	51134.5	0.075±0.001	2.15 ± 0.04	0.013 ± 0.001	0.26 ± 0.03	1.43 ± 0.06	1900 ± 2200	1.9 ± 0.8	0.8/74	TD
9	51136.9	0.068±0.001	2.08 ± 0.21	0.013 ± 0.008	0.28 ± 0.03	1.26 ± 0.07	700 ± 5000	2.0 ± 1.0	0.9/74	TD
10	51157.6	0.122±0.001	2.6 ± 0.7	0.004 ± 0.007	0.25 ± 0.02	2.33 ± 0.08	600 ± 10000	0.5 ± 0.8	0.8/74	TD
11	51160.3	0.167±0.001	1.97 ± 0.32	0.001 ± 0.001	0.24 ± 0.02	3.21 ± 0.08	50000 ± 700000	0.0 ± 1.5	0.7/74	TD
12	51163.2	0.253±0.004	2.7 ± 1.3	0.001 ± 0.003	0.00 ± 0.03	5.62 ± 0.17	10 ± 4000	3.4 ± 3.0	1.7/74	TD
13	51260.6	0.194±0.002	1.97 ± 0.04	0.015 ± 0.001	0.22 ± 0.02	3.77 ± 0.11	6000 ± 5000	4.5 ± 3.0	0.4/66	TD
14	51261.8	0.183±0.003	2.04 ± 0.04	0.018 ± 0.002	0.22 ± 0.02	3.56 ± 0.12	1500 ± 1600	2.4 ± 2.9	0.7/66	TD
15	51263.1	0.174±0.002	2.07 ± 0.04	0.020 ± 0.002	0.18 ± 0.03	3.48 ± 0.15	1900 ± 1800	4.7 ± 3.0	0.5/66	TD
16	51264.8	0.153±0.002	1.97 ± 0.03	0.014 ± 0.001	0.18 ± 0.03	3.06 ± 0.12	6000 ± 4000	7.2 ± 1.9	0.8/66	TD
17	51265.6	0.144±0.002	2.10 ± 0.08	0.022 ± 0.004	0.22 ± 0.02	2.79 ± 0.09	500 ± 1000	3.3 ± 1.5	0.7/66	TD
18	51266.9	0.128±0.002	2.08 ± 0.23	0.014 ± 0.008	0.25 ± 0.03	2.45 ± 0.12	700 ± 5000	2.6 ± 2.0	0.5/66	TD
19	51267.6	0.127±0.002	2.08 ± 0.17	0.022 ± 0.009	0.22 ± 0.03	2.47 ± 0.13	700 ± 4000	4.9 ± 2.6	0.8/66	TD
20	51273.6	0.099±0.003	1.95 ± 0.03	0.015 ± 0.001	0.18 ± 0.04	1.97 ± 0.10	10000 ± 9000	8.1 ± 1.4	1.9/66	TD
21	51274.5	0.087±0.001	2.04 ± 0.10	0.018 ± 0.005	0.24 ± 0.03	1.68 ± 0.08	800 ± 3000	3.1 ± 1.6	0.8/66	TD
22	51276.3	0.078±0.002	1.99 ± 0.19	0.010 ± 0.004	0.25 ± 0.03	1.48 ± 0.07	500 ± 3000	2.6 ± 0.7	0.7/66	TD
23	51278.7	0.062±0.002	1.92 ± 0.06	0.011 ± 0.001	0.34 ± 0.03	1.11 ± 0.06	20000 ± 50000	3.6 ± 1.2	0.8/66	TD
24	51279.6	0.060±0.001	1.99 ± 0.31	0.013 ± 0.011	0.33 ± 0.02	1.07 ± 0.05	700 ± 7000	2.1 ± 1.1	0.8/66	TD
25	51110.3	0.262±0.001	2.45 ± 0.02	0.109 ± 0.005	0.23 ± 0.03	5.06 ± 0.20	4879 ± 2000	17 ± 9	0.8/74	INT
26	51111.6	0.247±0.001	2.39 ± 0.03	0.113 ± 0.006	0.22 ± 0.04	4.80 ± 0.23	7147 ± 4000	24 ± 11	0.7/74	INT
27	51113.7	0.221±0.002	2.43 ± 0.03	0.108 ± 0.007	0.23 ± 0.04	4.25 ± 0.24	2331 ± 1500	17 ± 9	0.9/74	INT
28	51115.3	0.181±0.003	2.39 ± 0.07	0.086 ± 0.011	0.32 ± 0.04	3.28 ± 0.26	875.9 ± 1700	9 ± 7	0.7/74	SPL
29	51126.6	0.110±0.001	2.14 ± 0.03	0.025 ± 0.001	0.23 ± 0.02	2.11 ± 0.08	10000 ± 7000	8.8 ± 1.7	1.5/74	INT
30	51269.7	0.117±0.002	2.10 ± 0.03	0.022 ± 0.001	0.22 ± 0.02	2.26 ± 0.08	10000 ± 8000	9.1 ± 1.9	1.4/66	SPL
31	51270.8	0.083±0.001	2.17 ± 0.03	0.053 ± 0.003	0.50 ± 0.02	1.28 ± 0.06	10000 ± 7000	10.2 ± 2.5	1.6/66	SPL
32	51271.4	0.081±0.001	2.20 ± 0.03	0.059 ± 0.003	0.47 ± 0.04	1.29 ± 0.10	10000 ± 7000	10 ± 3	1.2/66	SPL

Table 7.2—Continued

N	MJD	$\frac{L_D}{L_{\rm Edd}}$	SIMPL-R		KERRBB2		IREFLECT	GAUSS	χ^2_ν/DOF	State
			Γ	f_{sc}	a_*	$\dot{M}(10^{18}$g/s)	ξ(erg cm/s)	N(ph./cm^2/s)		
33	51664.4	0.156±0.003	2.40 ± 0.04	0.090 ± 0.005	0.35 ± 0.03	2.78 ± 0.12	500 ± 600	10 ± 4	0.6/66	SPL
34	51664.7	0.152±0.002	2.40 ± 0.05	0.097 ± 0.007	0.41 ± 0.02	2.58 ± 0.13	500 ± 800	10 ± 4	0.9/66	SPL
35	51665.4	0.140±0.001	2.37 ± 0.13	0.079 ± 0.019	0.34 ± 0.05	2.49 ± 0.31	700 ± 3000	7 ± 6	0.6/66	SPL
36	51667.7	0.119±0.002	2.29 ± 0.03	0.067 ± 0.005	0.41 ± 0.03	2.00 ± 0.11	1500 ± 1300	8 ± 4	0.7/66	SPL
37	51668.8	0.118±0.001	2.32 ± 0.04	0.068 ± 0.005	0.37 ± 0.03	2.04 ± 0.11	500 ± 600	6.2 ± 2.1	0.8/66	SPL
38	51669.2	0.125±0.003	2.35 ± 0.02	0.063 ± 0.002	0.31 ± 0.02	2.27 ± 0.08	230 ± 90	7.6 ± 2.5	0.9/66	SPL
39	51670.6	0.103±0.002	2.30 ± 0.03	0.079 ± 0.004	0.42 ± 0.02	1.72 ± 0.07	500 ± 400	8.0 ± 2.3	0.7/66	SPL
40	51670.8	0.102±0.002	2.25 ± 0.03	0.060 ± 0.004	0.44 ± 0.03	1.68 ± 0.09	1700 ± 1300	7 ± 3	0.7/66	INT
41	51671.4	0.110±0.002	2.29 ± 0.13	0.058 ± 0.016	0.34 ± 0.04	1.96 ± 0.17	600 ± 2700	7.3 ± 2.5	0.9/66	SPL
42	51672.4	0.093±0.001	2.25 ± 0.10	0.067 ± 0.014	0.44 ± 0.04	1.53 ± 0.15	800 ± 2700	7 ± 4	0.7/66	SPL
43	51673.0	0.096±0.001	2.33 ± 0.07	0.109 ± 0.013	0.50 ± 0.05	1.49 ± 0.16	900 ± 1900	10 ± 6	0.6/66	INT
44	51673.4	0.098±0.002	2.36 ± 0.09	0.103 ± 0.017	0.44 ± 0.06	1.61 ± 0.23	900 ± 2500	10 ± 6	0.8/66	INT
45	51674.7	0.082±0.001	2.22 ± 0.03	0.113 ± 0.006	0.56 ± 0.05	1.20 ± 0.11	2600 ± 1800	11 ± 6	0.6/66	INT

- *Flux calibration.* The problem of flux calibration is endemic to X-ray astronomy. The Crab spectrum, as determined by Toor & Seward (1974), is the widely-adopted standard that we have consistently used in our work. Uncertainties in the normalisation of this spectrum have recently been considered by Weisskopf et al. (2010). Using their fig. 1 as a guide, we adopt a generous ±10 per cent uncertainty in our overall flux calibration, which corresponds to a 5 per cent uncertainty in $r_{\rm in}$.

- *Uncertainties in M, i and D.* As in our earlier work (e.g., Liu et al. 2008; Gou et al. 2009, 2010), we sample the allowed parameter space assuming Gaussian errors (except here for D, we use an asymmetric Gaussian). The sampling is performed using 42,500 triplets of M, i, and D, which are distributed in a uniform grid throughout the parameter space. At each point in the grid, the complete *RXTE* data set is analysed with Model S, and the selection criteria given in Section 7.3 are separately applied to the results. Folding all of the runs together, a composite distribution based on all of the selected spectra is obtained, where we have additionally weighted over the set of possible dynamical models (see table 1 in Orosz et al. 2011).

  In conducting this analysis, we have included the robust no-eclipse constraint, $i < 82°$. We have further required that during the TD-state plateau phase (days 105–182; Fig. 7.1) the disc luminosity not exceed 85 per cent of $L_{\rm Edd}$ (the actual Eddington limit for disc geometry; see section 6.1 in McClintock et al. 2006). Lastly, we also require that the disc luminosity during the thermal plateau phase be greater than 10 per cent of $L_{\rm Edd}$, or else the full sample of TD data would extend downward in luminosity to the implausibly low value of

$\lesssim 0.1$ per cent $L_{\rm Edd}$.

In the analysis described above, we have used the default value of the viscosity parameter, $\alpha = 0.1$. Because α is the major source of uncertainty considered in Table 7.3, we have repeated the analysis just described using $\alpha = 0.01$ and combined the two distributions, weighting them equally. We combine all other errors in Table 7.3, yielding an ensemble value of ≈ 4.2 per cent. Finally, we add in quadrature the 5 per cent error in the absolute flux calibration and arrive at our net error of 6.5 per cent. The effect of this uncertainty on our measurement of spin is incorporated by running a boxcar smoothing kernel (with a 13 per cent full width) over the distribution for $r_{\rm in}$.

The dominant source of error in our final determination of the spin is the combined observational uncertainty in M, i and D, which in turn is largely a result of the uncertainties associated with modeling the optical/NIR light curves (Orosz et al. 2011). Fig. 7.5 shows the dependence of $r_{\rm in}$/spin on these model parameters. Here, using the results of the grid analysis described above, we vary one of the three parameters, fixing the other two at the their best values. The strong correlations between spin and inclination, and between spin and distance, demonstrate the degree to which measurement errors in these quantities contribute to the uncertainty in spin. Together, errors in M, i, and D account for $\Delta a_* \approx 0.25$ ($\Delta r_{\rm in}/r_{\rm in} \approx 0.2$) at 90 per cent confidence. The contribution due to the inclination is sizable, ~ 11 per cent for $r_{\rm in}$, because its value is both large (74.7°) and uncertain (3.8°). The contribution due to the distance is also ~ 11 per cent, while that due to the mass is only ~ 7 per cent.

Table 7.3. Systematic Changes to the Model

TD	Change	$\Delta\bar{r}_{\rm in}(\%)$	
		Model I	Model S
P1	$\alpha = 0.01$	-3.68	-2.90
P2	$N_{\rm H} = 6 \times 10^{21}\,{\rm cm}^{-2}$	-2.90	-1.94
P3	$N_{\rm H} = 10 \times 10^{21}\,{\rm cm}^{-2}$	0.84	2.84
P4	$x = 1.5$	-1.13	···
P5	$x = 1.1$	-1.26	···
P6	q and x free	0.21	···
P7	$q = 3$	-2.88	···
P8	$T_{\rm disc} = 10^6$ K	-0.09	···
P9	$T_{\rm disc} = 10^7$ K	0.17	···
P10	$E_{\rm line} = 6.8$ keV	-1.86	···
P11	$W_{\rm Edge} = 3.5$ keV	···	-0.42
P12	$W_{\rm Edge} = 14$ keV	···	0.41
M1	DISC: BHSPEC	1.30	2.88
M2	PL: falloff with kT_e	-1.53	-0.66
M3	PL: down-scattering set	-0.27	0.07
M4	REFL: SMEDGE	1.70	···
M5	REFL: REFLIONX	-1.00	-2.65

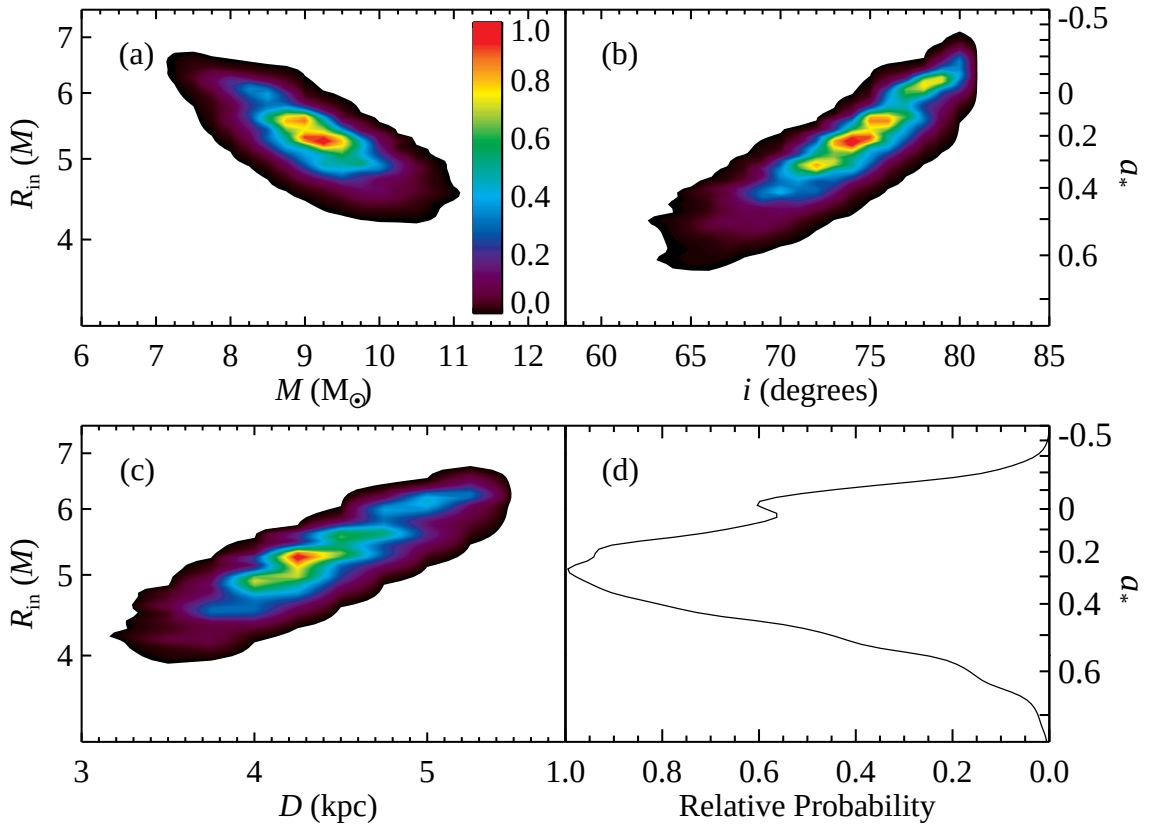

Figure 7.5.— Probability contours for the relationship between $r_{\rm in}$/spin and M, i, and D. Each of the first three panels (*a-c*) shows variation for a single parameter; the other two parameters have been fixed at their best values. The orientations of the probability ellipsoids show that spin is positively correlated with M and negatively correlated with both i and D. In panel (*d*), a combined probability distribution for the case $\alpha = 0.1$ is shown (arbitrarily scaled) with variation in M, i, and D folded together.

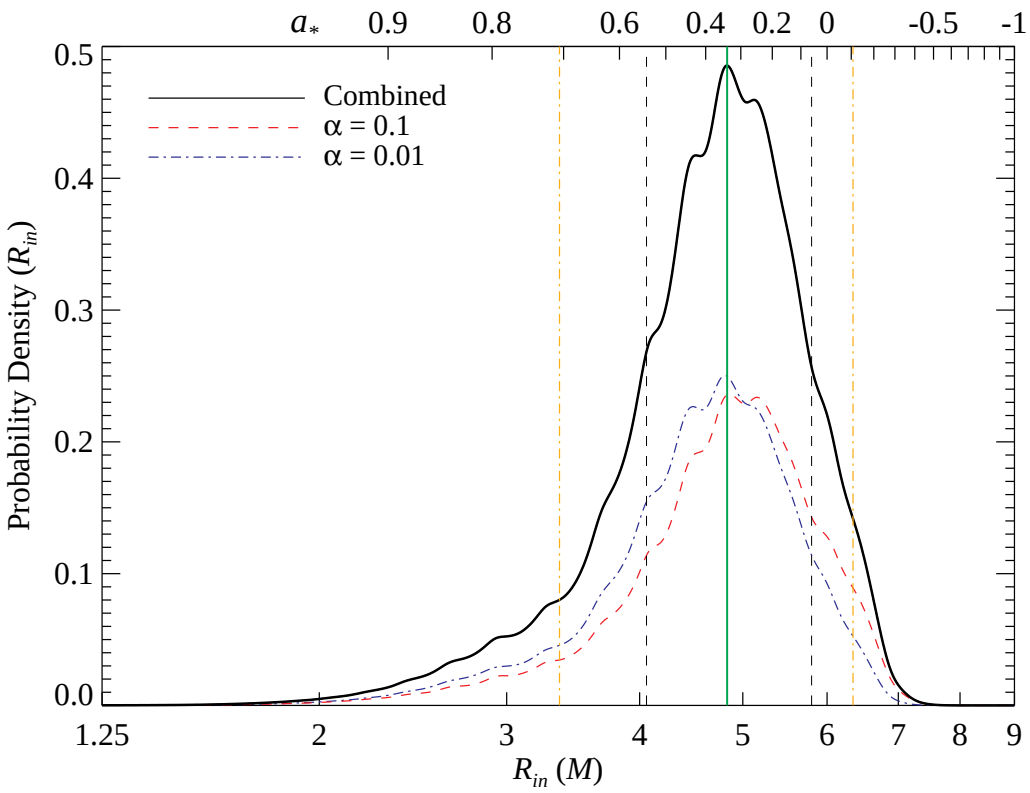

Figure 7.6.— Composite probability density for $R_{\rm in}$ and a_* which takes into account both systematic and statistical errors including: uncertainties in distance, black-hole mass and inclination; the spectral model; and the uncertainty in the absolute flux calibration. The net probability distribution is a combination of the individual distributions for two values of α. The contribution from each integrates to 50 per cent probability and is shown for $\alpha = 0.01$ (blue dash-dotted line) and $\alpha = 0.1$ (red dashed line). The 90 per cent confidence limits for the combined distribution are shown as yellow vertical lines, the 1σ limits as vertical black lines, and the most probable spin is marked with a green line. We conclude that the spin is moderate: $-0.11 < a_* < 0.71$ (90 per cent confidence).

After folding together all sources of error, the resulting probability distribution is shown in Fig. 7.6, with $R_{\rm in}$ and a_* displayed respectively on the bottom and top axes. The green vertical line identifies the most probable spin, $a_* = 0.34$, and the yellow lines indicate the 90 per cent confidence interval, which extends from -0.11 to 0.71. From an inspection of this distribution function, we conclude that the black hole is unlikely to be in a retrograde configuration (only ~ 11.2 per cent probability). Of greater importance, we conclude that *the spin is not high*. For example, the probability that the CF spin exceeds 0.9 is less than 0.4 per cent, a surprising result for a black hole that has produced superluminal jets.

7.6 Spin from Reflection Features

In the previous section, we concluded that the spin parameter has a low or intermediate value. This result is based on our CF analysis of many *RXTE* spectra, which were obtained primarily in the TD state. In what follows, we first analyse reflection features in intermediate-state spectra of J1550 obtained with the *ASCA* X-ray observatory; we then supplement this analysis using a sample of *RXTE* spectra, also obtained in the intermediate state. We fit the *ASCA* GIS-2 and GIS-3 data simultaneously, using a floating normalisation constant to allow for cross-calibration uncertainties. Our work differs from earlier analyses of these same data by others (e.g., see Miller et al. 2005; Gierliński & Done 2003; Miller et al. 2009b): Our focus is on a detailed analysis of the reflection component, rather than on a precise model of the overall continuum. We begin by setting all the physical parameters of the binary to the best-estimate values presented in Orosz et al. (2011).

In addition to the soft disc and hard power-law components seen in the TD- and intermediate-state spectra of black-hole binaries, a broad emission line at ~ 6.4 keV is also often present (see e.g. Miller 2007). This line feature is merely the most prominent reflection signature that arises as hard emission from the corona irradiates the cooler disc (Ross & Fabian 2005). In the vicinity of a black hole, the iron-$K\alpha$ line shape and other reflection features are distorted by various relativistic effects (Fabian et al. 1989; Laor 1991). The spin parameter can be constrained by modeling these features because their shape depends on how far the disc extends down into the gravitational potential well (see Section 7.1), the key assumption again being that this extent is set by the radius of the ISCO.

7.6.1 Phenomenological Models – *ASCA*

In order to highlight the relativistic nature of the line profile in the *ASCA* spectra, we start by modeling the 1–4 keV and 7–10 keV continua with a combination of a disc blackbody (described by the XSPEC model DISKBB[3] of Mitsuda et al. 1984) and the Comptonisation model SIMPL. The neutral hydrogen column was initially fixed at $N_{\rm H} = 8 \times 10^{21}\,{\rm cm}^{-2}$ as per Miller et al. (2003), which resulted in a poor fit to the continuum with $\chi^2/\nu = 2172.3/1002$. Allowing the column density to vary resulted in a significant improvement to the fit with $\chi^2/\nu = 1367.5/1001$ for $N_{\rm H} = 5.4 \pm 0.1 \times 10^{21}\,{\rm cm}^{-2}$. The total neutral hydrogen column density in the line

[3]This model characterises the thermal emission using only two parameters – the flux normalisation and a colour temperature. Here, we use this very approximate model of the continuum (compare Section 7.3) because of its simplicity in *phenomenologically* describing the thermal continuum.

of sight to J1550, which was determined using the *Chandra* transmission grating, is not expected to vary (Miller, Cackett, & Reis 2009a). However, the differing values of $N_{\rm H}$ can be reasonably attributed to differences in the calibrations of the *Chandra* and *ASCA* detectors. Furthermore, allowing $N_{\rm H}$ to differ between the two GIS spectra further improves the fit: $\Delta\chi^2 = -47.5$ for one less degree of freedom with a difference in $N_{\rm H}$ of < 5 per cent. Fig. 7.7 shows the line spectrum obtained by modeling the continuum as described above. The asymmetric and broad residual feature in the 4–7 keV band has the appearance one expects for fluorescent disc-line emission arising near a black hole.

We provide a physical description of the Fe line by first modeling the residuals seen in Fig. 7.7 using the LAOR model (Laor 1991) and fitting for the inner radius $r_{\rm in}$ and the power-law index q of the emissivity profile, which is described by a power-law of the form $\epsilon(r) \propto r^{-q}$. The outer disc radius is fixed at the maximum allowed value of 400 $r_{\rm g}$ ($r_{\rm g} \equiv GM/c^2$), and the disc inclination is constrained to be approximately 1σ from the adopted value of Orosz et al. (2011) (i.e. between 71 and 78 degrees). The line energy is constrained between 6.4–6.97 keV. The fit achieved by including the LAOR component, shown in Fig. 7.8, results in $\chi^2/\nu = 1848.0/1501$, an improvement of $\Delta\chi^2 = -416$ for 5 fewer degrees of freedom (compared to the best-fitting continuum model with no line feature). The best fit parameters for this model are detailed in Table 7.6.2 (Model 1).

It can be seen from the ratio plot shown in Fig. 7.8 that this simple, heuristic model, although mostly adequate, does not provide a detailed description of all the features present in the 6–8 keV range. Adding a narrow Gaussian line at ≈ 6.7 keV

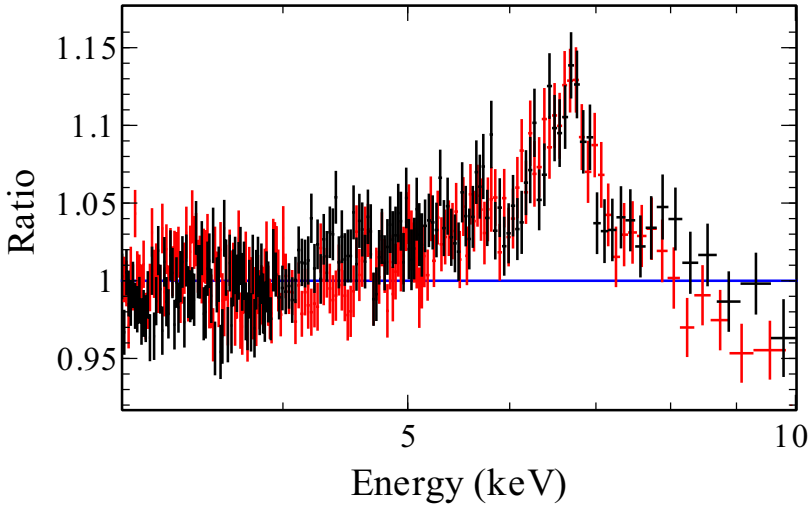

Figure 7.7.— Data/model ratio for a phenomenological continuum model consisting of a thermal disc and a Compton component. *ASCA* GIS-2 and GIS-3 spectra are shown in black and red respectively. The data were fitted jointly in the 1–4 and 7–10 keV energy range. The residuals in the 4–7 keV band show the relativistic nature (asymmetry and broadness) of the iron-emission line profile. The data have been rebinned for plotting purposes. The data/model ratio for the full energy range is shown in Fig. 7.8.

only marginally improves the fit[4] ($\Delta\chi^2 = -14.4$ for 2 fewer degrees of freedom), with evidence for additional residuals, which are possibly associated with Fe K-shell absorption edges in partially ionised material (Ross & Fabian 1993; Ross et al. 1996). Such features are usually present at ≈ 7.1 keV in TD-state spectra of black-hole binaries (Done et al. 1992; Reis et al. 2008). In order to properly account for the panorama of features associated with the reprocessing of radiation in the accretion disc, we now consider complete reflection models.

7.6.2 Reflection Analysis – *ASCA*

We replace the LAOR component with REFLIONX (Ross & Fabian 2005), which describes the spectrum reflected from an optically-thick and cold atmosphere of constant density that is illuminated by a power-law spectrum (Section 7.4). The parameters of the model are the iron abundance (set to Solar), photon index of the illuminating power law, ionisation parameter, and normalisation. The gravitational and Doppler effects are accounted for using the fully relativistic convolution model KERRCONV (Brenneman & Reynolds 2006), which includes black-hole spin as a fit parameter. The power-law indexes of REFLIONX and the Compton component (SIMPL-R) are tied, and, as before, we constrain the inclination to lie between 71 and 78 degrees and include a narrow Gaussian line at ≈ 6.7 keV. The model results in a good and improved fit to the data with $\chi^2/\nu = 1752.3/1499$ (Model 2 in Table 7.6.2); however it still does not fully account for the reflection features, with residuals present at ≈ 7 keV (top panel of Fig. 7.9).

[4]This feature was previously associated (Tomsick et al. 2001) with emission from the Galactic ridge (Valinia & Marshall 1998).

Although the scattered fraction for this spectrum is high, $f_{\rm SC} > 50$ per cent, and the CF method is not applicable, we nevertheless investigated the effect of switching the continuum model from DISKBB to KERRBB (Model 3), with the mass, distance and inclination frozen at their nominal values. This change produced insignificant differences in the fit parameters (Table 7.6.2). For both Models 2 and 3, we find that the spin parameter is moderate (< 0.75). Meanwhile, the disc ionisation has pegged at its maximum value ($\xi = 10^4\,{\rm erg\ cm^{-2}\ s^{-1}}$) indicating that the surface layer of the accretion disc is highly ionised, with iron possibly being fully ionised. In such circumstances, the Fe absorption edge can be particularly strong and is often found to be highly smeared (see Ross et al. 1996 and references therein).

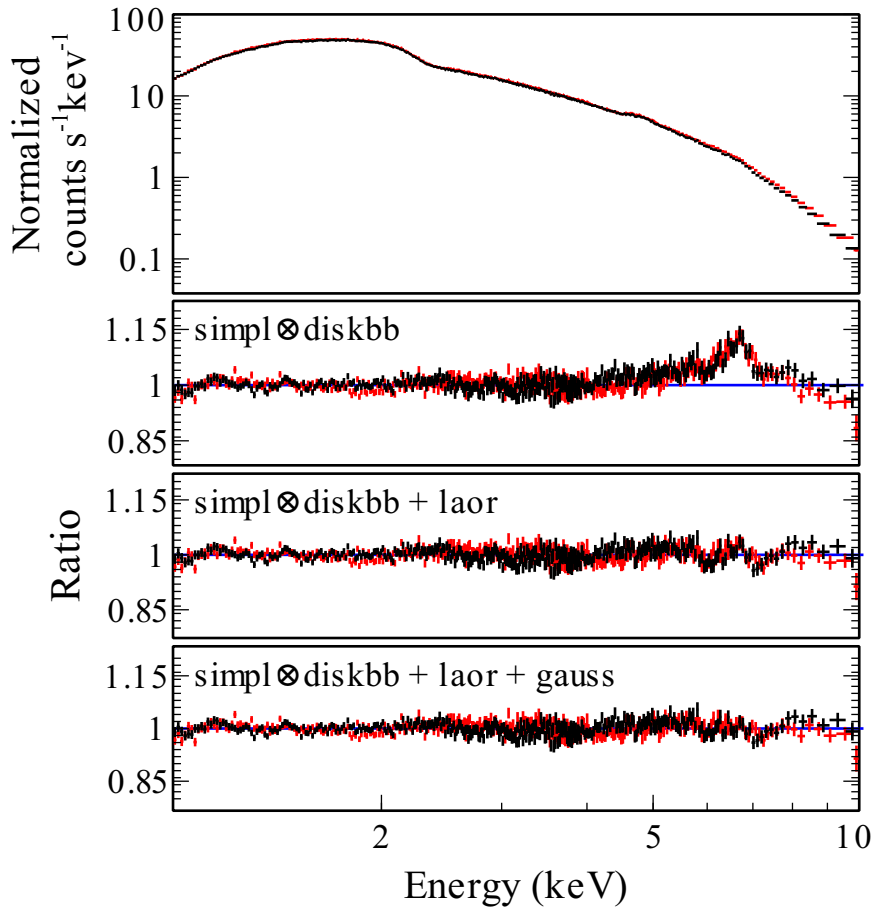

Figure 7.8.— *(top:)* The *ASCA* spectra. Below are plots of the ratio of the data to a phenomenological continuum model consisting of thermal-disc and Compton components plus a LAOR line; in the bottommost panel, a narrow Gaussian line has been added to the model.

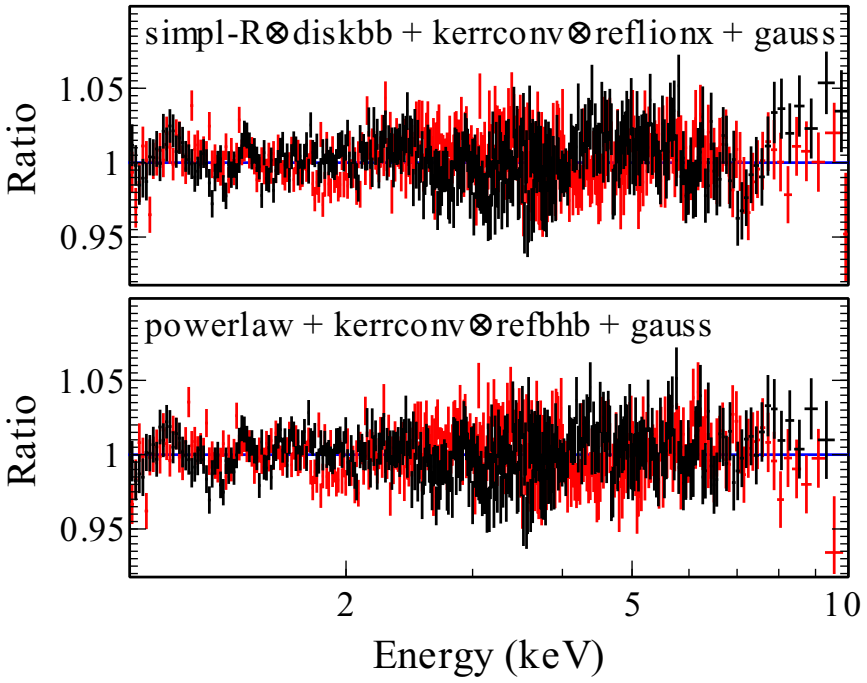

Figure 7.9.— Data/model ratio for (*top:*) the REFLIONX model together with a separate thermal emission and Compton component. (*bottom:*) Self-consistent thermal emission and reflection (REFBHB) together with a power-law component.

Table 7.4. *ASCA* 1–10 keV Reflection Spectral Fit Parameters

Parameters	Model 1 SIMPL⊗DISKBB +LAOR	Model 2 SIMPL-R⊗DISKBB +KERRCONV⊗REFLIONX	Model 3 SIMPL-R⊗KERRBB +KERRCONV⊗REFLIONX	Model 4 POWERLAW +KERRCONV⊗REFBHB	Model 5 POWERLAW +KERRCONV⊗REFBHB
$N_{\rm H}$ ($\times 10^{22}$ cm^{-2})	$0.576^{+0.003}_{-0.002}$	$0.650^{+0.006}_{-0.002}$	$0.666^{+0.002}_{-0.007}$	$0.663^{+0.002}_{-0.006}$	$0.653^{+0.009}_{-0.007}$
Γ	2.40 ± 0.01	$2.329^{+0.006}_{-0.010}$	$2.320^{+0.003}_{-0.002}$	2.24 ± 0.01	$2.22^{+0.03}_{-0.02}$
$f_{\rm SC}$ (N_{hard})[a]	0.6 ± 0.3	0.64 ± 0.04	0.616 ± 0.002	2.4 ± 0.1	$2.3^{+0.2}_{-0.1}$
kT (keV)	$0.513^{+0.009}_{-0.006}$	$0.566^{+0.001}_{-0.013}$	—	0.540 ± 0.001	$0.542^{+0.002}_{-0.001}$
N_{diskbb} ($(\frac{R/km}{D/10\ kpc})^2 cos\ i$)	5200^{+500}_{-200}	4211^{+86}_{-272}	—	—	—
$\dot{M}$ ($\times 10^{18}$ g s^{-1})	—	—	$0.668^{+0.003}_{-0.03}$	—	—
q	2.0 ± 0.2	1.88 ± 0.01	$1.85^{+0.2}_{-0.30}$	$2.38^{+0.04}_{-0.07}$	$2.5^{+0.2}_{-0.1}$
i (degrees)	71–78	71–78	71–78	77 ± 1	82_{-3}
E_{Laor} (keV)	$6.40^{+0.01}$	—	—	—	—
$r_{\rm in}$ ($r_{\rm g}$)	$8.2^{+2.9}_{-3.5}$	—	—	—	—
N_{laor} ($\times 10^{-3}$)	7.1 ± 0.1	—	—	—	—
ξ (erg cm s^{-1})	—	10000_{-320}	10000_{-900}	—	—
$N_{reflionx}$ ($\times 10^{-6}$)	—	1.32 ± 0.06	$1.288^{+0.004}_{-0.070}$	—	—
H_{den} ($\times 10^{22}$H cm^{-3})	—	—	—	$1.00_{-0.02}$	$1.00_{-0.02}$
F_{illum}/F_{bb}	—	—	—	$0.29^{+0.03}_{-0.18}$	$0.25^{+0.08}_{-0.07}$
N_{refbhb} ($\times 10^{-2}$)	—	—	—	$6.2^{+0.2}_{-2.7}$	$5.96^{+0.5}_{-1.1}$
spin (a_*)	—	< 0.75	$0.45(< 0.75)$	$0.6(> 0.38)$	$0.55^{+0.15}_{-0.22}$
χ^2/ν	1848.0/1501	1752.3/1499	1759.5/1499	1700.9/1498	1698.6/1498

Notes: All errors are quoted at the 90 per cent confidence level for one parameter of interest ($\Delta\chi^2 = 2.71$). Model 1, which is purely phenomenological, uses the familiar LAOR line and allows a comparison with previous work. Models 2 and 3 use different disc components; however both of them employ the same full reflection model (REFLIONX), while treating the Compton component using SIMPL-R (Section 7.4.1). The core of Model 4 is REFBHB which is likewise a full reflection model, with the added virtue that it self-consistently models the thermal component as well. In Models 1 to 4 the inclination was constrained to be between 71 and 78 degrees. In Model 5 the inclination is allowed to range from 60 to 82 degrees. A constraint on the inclination was achieved only for Models 4 and 5.

[a] The POWERLAW normalisation is in photons cm^{-2} s^{-1} for Models 4 and 5. For Models 1–3, the normalisation is given by the dimensionless parameter $f_{\rm SC}$ (see Section 7.3).

In order to incorporate the effects of thermal ionisation expected for a hot accretion disc, we replace REFLIONX with the model REFBHB developed by Ross & Fabian (2007). This reflection model accounts for both thermal X-ray emission and the reflection features. The effects of Compton broadening in the disc are fully included, subject to the one assumption of a constant-density atmosphere. The parameters of the model are the number density of hydrogen in the illuminated surface layer, $H_{\rm den}$, the temperature of the blackbody heating the surface layers, the power-law photon index, and the ratio of the total flux illuminating the disc to the total blackbody flux emitted by the disc. Again, we tie the power-law index of REFBHB to that of the Compton component – now modeled as a standard power law – and convolve the spectrum with KERRCONV in order to include relativistic broadening. The model results in an excellent fit to the data with $\chi^2/\nu = 1700.9/1498$ (Model 4, see bottom panel in Fig. 7.9), however the hydrogen surface density is pegged at the maximum value of the model. The ionisation state of the disc is inversely proportional to the value of the hydrogen density and thus the pegged value implies that the fit is requiring a higher amount of emission in the form of discrete features as opposed to the near featureless reflected continuum arising from a highly ionised disc-surface. A similar result would be produced by increasing the iron abundance. Unfortunately the model in its current format does not allow for a change in elemental abundances. In order to investigate the effect that H_{den} has on the spin parameter we fixed it at 1×10^{21} H cm^{-3} using Model 4 (i.e. an order of magnitude less than the value presented in Table 7.6.2) and refitted the data. This constraint on H_{den} resulted in an adequate fit with $\chi^2/\nu = 1731.6/1499$ and a spin value of 0.60 ± 0.05. We note here that POWERLAW has been used to model

the Compton component. We have explored replacing POWERLAW with SIMPL-R, and the fit becomes worse with $\chi^2/\nu = 1802.5/1498$. However, the value of the spin parameter, as well as those of the reflection parameters, remains largely unchanged.

From Models 1 to 4 it is clear that the spin parameter is consistently below ≈ 0.75. However, in the first three cases inclination is not constrained. For this reason we explore a very broad range of i, from 60° to 82°. We note that above this limit, the disc would be super-Eddington during its steady thermal plateau in Fig. 7.1. The best fit is given by Model 5 (Tab. 7.6.2) and reaches the upper inclination limit, netting a small improvement ($\Delta\chi^2 = -2.3$) over Model 4. For all models we see that the emissivity index is consistently below the typical value of three associated with the canonical 'lamp-post' coronal geometry, and is instead more consistent with a slab-like corona. In order to illuminate any degeneracy between the value of spin and either the emissivity index or inclination, we show in Fig. 7.10 the 68, 90 and 95 per cent probability contours for these parameters plotted versus spin. In both instances there exists a small and negative correlation with spin. However it is also clear that q is well constrained between 2.2 and 2.7 and that $i \gtrsim 75°$ at 90 per cent confidence even while including the uncertainty in spin. When we marginalize over these parameters and compute the uncertainty in spin alone (Fig. 7.11 for Model 5), the spin parameter obtained from the gravitational blurring of reflection features is constrained to be in the window $0.33 < a_* < 0.70$ at 90 per cent confidence with the best estimate at $a_* \approx 0.55$. A non-rotating Schwarzschild black hole is rejected at greater than 3σ.

Our measured spin from Fe $K\alpha$ using the REFBHB model is consistently lower than the preliminary value of $a_* = 0.75 - 0.80$ reported by Miller et al. (2009b),

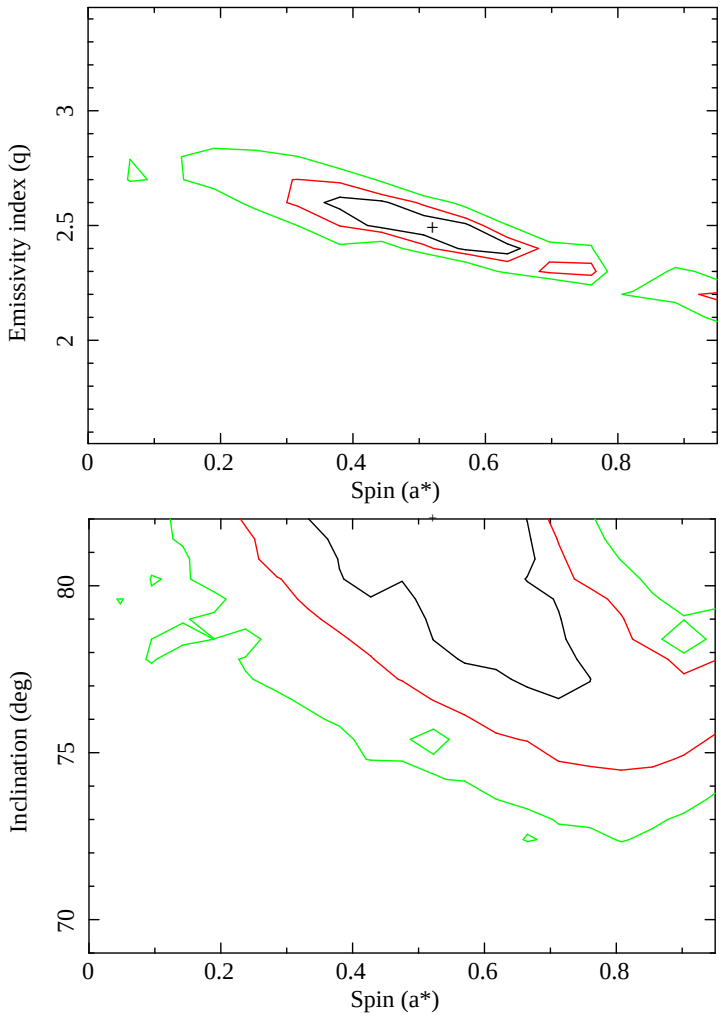

Figure 7.10.— (*top*): Emissivity versus spin contour plot for J1550. The 68, 90 and 95 per cent confidence range for two parameters of interest are shown in black, red and green, respectively. We have allowed i to take any value between $60° \leq i \leq 82°$, and find that the spin is greater than 0.33 at the 90 per cent level of confidence. (*bottom:*) Similar plot for inclination versus spin. We see from the *ASCA* data that a zero spin value is clearly ruled out, as is an inclination lower than 72°.

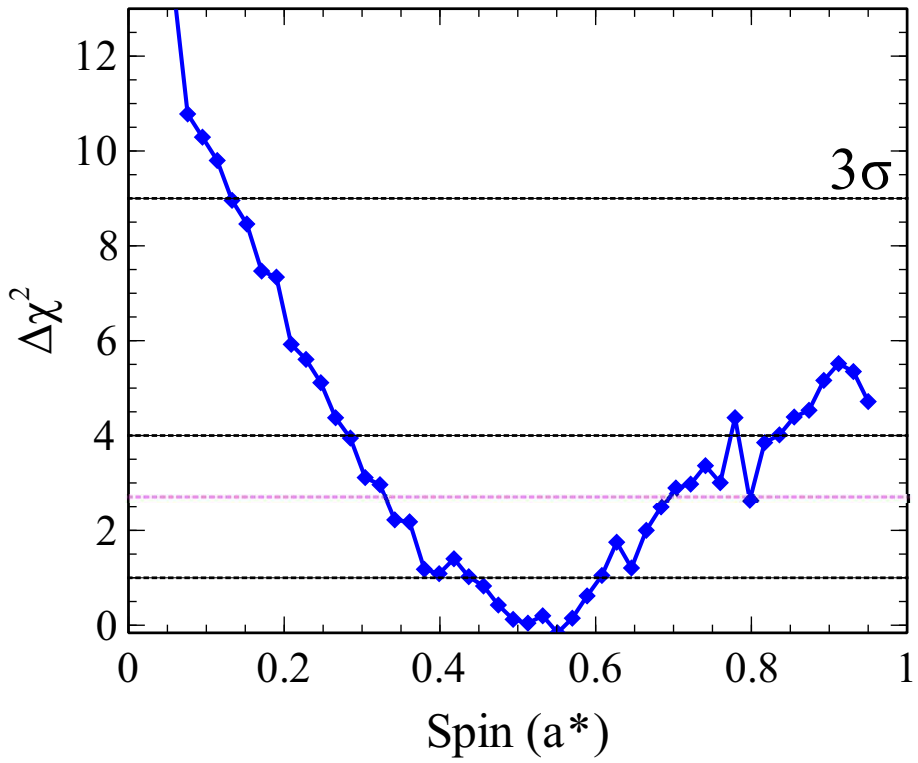

Figure 7.11.— Goodness-of-fit versus spin parameter for J1550. From the reflection features present in the *ASCA* spectra of J1550 we can rule out a non rotating black hole at over 3σ confidence. However we cannot place a comparable strong upper limit on this value. The 90 per cent confidence level ($\Delta\chi^2 = 2.71$ for one parameter of interest) is shown in magenta. The black dotted lines indicate confidence intervals. Spin is constrained to $0.33 < a_* < 0.70$ at the 90 per cent confidence level.

and we have attained a better fit than they ($\Delta\chi^2 \lesssim -100$) for more degrees of freedom. The critical difference in our model and spin estimate comes from having incorporated the effect Compton-broadening of the iron $K\alpha$ line in the hot layers of the accretion disc. With REFBHB the disc is intrinsically hot and therefore the effect of Compton-broadening is fully accounted for when modeling the data. The extra broadening caused by this effect acts to lower the degree of gravitational broadening and as such requires less extreme spin parameters as compared with models where the reflection is assumed to come from a relatively cold surface, e.g, for AGN (Ross & Fabian 2007). Generically it is thus expected that REFLIONX (designed specifically for cold discs) should estimate faster spins than REFBHB. The effect is moderate, but still evident when comparing the upper limits on spin from Table 7.6.2 in which we see that the 90 per cent upper bound extends to 0.75 for Models 2 and 3 (using REFLIONX) as compared to 0.7 for Model 5, which uses REFBHB.

7.6.3 Spin from reflection features – *RXTE*

In order to supplement the *ASCA* spin measurement above, we present an analysis of a sample of ten *RXTE* spectra selected from the composite data set discussed in Sections 7.3 and 7.4 to have the following properties: very large scattered fraction, $f_{\rm SC} > 50$ per cent, goodness of fit, $\chi^2/\nu < 2$, and uniform values of luminosity and photon index, $L_{\rm D}/L_{\rm Edd} \approx 0.2 \pm 0.05$ and $\Gamma \approx 2.5 \pm 0.1$, respectively. We begin by simultaneously modeling the reflection features present in all the *RXTE* spectra using REFLIONX convolved with KERRCONV while using SIMPL-R⊗DISKBB for the thermal plus Compton continuum (Model 2 in Section 7.6.2). (N.B. The REFBHB

component used in Models 4 and 5 was unable to converge to an adequate fit for *RXTE* and provided no spin constraint. Therefore, in this section we adopt Model 2.) The spin, inclination ($60 \leq i \leq 82$) and emissivity index[5] are treated as global parameters among the ten spectra. As in Section 7.3, the neutral hydrogen column density is fixed at $8 \times 10^{21}\,\mathrm{cm}^{-2}$. The remaining parameters were allowed to vary in individual spectra. Fig. 7.12 shows the best-fitting model spectra (top panel) together with the data-to-model ratio for each spectrum (bottom panel). The fit was marginally improved ($\Delta\chi^2 = -30.5$ for 10 degrees of freedom) by including a narrow line at ≈6.7 keV which accounts for the slight curvature in the residuals at that energy (compare the lower two panels in Fig. 7.12).

We find that the global best fit is sensitive to the upper energy range adopted for the *RXTE* spectra, which we attribute in part to a competition between the lower energy reflection features and the high-energy Compton hump. Considering upper ranges between 12–45 keV, the best spin estimate was found between $a_* \approx 0.6 - 0.69$ giving reduced chi-square values from $\chi^2/\nu = 0.4 - 0.8$, with higher values obtained at extended energy ranges. Most importantly, the model consistently estimated the 90 per cent upper limit for spin at $a_* = 0.75$. For the other global parameters, we treat the *RXTE* results as second-tier, but find results consistent with the *ASCA* values: $q \approx 2.5$ and $i > 72^\circ$ (90 per cent).

We are cautious in interpreting this spin estimate using *RXTE* spectral fits, owing to the coarse ($\sim$ 20 per cent) energy resolution. However, we expect that

[5]Because we have selected a homogeneous set of spectra with almost identical luminosities, it is likely that the emissivity index – an indicator of coronal geometry – is the same for all ten spectra.

RXTE should provide robust upper bounds on the degree of relativistic broadening (viz., spin), owing to its vast collecting area and $\lesssim 1$ per cent spectral calibration (Jahoda et al. 2006). We caution towards the significance of the *RXTE* -derived spin parameter and consider the upper limit obtained here as a *complementary result* to that obtained from the *ASCA* data alone, confirming that Fe $K\alpha$ spin is not high.

7.7 Discussion

7.7.1 A Combined Fe $K\alpha$ and CF Result

In the two previous sections, we concluded that both the Fe-line and CF methods predict moderate values of spin, which are quite consistent: $0.33 < a_* < 0.70$ (*ASCA* only) and $-0.11 < a_* < 0.71$, respectively (90 per cent confidence). The CF spin result predicts a slightly narrower Fe-line feature than that found by the Fe-line analysis. Alternatively, the Fe-line measurements consistently favor a high inclination, and therefore require a lesser distance ($D \approx 4$ kpc), in order for the CF results to match.

Having obtained two independent measurements of the spin, we now combine them by convolving the individual spin probability distributions to obtain the joint distribution shown in Fig. 7.13. Our synthesized result is then $0.29 < a_* < 0.62$, with a most probable value of $a_* = 0.49$. Remarkably, based on a model of binary evolution and the GRB collapsar model, Brown et al. (2007) predicted that J1550 formed with $a_* \approx 0.5$. Our results are consistent with their prediction.

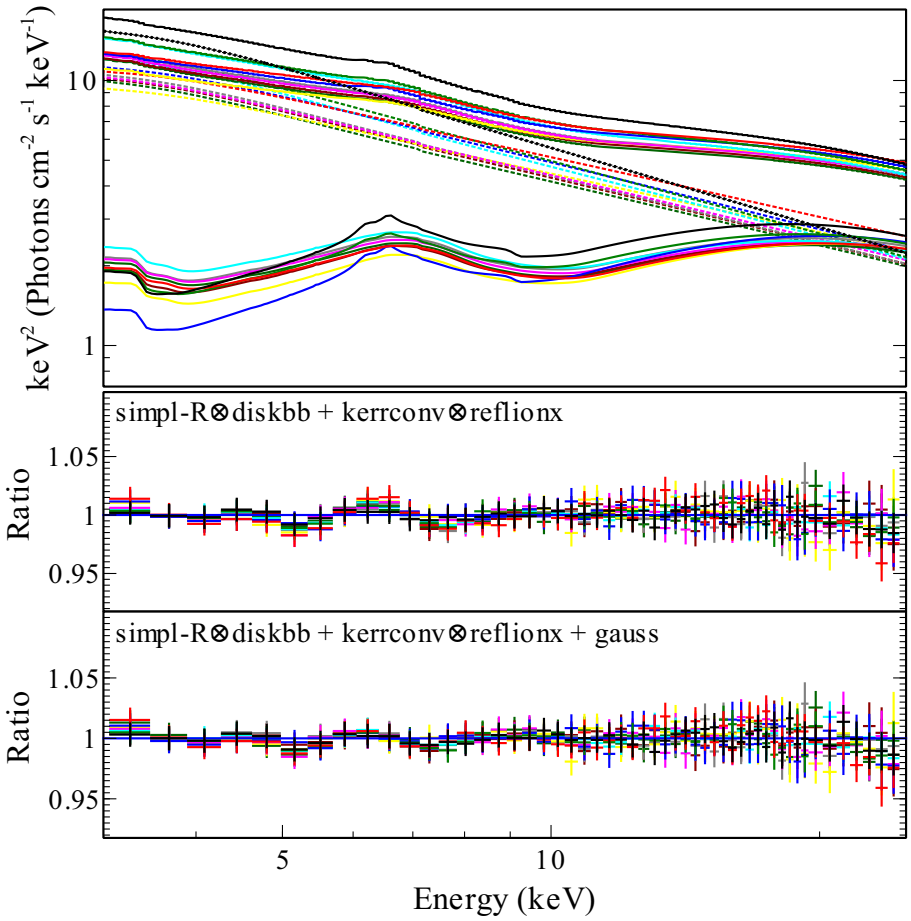

Figure 7.12.— Best-fitting model (*top*) for the ten *RXTE* observations. The model consists of a disc and Compton continuum together with a relativistically blurred reflection component. The spin, inclination, and emissivity index were treated as global parameters (see Section 7.6.3). (*middle:*) Data/model ratio for the above model and (*bottom:*) after the inclusion of a narrow Gaussian emission line.

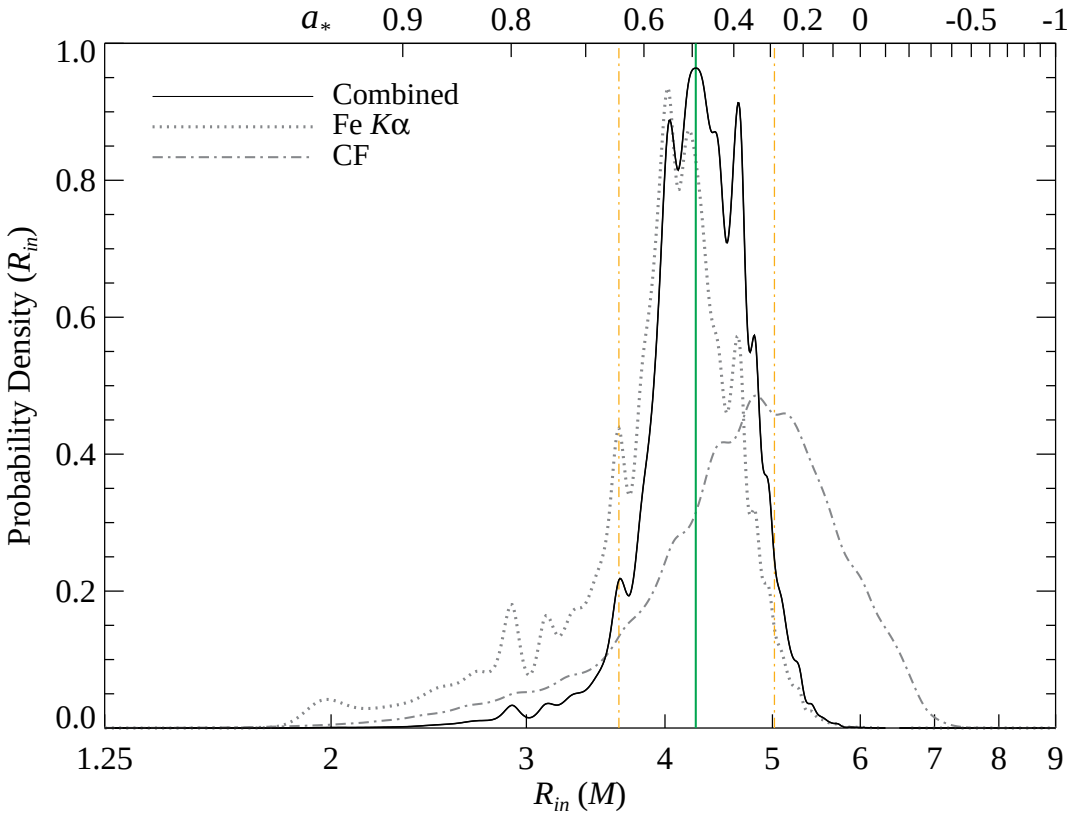

Figure 7.13.— Combined Fe $K\alpha$ and CF probability density for $R_{\rm in}$ and a_*. The net result is again a moderate value in-between the two individual estimates ($a_* = 0.49^{+0.13}_{-0.20}$, 90 per cent confidence).

7.7.2 Testing the No-Hair Theorem

The no-hair theorem states that a macroscopic black hole is described by just two parameters: M and a_*[6]. A violation of the no-hair theorem would prove that either the object in question is not a bona fide Kerr black hole or that general relativity is in error. Presently, tests of the no-hair theorem proposed by various groups center on searching for deviations of the quadrupole and higher moments from the expected Kerr value (see e.g., Ryan 1997; Will 2008; Johannsen & Psaltis 2010; Vigeland & Hughes 2010; Bambi & Barausse 2011).

The Fe-line and CF methods both rely upon a common assumption that $R_{\rm ISCO}$ is the truncation radius of the disc. However, under alternative theories of gravity, one expects the two methods to deliver different values of spin because the models will scale differently with radius. This measured discrepancy could then be rectified by appealing to perturbations to the Kerr solution (akin to those described by the works mentioned above). The fact that we find consistent values of spin provides tacit support for the no-hair theorem. However, the errors in both spin measurements are large, and we do not yet understand all sources of systematic error. Nevertheless, this example gives a foretaste of how spin measurements can contribute to deep questions in physics.

[6]In principle, it could have an electric charge, but astrophysical black holes are unlikely to have enough charge to be dynamically important.

7.7.3 Confronting GRMHD Simulations

Recently, it has become feasible, via general-relativistic magnetohydrodynamic (GRMHD) simulations, to assess the differences between MRI-driven accretion flows and the idealised α-disc model, upon which our CF model is based. Differences include both a non-zero torque inside the ISCO and an altered angular momentum profile for the disc.

To calibrate the magnitude of these differences in the context of the CF model, Kulkarni et al. (2011) have analysed a suite of GRMHD simulations of accretion onto spinning BHs. Because it is computationally very expensive to simulate thin discs, the discs they consider are about twice as thick as those considered here. In general, they conclude that deviations from the Novikov-Thorne model, upon which the CF method is based, tend to over-estimate spin ($r_{\rm in}$ is too small by several per cent and deviates more for thicker discs and at higher inclinations). For the inclination of J1550, they find that the magnitude of this bias is ≈ 10 per cent ($\Delta a_* \approx 0.13$). We note that the actual change is expected to be smaller over the luminosity range we use because the discs we consider are significantly thinner.

Similar MHD simulations have been made to assess a principal assumption of the Fe-line method, namely, that the line emission from within the ISCO is negligible (Reynolds & Fabian 2008). Including the effect of contributing plunging-region emission results in intrinsically broader line profiles and hence will lower the estimate for spin. For the disc thickness and spin values in question, simulations predict that this effect could possibly shift $r_{\rm in}$ by ~ 12 per cent (value taken from fig. 5 in Reynolds & Fabian (2008)), thereby decreasing the most probable Fe $K\alpha$ estimate of

spin from $a_* \approx 0.55$ to ≈ 0.4, in close agreement with the best CF value of $a_* \approx 0.34$.

Based on the work of Kulkarni et al. (2011) and (Reynolds & Fabian 2008), we conclude that both spin estimates are likely too high (≈ 10 per cent low in $r_{\rm in}$), which strengthens our conclusion that the spin of J1550 is moderate.

7.7.4 The Question of Alignment

The spin of an accreting black hole in a binary is expected to align with the orbital angular momentum vector of the system within $\approx 10^7 - 10^8$ years (Maccarone 2002). A recent population synthesis study (Fragos et al. 2010), which makes conservative assumptions concerning the torques acting to align a black hole, predicts that most black holes will be aligned to better than 10°. In Section 7.6, we constrained the inclination of the inner, reflecting portion of the accretion disc (Fig. 7.10). This allows us to check on the relative alignment of the black-hole spin axis (which is aligned with this inner-disc region; Lodato & Pringle 2006) and the orbital vector. In our exploration of the Fe $K\alpha$ model, for a wide range of orbital inclinations (60° – 82°), we find a best-fitting inclination for the inner disc of $\approx 75 - 82°$. This value is consistent with the orbital inclination angle given by our dynamical model, $i = 74.7 \pm 3.8$ degrees (Orosz et al. 2011), which validates the CF assumption of alignment (Li et al. 2005), while simultaneously providing support for the dynamical model.

7.7.5 Implications of a Low-Spin Microquasar

The low spins of J1550 and the microquasar A0620–00 ($a_* \approx 0.1$; Gou et al. 2010) challenge the long-standing and widely-held belief that there is a strong connection between black-hole spin and relativistic jets (Blandford & Znajek 1977; hereafter BZ), while these low spins support the conclusion of a literature study by Fender et al. (2010) that found no evidence for a correlation between black-hole spin and jet power. By contrast, simulations strongly suggest that if jets are powered by black-hole spin, then the jet power will increase dramatically with increasing a_* (Tchekhovskoy et al. 2010). However, it is alternatively possible for a magnetized disc to directly power a jet (here, a centrifugally-driven outflow) without any need to harness power from spin of the black hole (Blandford & Payne 1982; hereafter BP). In fact, more power can potentially be provided to a jet by the disc under the BP mechanism than from the BH's spin (via the BZ mechanism) for spins $a_* < 0.4$. For these discs, the rotation rate at the ISCO is faster than the rotation of the black hole at its horizon, and the available power from the BZ mechanism is generally low (e.g. McKinney 2005).

Given the low spins of J1550 and A0620–00, we suggest that their episodic jets are driven in part by the accretion disc, while the jet of an extreme-spin source like GRS 1915+105 (McClintock et al. 2006; Blum et al. 2009) may instead be fully powered by the BZ mechanism. A useful comparison of the operational regimes of BP and BZ is given by Garofalo et al. (2010). They show that BP is always viable, but that BZ is the more likely mechanism for high-spin sources to produce jets. We note the caveat that there is no definitive measurement of J1550's jet power,

and that the magnetic field of the disc is likewise difficult to estimate; our claim is motivated purely by the existence of powerful jets in two low-spin microquasars.

The relativistic, two-sided jet of J1550 was launched during the remarkable 7 Crab flare (see Section 7.1). In what follows, we show that during this daylong event the luminosity of the accretion disc was close to, or perhaps at, its Eddington limit. The synchronicity of this extreme-luminosity condition of the disc and the jet-launching X-ray flare suggest that radiation pressure may have been important in collimating or feeding the jet (possibly indirectly via a radiatively-driven disc wind; for a discussion of the interplay between jet and wind, see Neilsen & Lee 2009 and Miller et al. 2008a).

In Fig. 7.14, we plot the intrinsic accretion-disc luminosity during the flare state versus the luminosity during the thermal-dominant plateau state (Days 105–182; see Fig. 7.1). Each data point represents an analysis of the complete J1550 data set for one triplet of values of M, i and D from among the 42,500 triplets used in our Odyssey cluster analysis (Appendix A.4). The spin value for each point (averaged over the *gold* and *silver* data) is colour-coded according to the bar at the top of the plot. The point corresponding to the dynamical model adopted from Orosz et al. (2011), their Model F, is labelled and marked by a red cross. The five less probable models considered by Orosz et al. are marked by black crosses. We conclude that the disc in Model F (by far the most probable model; see Appendix A.5), is very near its Eddington limit at the time the jet is launched.

Luminous discs are geometrically thick and widely believed to be effective at driving jets. In the case of the J1550 flare, the disc is not only thick, it is also near

its Eddington limit, so that it will provide substantial radiation pressure, can sustain stronger magnetic fields, and possibly shed material via a radiation-driven outflow, thereby promoting the ejection of a jet. In any case, as a bottom line, the low spins of J1550 and A0620–00 indicate that spin is not the sole driver behind all powerful episodic jets.

7.8 Conclusion

For the first time in a single work, we have determined high-quality, independent estimates of the spin of an accreting black hole using the two leading methods. In our CF analysis, we carefully explored the sensitivity of our results to a wide range of model-dependent systematic errors and observational errors. We conclude that J1550 is a slowly spinning black hole with $a_* \approx 0.34$, while ruling out spins larger than $a_* \gtrsim 0.71$ at 90 per cent confidence. Next, we analysed the Fe $K\alpha$ and reflection signatures in bright, intermediate spectral states of J1550. By modeling these broad, skewed features, we obtained a slightly higher estimate of the spin, $a_* \approx 0.55^{+0.15}_{-0.22}$ (at 90 per cent confidence), while also deriving an estimate of the inclination angle of the inner disc that is in close agreement with the orbital inclination angle (Orosz et al. 2011). Combining the two spin estimates, we conclude that J1550, like the microquasar A0620–00, is a slowly spinning black hole.

The low spins of both J1550 and A0620–00 indicate that, for at least some microquasars, BZ-type mechanisms are not primary in driving powerful episodic jets, and that other mechanisms (perhaps BP) are at play. The near Eddington-limited 7 Crab flare observed for J1550 suggests that radiation-pressure support from a

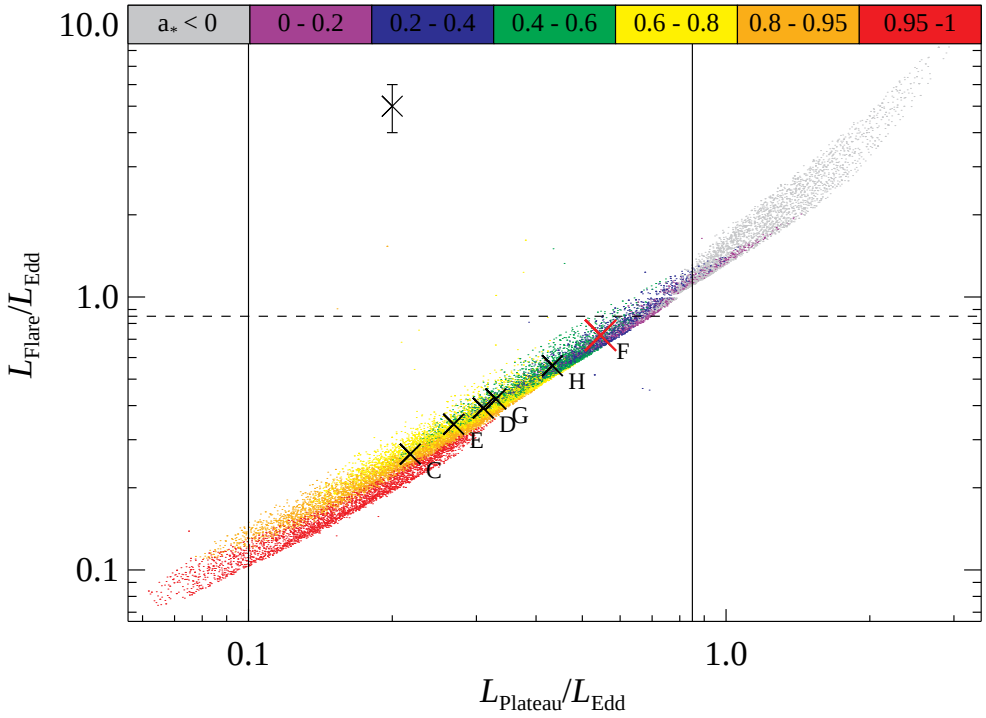

Figure 7.14.— The intrinsic (i.e., seed) luminosity of the disc component during the 7 Crab flare versus the luminosity during the thermal plateau phase. In order to avoid saturating the plot, we show only half the data points, which were selected at random. The vertical black lines mark the lower and upper luminosity thresholds, and the horizontal dashed line corresponds to the Eddington limit of an accretion disc (Section 7.5). Note that Model F is very near this limit.

thermal disc is one possible way that low-spin black holes are aided in driving large-scale relativistic jets.

7.9 Appendix: Continuum-Fitting: Assessing the Systematic Uncertainties

7.9.1 Model Parameters

We consider the effect of the principal parameters listed in Table 7.3 on our final determination of the spin (Fig. 7.6) for Model S (Section 7.3) and Model I (Section 7.4). Here and below, we consider only the *gold* data. As in Sections 7.3 and 7.4, we fix M, i, and D at their fiducial values (Section 7.1). Now, element by element, we consider the changes to the parameters and model components that are given in Table 7.3.

As is illustrated by Fig. 7.6, and shown in Table 7.3 (P1), decreasing the viscosity parameter by a factor of 10 from $\alpha = 0.1$ to $\alpha = 0.01$ results in a decrease in the inner disc radius by $\sim 3 - 4$ per cent. This is the largest of the 17 changes listed in Table 7.3, and it is dwarfed by the effects of the uncertainties in the external input parameters M, i, and D (Section 7.5), which are analysed separately.

The column density (P2–3) is next varied over a broad range, $N_{\rm H} = 6 - 10 \times 10^{21}$ cm^{-2}, which corresponds to $\gtrsim 8\sigma$ relative to the *Chandra* grating value (see Section 7.3.2, Miller et al. 2003). We consider this extreme range because of the discrepant results for $N_{\rm H}$ obtained using *ASCA* data (see Section 7.6), which

we attribute to an error in the calibration of the *ASCA* detectors at low energies. As shown in Table 7.3, our liberal estimate of the uncertainty in $N_{\rm H}$ affects our determination of $r_{\rm in}$ by < 3 per cent.

We next explore the parameters of the IREFLECT model. We test smaller covering factors of 1/2 and 1/10 by linking the covering factor in IREFLECT to (negative) '$(x-1)$' where x is a parameter of SIMPL-R. The sign is made negative to act as a switch in the model and isolate reflection from the direct (illuminating) component. Thus, we consider two cases: $x = 1.5$ (P4) and $x = 1.1$ (P5). We next try fitting for the covering factor, allowing it to vary between 0 and 1, while also fitting for the emissivity index, which we constrain to lie in the range $2 < q < 5$ (P6). As shown in Table 7.3, the effect of this exercise on $r_{\rm in}$ is small, ~ 1 per cent. We also perform a set of fits using a fixed $q = 3$ (P7; corresponding to a standard lamp-post model); the resultant fits are on average worse by $\approx 3\sigma$, while $r_{\rm in}$ shrinks by about 3 per cent.

An even smaller effect is obtained by varying the disc temperature in Model I. First, we decrease $T_{\rm disc}$ (P8) by a factor of 5 relative to its assumed value (Section 7.4.2), and next we try a larger temperature of 10^7 K (P9), twice the fiducial value. We find that in the former run, the ionisation parameter increases, and in the latter it decreases, but that in both cases the effect on $r_{\rm in}$ is negligible (< 0.2 per cent).

To account for the high ionisation parameter measured using Model I, we test shifting the Fe $K\alpha$ line to a higher intrinsic energy of 6.8 keV(P10), a value intermediate between $K\alpha$ produced by He-like Fe^{+24} and H-like Fe^{+25}. This shift in

the line energy causes a ≈ 2 per cent decrease in $r_{\rm in}$.

Lastly, for Model S we adjust the width of the SMEDGE component $W_{\rm Edge}$ to first half (P11) and then twice (P12) its nominal value of 7 keV. This impacts $r_{\rm in}$ by < 0.5 per cent.

In summary, as we found earlier in our study of LMC X-3 (Steiner et al. 2010), α is the parameter (aside from M, i, and D) that introduces the largest uncertainty in determining spin via the CF method.

7.9.2 Model Components

We begin by substituting BHSPEC (Davis & Hubeny 2006) for the thermal disc component in place of KERRBB2 (see Section 7.4.2 in McClintock et al. 2006 for a discussion of these relativistic disc models). The virtue of BHSPEC relative to KERRBB2 is that it directly incorporates the effects of spectral hardening; its drawback is that it does not include returning radiation, which heats the disc. Employing BHSPEC instead, we find that $r_{\rm in}$ is increased by $\approx 1-3$ per cent (M1 in Table 7.3).

Next, we explore the possibility that the power-law component is cut off exponentially at high energy (e.g., thermal Comptonisation), while allowing the cut-off energy to vary over the range $kT_e = 25 - 200$ keV. ($f_{\rm SC}$ should in principle be corrected to achieve photon conservation, however we did not do so here because this correction is negligible for the *gold* spectra.) We find that the effect of a possible cutoff is small, changing $r_{\rm in}$ by $\lesssim 1.5$ per cent (M2). In addition, we explore generating the power law using the double-sided version of SIMPL and SIMPL-R (in

place of the upscattering-only version). The effect on $r_{\rm in}$ is $\lesssim 0.3$ per cent (M3).

Lastly, we examine the effect of using one reflection model versus another. We find that both IREFLECT and REFLIONX give somewhat smaller values of $r_{\rm in}$ than SMEDGE, and that the effect is small, $\lesssim 3$ per cent (M4, M5).

7.9.3 Flux

As described in Section 7.5, we include a liberal ~ 10 per cent uncertainty in the absolute flux calibration. Because the luminosity of the thermal component at a given colour temperature scales proportionally to $r_{\rm in}^2$, a 10 per cent adjustment to the flux normalisation introduces a $\sim$5 per cent uncertainty in $r_{\rm in}$.

7.9.4 Black-Hole Mass, Inclination and Distance

While analysing the X-ray spectral data, we have used the best estimates for M, i and D (Section 7.1) taken from Model F of table 1 in Orosz et al. (2011). In order to determine how the spin measurement depends upon uncertainties in the model of Orosz et. al. we use the Odyssey computing cluster at Harvard University and replicate our analysis over a 3-D grid of 42,500 points distributed uniformly over mass, inclination, and distance. The grid spans the ranges $M = 5 - 17.5$ M$_\odot$, $i = 36 - 85^\circ$ and $D = 3 - 7$ kpc, respectively. We adopt the 3 kpc distance bound following Hannikainen et al. (2009); the 7 kpc bound is a relativistic limit based on the proper motion of the X-ray jets (Corbel et al. 2002): $D \leq c/\sqrt{\mu_a \mu_r} \lesssim 7$ kpc (e.g., Mirabel & Rodríguez 1999). At each grid point, we compute a table of the spectral

hardening factor (e.g., see Gou et al. 2010) and fit all of the available TD, SPL, and INT spectra. We use Model S (Section 7.3.2) because it is computationally efficient and has the best performance of all three CF models considered. We perform the analysis for both values of disc viscosity: $\alpha = 0.01$ and $\alpha = 0.1$.

We then apply our data selection criteria, obtaining a sample of *gold* and *silver* spectra (typically 50–100) at each of the 42,500 grid points. From this we derive a spin probability distribution unique to each point. Before summing over the grid, we impose the following grid point selection constraints: First, the grid point's inclination must be below the eclipsing limit, $i < 82°$ (see e.g., Narayan & McClintock 2005). Secondly, as discussed in Section 7.5, we require that the intrinsic disc luminosity during the TD-state plateau phase (days 105–181; Fig. 7.1) fall in the range $0.10 < L_{\rm D}/L_{\rm Edd} < 0.85$. We combine the distributions for all satisfactory grid points, weighting each according to its location in the grid (with high weights occurring at probable values of M, i, and D).

7.9.5 Rolling Together the Uncertainties

We combine the systematic uncertainties discussed above in two stages. Referring to Table 7.3, in the first stage we combine in quadrature the individual values in the Model S column for rows P11-12, M1, M2-3, M4-5 with half the value for P2-3 (half because the range of variation considered for $N_{\rm H}$ is so extreme). For each of the parameters $N_{\rm H}$ and $W_{\rm Edge}$, we use the larger of the deviations given in the table. The resultant error of 4.2 per cent is combined with the 5 per cent error in $r_{\rm in}$ from flux uncertainty to give a net error of 6.5 per cent. This combined uncertainty sets the

half-length for a boxcar smoothing kernel that we apply to the full spin distribution. Equally-weighted distributions using both values of α are included in this step.

The resulting distribution is shown in Fig. 7.15. Because we have so far considered just dynamical Model F, the distribution of $r_{\rm in}$ is narrower, $-0.14 < a_* < 0.57$ (90 per cent confidence level) than our final distribution shown in Fig. 7.6, although the most probable value of spin is unchanged, $a_* = 0.34$. We now go on to the second stage in combining sources of error and consider an ensemble of possible dynamical models.

The case of J1550 is unusual in that there are several candidate models which produce reasonable fits to the dynamical data, which are summarized in table 1 in Orosz et al. (2011). Above, we considered only Model F, the most probable model. We now incorporate the possibility that one of the five alternative models (Models C-E and Models G & H) are correct. Models A and B do not constrain the dynamical model satisfactorily, and do not allow one to obtain a useful distance estimate, and so they are disregarded here.

As was done above for Model F, a spin ($r_{\rm in}$) probability distribution is obtained for each candidate dynamical model. For each model, including Model F, we use the total χ^2 (summed for the velocity data and the light curve data, both optical and infrared) to determine its corrected Akaike Information Criterion (AICc; Akaike 1974; Hurvich & Tsai 1989), which is closely related to the log-likelihood of each model. With these values, AIC-weights are assigned to each model (i): $W_{{\rm AIC},\ i} = exp[-1/2\ ({\rm AICc}_i - inf\{{\rm AICc}\})]$ (Burnham & Anderson 2002).

Our fiducial dynamical model is by far the most likely, carrying ~ 84 per cent

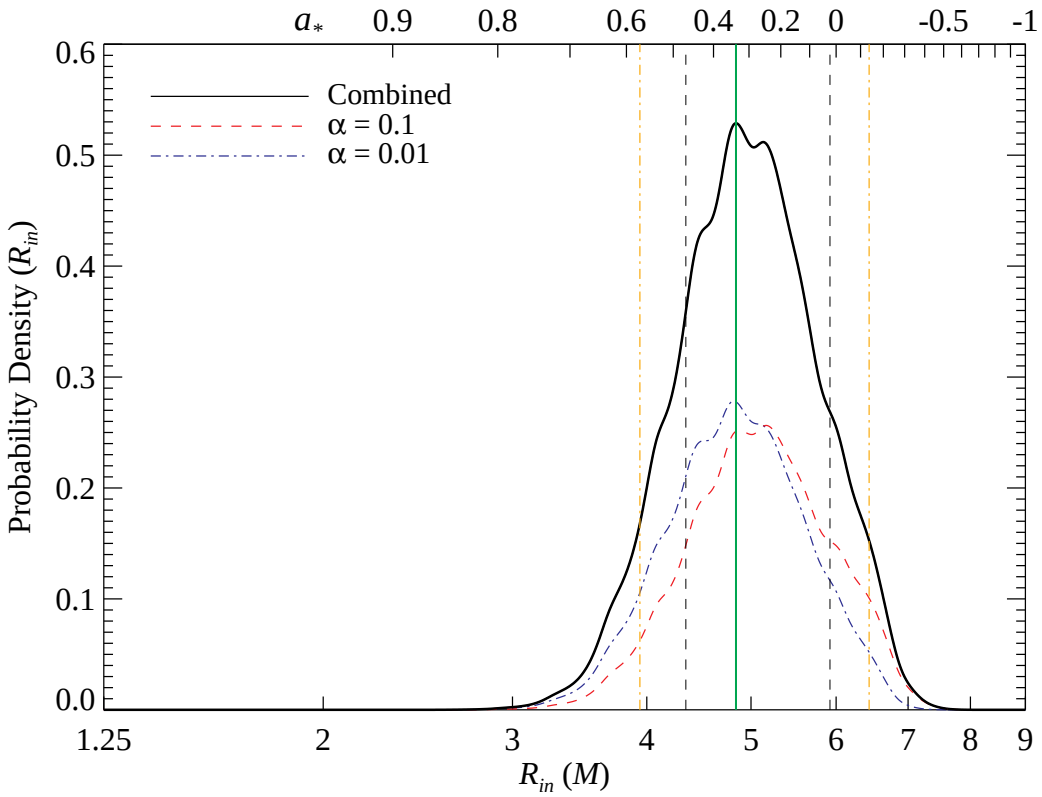

Figure 7.15.— Similar to Fig. 7.6, but using just Model F in Orosz et al. (2011). The green, black, and gold vertical lines indicate the most likely value for $R_{\rm in}$ (a_*), and 1σ and 90 per cent confidence interval limits, respectively.

of the total weight. A weighted sum is computed using the AIC-weights to obtain a composite spin distribution. This is broadened using the boxcar smoothing kernel described above (13 per cent width) to produce the final distribution as shown in Fig. 7.6. *Thus, this final result incorporates uncertainties in the choice of the dynamical model; the dynamical model uncertainties; the X-ray spectral model and parameter settings; and a 10 per cent uncertainty in the X-ray flux calibration.*

Chapter 8

Conclusions and Future Directions

By virtue of the no-hair theorem, we have completely described astrophysical objects whose event horizons are smaller in size than the Boston metropolitan area. Remarkably, the 10-million degree disk of gas orbiting these black holes, which is about the size of Massachusetts, is capable of radiating 500,000 times the total power of the Sun. These accreting black holes and their surrounding environments provide a unique opportunity for testing general relativity in the regime of strong gravity. Our studies of these accreting black holes have established a foundation for the continuum-fitting method of measuring black hole spin and have produced some of the first estimates of the spins of stellar-mass black holes.

8.1 Summary: Spectral Model

In Chapters 2 and 3, a new and self-consistent Comptonization model was introduced in order to describe the power-law component of emission that is present in the

spectra of all accreting black holes. This component contaminates the targeted thermal component, and it must be carefully modeled in order to obtain reliable estimates of black hole spin. The new model SIMPL conserves photons and scatters a portion of the thermal KERRBB2 disk flux into a high-energy power law. By applying this model to the spectra of two black holes (H1743 and J1550), we established the validity of the model up to the limit where 25% of the thermal seed photons are up-scattered into the power-law component ($f_{\rm SC} \approx 25\%$).

This development resulted in a key discovery, namely that the inner disk radius in the SPL state is stable (up to $f_{\rm SC} \approx 25\%$), just as it is in the TD state. Furthermore, the radius one obtains as a source transitions between these two states is the same within several percent. In contrast, previous studies of the SPL state, which used non-self-consistent models, gave spuriously small values of the inner disk radius. In some cases, the apparent radius was even smaller than the radius of the event horizon!

The development of SIMPL has proved to be an important methodological advance that has enabled us to apply the CF method to a much wider body of data for a given source. Furthermore, this model is directly responsible for our success in measuring the spins of two moderately-to-strongly Comptonized sources: Cyg X–1, which has a nearly maximal spin ($a_* > 0.95$; Gou et al. 2011), and LMC X–1 ($a_* \approx 0.92$; Gou et al. 2009).

8.2 Summary: Foundations

Inferring black hole spin from an analysis of either the thermal continuum or reflection features rests on a fundamental assumption: that the inner edge of the black hole's accretion disk terminates at the ISCO radius for particles orbiting the black hole. The radius of the ISCO is uniquely determined by the black hole's mass and spin, scaling directly with mass, and inversely with spin.

In Chapter 4, we tested this crucial assumption. One prediction is that the inner-disk radius should remain constant over human time scales. To test this, we conducted a large study of the persistent black hole source LMC X–3. We used all available data gleaned from eight X-ray missions with coverage spanning 26 years. We found that the inner radius was constant to within 4% over 26 years of observation and over large variations in luminosity.

These results provide compelling observational evidence that the inner-disk radius is a constant and measurable property of a black hole. However, this constant radius $R_{\rm in}$ may be offset somewhat from $R_{\rm ISCO}$ as a result of magnetohydrodynamic forces acting in the accretion flow. Such effects are being assessed in ongoing GRMHD studies. Current state of the art simulations (e.g., Shafee et al. 2008; Reynolds & Fabian 2008; Kulkarni et al. 2011; Noble et al. 2011) predict that $R_{\rm in}$ is only modestly smaller than $R_{\rm ISCO}$, and that the correction to the spin parameter is only about 10% for low values of spin and less at high values.

Our results on the constancy of the inner disk radius demonstrate the feasibility of measuring black hole spin via both CF and Fe $K\alpha$ methods, as well as by any

other method that relies on the established relationship between spin and the inner radius of the disk.

The second important assumption of the CF method is that the binary orbital inclination (which is readily measured) is the same as the inclination of the black hole's spin axis. This assumption is expected to hold for most systems because accretion torques acting over millions of years are strong enough to align the black hole spin axis with the angular momentum vector (Martin et al. 2008).

In Chapter 5, we tested this assumption for the black hole binary J1550, the only system that displays pc-scale X-ray jets and whose inclination angle has been measured. We determined the inclination of the spin axis by modeling proper motion data for the two-sided jet using a model originally developed to describe gamma-ray bursts and using also a general-purpose Markov chain Monte Carlo code, which we developed for this application. We concluded that the black hole spin axis and the orbital angular momentum are likely aligned: the difference in their inclination angles was constrained to be $< 12^\circ$ at 90% confidence. This is the first test of its kind, and lends strong support to the alignment hypothesis.

8.3 Summary: New Spin Measurements

In Chapter 6, we applied the kinematic jet model used for J1550 to H1743, a system that also produced large-scale, two-sided X-ray and radio jets. Doing so allowed us to precisely measure the inclination angle of the black hole's spin axis, $i = 75^\circ \pm 3^\circ$, and the distance to the system, $D = 8.5 \pm 0.8$ kpc. Using these values of i and D

and an empirical distribution of black hole masses, we were able to estimate the spin of H1743 using the CF method: $a_* = 0.2 \pm 0.3$. This is the first application of the CF method that does not rely on a dynamical study of the optical counterpart to constrain one or more of the parameters M, i and D. All that is known about the optical counterpart are its magnitude and coordinates – even the orbital period of the system is unknown!

J1550 is a remarkable stellar-mass black hole: It is the first black hole microquasar to show X-ray jets and is one of only four black holes that exhibit a pair of commensurate (3:2) X-ray oscillations at high frequency (276 and 184 Hz). As part of a campaign to measure the masses and spins of black holes in binary systems, in Chapter 7, we determined the spin of J1550. For the first time, this was accomplished by using both leading techniques independently: the CF and Fe $K\alpha$ methods. Great care went into assessing all known sources of measurement uncertainty, including modeling errors and uncertainty in overall X-ray flux calibration. We found that the two measurements of spin were in good agreement and that the spin of J1550 is moderate. From CF alone, our 90% confidence limit for the spin was $0.34^{+0.20}_{-0.28}$, whereas using the Fe $K\alpha$ method alone, it was $0.55^{+0.15}_{-0.22}$. Combining both measurements, we concluded that the spin parameter of this black hole is $a_* = 0.49^{+0.13}_{-0.20}$ at 90% confidence.

For J1550, we speculated that the jets were powered by the rotational energy of the disk during a remarkable X-ray flare event. However, more recent work, which shows a strong correlation between jet power and spin (Narayan & McClintock 2012), indicates that the jets were most likely powered directly by the spin of the black hole. We note that our determination of the spin of J1550 was critically

important in establishing this relationship between jet power and spin.

8.4 New Horizons for Black Hole Spin

During the past several years, theorists have suggested several observational tests of the no-hair theorem (e.g., Johannsen & Psaltis 2010; Bambi & Barausse 2011; Vigeland & Hughes 2010). The no-hair theorem famously describes a black hole to be as simple as an elementary particle – fully described by M, a_* (and charge Q, which is believed to be unimportant for astrophysical black holes). Any departure from this predicted simplicity would have revolutionary consequences for our understanding of gravitationally-collapsed objects and the theory of general relativity.

By making straightforward measurements of black hole mass and by obtaining accurate measurements of spin via independent methods, it may be possible to detect deviations in the quadrupole moment of a black hole with respect to the value predicted by the Kerr metric. Such a deviation would be a violation of the no-hair theorem and represent a clear departure from general relativity (see e.g., McClintock et al. 2011, and references therein).

Currently, primarily the two methods described in this dissertation, the CF and Fe $K\alpha$ methods, are being used to measure the spins of a number of black holes. However, within X-ray astrophysics there are two other approaches that appear very promising: high-frequency QPOs, which are theorized to originate in strong gravity and to depend solely on the spin and mass of the black hole (e.g., Remillard & McClintock 2006), and X-ray polarimetry. Energy-dependent measurements of

X-ray polarization are quite sensitive to a black hole's spin, as shown by current models (Dovčiak et al. 2008; Li et al. 2009; Schnittman & Krolik 2009), and data suitable for the measurement of spin will soon be available following the launch of the *GEMS* satellite.

This thesis lays the groundwork for ongoing efforts to measure the spins of black holes. We have presented a new empirical model of Comptonization that allows the CF method to be successfully applied to far more X-ray spectral data and more sources than previously thought possible. Using this methodological advance, we tested the fundamental assumption of the CF method, namely the constancy of the inner-disk radius, by analyzing all available data for LMC X–3. We found that to within 4%, the inner-disk radius was constant over 26 years and was unaffected by source variability. This result establishes a firm foundation for the measurement of spin via either the CF or Fe $K\alpha$ methods. We also tested a second crucial assumption of the CF method, that the black hole's spin axis is aligned with the orbital angular momentum. An affirmative result from this test was obtained from modeling the ballistic motion of the X-ray and radio jets of J1550. This same kinematic jet model was then applied to the microquasar H1743 to determine its distance and the inclination of its black hole spin axis. This ultimately led to a measurement of the spin of its black hole. Returning to J1550, for the first time in a single work, we determined high-quality – and consistent – estimates of spin using both the CF and Fe $K\alpha$ methods.

The fledgling enterprise of measuring black hole spin has made great strides during the past six years. In the coming decade, next-generation instruments will be used to enable new methods of measuring black hole spin and to shed new light on

the demography of spinning black holes. Looking forward, these advances will be crucial in efforts to test general relativity and in coming to a deeper understanding of the most exotic objects nature has produced.

References

Abramowicz, M. A., Jaroszyński, M., Kato, S., Lasota, J.-P., Różańska, A., & Sądowski, A. 2010, A&A, 521, A15

Akaike, H. 1974, Automatic Control, IEEE Transactions on, 19, 716

Arnaud, K. A. 1996, in Astronomical Society of the Pacific Conference Series, Vol. 101, Astronomical Data Analysis Software and Systems V, ed. G. H. Jacoby & J. Barnes, 17

Arvanitaki, A., Dimopoulos, S., Dubovsky, S., Kaloper, N., & March-Russell, J. 2010, Phys. Rev. D, 81, 123530

Bambi, C., & Barausse, E. 2011, ApJ, 731, 121

Bardeen, J. M., & Petterson, J. A. 1975, ApJ, 195, L65

Bardeen, J. M., Press, W. H., & Teukolsky, S. A. 1972, ApJ, 178, 347

Beloborodov, A. M. 1999, ApJ, 510, L123

Berti, E., & Volonteri, M. 2008, ApJ, 684, 822

Blandford, R. D., & McKee, C. F. 1976, Physics of Fluids, 19, 1130

Blandford, R. D., & Payne, D. G. 1982, MNRAS, 199, 883

Blandford, R. D., & Znajek, R. L. 1977, MNRAS, 179, 433

Blum, J. L., Miller, J. M., Fabian, A. C., Miller, M. C., Homan, J., van der Klis, M., Cackett, E. M., & Reis, R. C. 2009, ApJ, 706, 60

Boella, G., Butler, R. C., Perola, G. C., Piro, L., Scarsi, L., & Bleeker, J. A. M. 1997, A&AS, 122, 299

Borozdin, K., Revnivtsev, M., Trudolyubov, S., Shrader, C., & Titarchuk, L. 1999, ApJ, 517, 367

Brenneman, L. W., & Reynolds, C. S. 2006, ApJ, 652, 1028

Brown, G. E., Lee, C., & Moreno Méndez, E. 2007, ApJ, 671, L41

Burnham, K. P., & Anderson, D. R. 2002, Model Selection and Multimodel Inference (New York, Springer-Verlag New York, Inc.)

Campanelli, M., Lousto, C. O., & Zlochower, Y. 2006, Phys. Rev. D, 74, 041501

Capalbi, M., Perri, M., Saija, B., Tamburelli, F., & Angelini, L. 2005, The Swift XRT Data Reduction Guide, Tech. Rep. 1.2

Chaty, S., Charles, P. A., Martí, J., Mirabel, I. F., Rodríguez, L. F., & Shahbaz, T. 2003, MNRAS, 343, 169

Cleveland, W. S. 1979, JASA, 74, 829

Coppi, P. S. 1999, in Astronomical Society of the Pacific Conference Series, Vol. 161, High Energy Processes in Accreting Black Holes, ed. J. Poutanen & R. Svensson, 375

Corbel, S., Fender, R. P., Tzioumis, A. K., Tomsick, J. A., Orosz, J. A., Miller, J. M., Wijnands, R., & Kaaret, P. 2002, Science, 298, 196

Corbel, S., Kaaret, P., Fender, R. P., Tzioumis, A. K., Tomsick, J. A., & Orosz, J. A. 2005, ApJ, 632, 504

Corbel, S., et al. 2001, ApJ, 554, 43

Cowley, A. P. 1992, ARA&A, 30, 287

Cowley, A. P., Crampton, D., Hutchings, J. B., Remillard, R., & Penfold, J. E. 1983, ApJ, 272, 118

Cowley, A. P., et al. 1991, ApJ, 381, 526

Davis, S. W., Blaes, O. M., Hubeny, I., & Turner, N. J. 2005, ApJ, 621, 372

Davis, S. W., Done, C., & Blaes, O. M. 2006, ApJ, 647, 525

Davis, S. W., & Hubeny, I. 2006, ApJS, 164, 530

Done, C., & Davis, S. W. 2008, ApJ, 683, 389

Done, C., Gierliński, M., & Kubota, A. 2007, A&AR, 15, 1

Done, C., & Kubota, A. 2006, MNRAS, 371, 1216

Done, C., Mulchaey, J. S., Mushotzky, R. F., & Arnaud, K. A. 1992, ApJ, 395, 275

Dovčiak, M., Muleri, F., Goosmann, R. W., Karas, V., & Matt, G. 2008, MNRAS, 391, 32

Dunn, R. J. H., Fender, R. P., Körding, E. G., Belloni, T., & Cabanac, C. 2010, MNRAS, 403, 61

Ebisawa, K. 1996, Release of New XRT Responses, and Comparison of ascaarf v2.53 and v2.62, Tech. rep.

Ebisawa, K. 1999, in ASP Conference Series, Vol. 161, High Energy Processes in Accreting Black Holes, ed. J. Poutanen & R. Svensson, 39–53

Ebisawa, K., Makino, F., Mitsuda, K., Belloni, T., Cowley, A. P., Schmidtke, P. C., & Treves, A. 1993, ApJ, 403, 684

Ebisawa, K., et al. 1994, PASJ, 46, 375

Esin, A. A., McClintock, J. E., & Narayan, R. 1997, ApJ, 489, 865

Fabian, A. C., Rees, M. J., Stella, L., & White, N. E. 1989, MNRAS, 238, 729

Fabian, A. C., et al. 2009, Nat, 459, 540

Farinelli, R., Titarchuk, L., Paizis, A., & Frontera, F. 2008, ApJ, 680, 602

Farr, W. M., Sravan, N., Cantrell, A., Kreidberg, L., Bailyn, C. D., Mandel, I., & Kalogera, V. 2011, ApJ, 741, 103

Fender, R. P., Gallo, E., & Russell, D. 2010, MNRAS, 406, 1425

Fiore, F., Guainazzi, M., & Grandi, P. 1999, Cookbook for BeppoSAX NFI Spectral Analysis, Bepposax SDC

Fragos, T., Tremmel, M., Rantsiou, E., & Belczynski, K. 2010, ApJ, 719, L79

Gallo, E., Fender, R. P., Miller-Jones, J. C. A., Merloni, A., Jonker, P. G., Heinz, S., Maccarone, T. J., & van der Klis, M. 2006, MNRAS, 370, 1351

García, J., & Kallman, T. R. 2010, ApJ, 718, 695

Garofalo, D., Evans, D. A., & Sambruna, R. M. 2010, MNRAS, 406, 975

Gelman, A., Roberts, G. O., & Gilks, W. R. 1996, Efficient Metropolis jumping rules, Vol. 5 (Oxford University Press), 599–607

Gelman, A., & Rubin, D. 1992, Statistical Science, 7, 457

Gierliński, M., & Done, C. 2003, MNRAS, 342, 1083

Gierliński, M., Zdziarski, A. A., Poutanen, J., Coppi, P. S., Ebisawa, K., & Johnson, W. N. 1999, MNRAS, 309, 496

Godet, O., et al. 2009, A&A, 494, 775

Gou, L., McClintock, J. E., Steiner, J. F., Narayan, R., Cantrell, A. G., Bailyn, C. D., & Orosz, J. A. 2010, ApJ, 718, L122

Gou, L., et al. 2011, submitted

Gou, L. J., et al. 2009, ApJ, 701, 1076

Greene, J., Bailyn, C. D., & Orosz, J. A. 2001, ApJ, 554, 1290

Guainazzi, M., Kirsch, M., & Haberl, F. 2009, Evaluation of the spectral calibration accuracy in EPIC-pn fast modes, Tech. Rep. CAL-TN-0083, XMM-Newton Science Operations Center

Hannikainen, D. C., et al. 2009, MNRAS, 397, 569

Hao, J. F., & Zhang, S. N. 2009, ApJ, 702, 1648

Hastings, W. K. 1970, Biometrika, 57, 97

Heinz, S. 2002, A&A, 388, L40

Hjellming, R. M., & Rupen, M. P. 1995, Nat, 375, 464

Hjellming, R. M., et al. 2000, ApJ, 544, 977

Homan, J., Miller, J. M., Wijnands, R., van der Klis, M., Belloni, T., Steeghs, D., & Lewin, W. H. G. 2005, ApJ, 623, 383

Homan, J., Wijnands, R., van der Klis, M., Belloni, T., van Paradijs, J., Klein-Wolt, M., Fender, R., & Méndez, M. 2001, ApJS, 132, 377

Huang, Y. F., Dai, Z. G., & Lu, T. 1999, MNRAS, 309, 513

Hurvich, C. M., & Tsai, C.-L. 1989, Biometrika, 76, 297

Jahoda, K., Markwardt, C. B., Radeva, Y., Rots, A. H., Stark, M. J., Swank, J. H., Strohmayer, T. E., & Zhang, W. 2006, ApJS, 163, 401

Johannsen, T., & Psaltis, D. 2010, ApJ, 716, 187

Kaaret, P., Corbel, S., Tomsick, J. A., Fender, R., Miller, J. M., Orosz, J. A., Tzioumis, A. K., & Wijnands, R. 2003, ApJ, 582, 945

Kalemci, E., Tomsick, J. A., Rothschild, R. E., Pottschmidt, K., Corbel, S., & Kaaret, P. 2006, ApJ, 639, 340

King, A. R., Lubow, S. H., Ogilvie, G. I., & Pringle, J. E. 2005, MNRAS, 363, 49

King, A. R., Pringle, J. E., & Livio, M. 2007, MNRAS, 376, 1740

Kubota, A., & Done, C. 2004, MNRAS, 353, 980

Kubota, A., Done, C., Davis, S. W., Dotani, T., Mizuno, T., & Ueda, Y. 2010, ApJ, 714, 860

Kubota, A., & Makishima, K. 2004, ApJ, 601, 428

Kubota, A., Makishima, K., & Ebisawa, K. 2001, ApJ, 560, L147

Kuiper, L., van Paradijs, J., & van der Klis, M. 1988, A&A, 203, 79

Kulkarni, A. K., et al. 2011, MNRAS, 414, 1183

Lamb, P., & Sanford, P. W. 1979, MNRAS, 188, 555

Laor, A. 1991, ApJ, 376, 90

Lee, C., Brown, G. E., & Wijers, R. A. M. J. 2002, ApJ, 575, 996

Leong, C., Kellogg, E., Gursky, H., Tananbaum, H., & Giacconi, R. 1971, ApJ, 170, L67

Li, L.-X., Narayan, R., & McClintock, J. E. 2009, ApJ, 691, 847

Li, L.-X., Zimmerman, E. R., Narayan, R., & McClintock, J. E. 2005, ApJS, 157, 335

Liu, J., McClintock, J. E., Narayan, R., Davis, S. W., & Orosz, J. A. 2008, ApJ, 679, L37

—. 2010, ApJ, 719, L109

Lodato, G., & Pringle, J. E. 2006, MNRAS, 368, 1196

Maccarone, T. J. 2002, MNRAS, 336, 1371

Maeda, Y. e. a. 2008, Recent Update of the XRT response. III. Effective Area, Tech. Rep. Suzaku Memo 2008-06, JX-ISAS

Magdziarz, P., & Zdziarski, A. A. 1995, MNRAS, 273, 837

Makishima, K., et al. 1996, PASJ, 48, 171

Martin, R. G., Tout, C. A., & Pringle, J. E. 2008, MNRAS, 387, 188

Martínez, V. J., Saar, E., Martínez-González, E., & Pons-Bordería, M.-J., eds. 2009, Lecture Notes in Physics, Berlin Springer Verlag, Vol. 665, Data Analysis in Cosmology (Springer Berlin / Heidelberg)

McClintock, J. E., Remillard, R. A., Rupen, M. P., Torres, M. A. P., Steeghs, D., Levine, A. M., & Orosz, J. A. 2009, ApJ, 698, 1398

McClintock, J. E., Shafee, R., Narayan, R., Remillard, R. A., Davis, S. W., & Li, L.-X. 2006, ApJ, 652, 518

McClintock, J. E., et al. 2011, Classical and Quantum Gravity, 28, 114009

McKinney, J. C. 2005, ApJ, 630, L5

McNamara, B. R., Kazemzadeh, F., Rafferty, D. A., Bîrzan, L., Nulsen, P. E. J., Kirkpatrick, C. C., & Wise, M. W. 2009, ApJ, 698, 594

Miller, J. M. 2007, ARA&A, 45, 441

Miller, J. M., Cackett, E. M., & Reis, R. C. 2009a, ApJ, 707, L77

Miller, J. M., Fabian, A. C., Nowak, M. A., & Lewin, W. H. G. 2005, in The Tenth Marcel Grossmann Meeting. On recent developments in theoretical and experimental general relativity, gravitation and relativistic field theories, ed. M. Novello, S. Perez Bergliaffa, & R. Ruffini, 1296

Miller, J. M., Raymond, J., Reynolds, C. S., Fabian, A. C., Kallman, T. R., & Homan, J. 2008a, ApJ, 680, 1359

Miller, J. M., Reynolds, C. S., Fabian, A. C., Miniutti, G., & Gallo, L. C. 2009b, ApJ, 697, 900

Miller, J. M., et al. 2001, ApJ, 563, 928

—. 2003, MNRAS, 338, 7

—. 2008b, ApJ, 679, L113

Miniutti, G., Panessa, F., de Rosa, A., Fabian, A. C., Malizia, A., Molina, M., Miller, J. M., & Vaughan, S. 2009, MNRAS, 398, 255

Miniutti, G., et al. 2007, PASJ, 59, 315

Mirabel, I. F., & Rodríguez, L. F. 1999, ARA&A, 37, 409

Mitsuda, K., et al. 1984, PASJ, 36, 741

Motta, S., Muñoz-Darias, T., & Belloni, T. 2010, MNRAS, 408, 1796

Narayan, R., & McClintock, J. E. 2005, ApJ, 623, 1017

—. 2012, MNRAS, 419, L69

Narayan, R., McClintock, J. E., & Shafee, R. 2008, in American Institute of Physics Conference Series, Vol. 968, Astrophysics of Compact Objects, ed. Y.-F. Yuan, X.-D. Li, & D. Lai, 265–272

Natarajan, P., & Pringle, J. E. 1998, ApJ, 506, L97

Neilsen, J., & Lee, J. C. 2009, Nat, 458, 481

Nishimura, J., Mitsuda, K., & Itoh, M. 1986, PASJ, 38, 819

Noble, S. C., Krolik, J. H., & Hawley, J. F. 2009, ApJ, 692, 411

—. 2010, ApJ, 711, 959

Noble, S. C., Krolik, J. H., Schnittman, J. D., & Hawley, J. F. 2011, ApJ, 743, 115

Novikov, I. D., & Thorne, K. S. 1973, in Black Holes (Les Astres Occlus), 343–450

Orosz, J. A. 2003, in IAU Symposium, Vol. 212, A Massive Star Odyssey: From Main Sequence to Supernova, ed. K. van der Hucht, A. Herrero, & C. Esteban, 365

Orosz, J. A., Steiner, J. F., McClintock, J. E., Torres, M. A. P., Remillard, R. A., Bailyn, C. D., & Miller, J. M. 2011, ApJ, 730, 75

Orosz, J. A., et al. 2001, ApJ, 555, 489

—. 2002, ApJ, 568, 845

—. 2009, ApJ, 697, 573

Özel, F., Psaltis, D., Narayan, R., & McClintock, J. E. 2010, ApJ, 725, 1918

Page, M. J., Soria, R., Wu, K., Mason, K. O., Cordova, F. A., & Priedhorsky, W. C. 2003, MNRAS, 345, 639

Parmar, A., & Smith, A. 1985, ME Calibration and Updates to the CCF, Tech. rep., EXOSAT Express

Penna, R. F., McKinney, J. C., Narayan, R., Tchekhovskoy, A., Shafee, R., & McClintock, J. E. 2010, MNRAS, 408, 752

Pessah, M. E., Chan, C.-k., & Psaltis, D. 2007, ApJ, 668, L51

Poutanen, J., & Svensson, R. 1996, ApJ, 470, 249

Reis, R. C., Fabian, A. C., Ross, R. R., & Miller, J. M. 2009, MNRAS, 395, 1257

Reis, R. C., Fabian, A. C., Ross, R. R., Miniutti, G., Miller, J. M., & Reynolds, C. 2008, MNRAS, 387, 1489

Reis, R. C., et al. 2011, MNRAS, 410, 2497

Remillard, R. A., & McClintock, J. E. 2006, ARA&A, 44, 49

Remillard, R. A., McClintock, J. E., Orosz, J. A., & Levine, A. M. 2006, ApJ, 637, 1002

Remillard, R. A., Muno, M. P., McClintock, J. E., & Orosz, J. A. 2002a, ApJ, 580, 1030

Remillard, R. A., Sobczak, G. J., Muno, M. P., & McClintock, J. E. 2002b, ApJ, 564, 962

Reynolds, C. S., & Fabian, A. C. 2008, ApJ, 675, 1048

Reynolds, C. S., & Nowak, M. A. 2003, Phys. Rep. , 377, 389

Ross, R. R., & Fabian, A. C. 1993, MNRAS, 261, 74

—. 2005, MNRAS, 358, 211

—. 2007, MNRAS, 381, 1697

Ross, R. R., Fabian, A. C., & Brandt, W. N. 1996, MNRAS, 278, 1082

Ryan, F. D. 1997, Phys. Rev. D, 56, 1845

Rybicki, G. B., & Lightman, A. P. 1979, Radiative processes in astrophysics (New York, Wiley-Interscience)

Sądowski, A., Abramowicz, M., Bursa, M., Kluźniak, W., Lasota, J., & Różańska, A. 2011, A&A, 527, A17

Schmoll, S., et al. 2009, ApJ, 703, 2171

Schnittman, J. D., & Krolik, J. H. 2009, ApJ, 701, 1175

Serlemitsos, P. J., et al. 2007, PASJ, 59, 9

Shafee, R., McClintock, J. E., Narayan, R., Davis, S. W., Li, L.-X., & Remillard, R. A. 2006, ApJ, 636, L113

Shafee, R., McKinney, J. C., Narayan, R., Tchekhovskoy, A., Gammie, C. F., & McClintock, J. E. 2008, ApJ, 687, L25

Shakura, N. I., & Sunyaev, R. A. 1973, A&A, 24, 337

Shapiro, S. L., Lightman, A. P., & Eardley, D. M. 1976, ApJ, 204, 187

Shapiro, S. L., & Teukolsky, S. A. 1983, Black holes, white dwarfs, and neutron stars: The physics of compact objects (New York, Wiley-Interscience)

Shrader, C., & Titarchuk, L. 1998, ApJ, 499, L31

Shrader, C. R., & Titarchuk, L. 1999, ApJ, 521, L121

Smith, D. M., Dawson, D. M., & Swank, J. H. 2007, ApJ, 669, 1138

Sobczak, G. J., McClintock, J. E., Remillard, R. A., Cui, W., Levine, A. M., Morgan, E. H., Orosz, J. A., & Bailyn, C. D. 2000a, ApJ, 544, 993

—. 2000b, ApJ, 531, 537

Soria, R., Wu, K., Page, M. J., & Sakelliou, I. 2001, A&A, 365, L273

Steiner, J. F., & McClintock, J. E. 2012, ApJ, 745, 136

Steiner, J. F., McClintock, J. E., & Reid, M. J. 2012, ApJ, 745, L7

Steiner, J. F., McClintock, J. E., Remillard, R. A., Gou, L., Yamada, S., & Narayan, R. 2010, ApJ, 718, L117

Steiner, J. F., McClintock, J. E., Remillard, R. A., Narayan, R., & Gou, L. J. 2009a, ApJ, 701, L83

Steiner, J. F., Narayan, R., McClintock, J. E., & Ebisawa, K. 2009b, PASP, 121, 1279

Steiner, J. F., et al. 2011, MNRAS, 1036

Stetson, P. B. 1987, PASP, 99, 191

Stuhlinger, M., et al. 2006, Status of XMM-Newton instruments cross-calibration with SASv6.5, Tech. Rep. CAL-TN-0052v3, XMM-Newton Science Operations Center

Sunyaev, R. A., & Titarchuk, L. G. 1980, A&A, 86, 121

Swank, J. H. 1999, Nuclear Physics B Proceedings Supplements, 69, 12

Tanaka, Y., & Lewin, W. H. G. 1995, in X-ray binaries, p. 126 - 174, ed. W. H. G. Lewin, J. van Paradijs, & E. P. J. van den Heuvel, 126–174

Tchekhovskoy, A., Narayan, R., & McKinney, J. C. 2010, ApJ, 711, 50

Titarchuk, L. 1994, ApJ, 434, 570

Titarchuk, L., & Lyubarskij, Y. 1995, ApJ, 450, 876

Titarchuk, L., Mastichiadis, A., & Kylafis, N. D. 1997, ApJ, 487, 834

Tomsick, J. A., Corbel, S., Fender, R., Miller, J. M., Orosz, J. A., Tzioumis, T., Wijnands, R., & Kaaret, P. 2003, ApJ, 582, 933

Tomsick, J. A., Corbel, S., & Kaaret, P. 2001, ApJ, 563, 229

Toor, A., & Seward, F. D. 1974, AJ, 79, 995

Treves, A., Belloni, T., Chiappetti, L., Maraschi, L., Stella, L., Tanzi, E. G., & van der Klis, M. 1988, ApJ, 325, 119

Turner, M. J. L., et al. 1989, PASJ, 41, 345

Valinia, A., & Marshall, F. E. 1998, ApJ, 505, 134

Verde, L., et al. 2003, ApJS, 148, 195

Vigeland, S. J., & Hughes, S. A. 2010, Phys. Rev. D, 81, 024030

Volonteri, M., Madau, P., Quataert, E., & Rees, M. J. 2005, ApJ, 620, 69

Wang, X. Y., Dai, Z. G., & Lu, T. 2003, ApJ, 592, 347

Weisskopf, M. C., Guainazzi, M., Jahoda, K., Shaposhnikov, N., O'Dell, S. L., Zavlin, V. E., Wilson-Hodge, C., & Elsner, R. F. 2010, ApJ, 713, 912

White, N. E., & Holt, S. S. 1982, ApJ, 257, 318

White, N. E., Nagase, F., & Parmar, A. N. 1995, in X-ray binaries, p. 1 - 57, 1–57

Will, C. M. 2008, ApJ, 674, L25

Wilms, J., Allen, A., & McCray, R. 2000, ApJ, 542, 914

Wilms, J., Nowak, M. A., Pottschmidt, K., Heindl, W. A., Dove, J. B., & Begelman, M. C. 2001, MNRAS, 320, 327

Woosley, S. E. 1993, ApJ, 405, 273

Xue, Y., Wu, X., & Cui, W. 2008, MNRAS, 384, 440

Yao, Y., Wang, Q. D., & Zhang, S. N. 2005, MNRAS, 362, 229

Zdziarski, A. A., Leighly, K. M., Matsuoka, M., Cappi, M., & Mihara, T. 2002, ApJ, 573, 505

Zhang, S. N., Cui, W., & Chen, W. 1997, ApJ, 482, L155

Zoghbi, A., Fabian, A. C., Uttley, P., Miniutti, G., Gallo, L. C., Reynolds, C. S., Miller, J. M., & Ponti, G. 2010, MNRAS, 401, 2419

Życki, P. T., Done, C., & Smith, D. A. 1999, MNRAS, 309, 561